Bifurcations in a swirling flow

Elena Vyazmina

HAL Id: tel-00538944
https://pastel.hal.science/tel-00538944

Submitted on 25 Nov 2010

École Polytechnique

Laboratoire d'Hydrodynamique (LadHyX)

Thèse présentée pour obtenir le grade de

DOCTEUR DE L'ÉCOLE POLYTECHNIQUE

spécialité: mécanique

par

ELENA VYAZMINA

Bifurcations in a swirling flow*

* Bifurcations d'un écoulement tournant

soutenue le 13 juillet 2010 devant le jury composé de:

J.-M. Chomaz	directeur de thèse	École Polytechnique, France
J.-C. Robinet	rapporteur	ENSAM, France
M. Rossi	examinateur	Université de Paris VI, France
P.J. Schmid	directeur de thèse	École Polytechnique, France
D. Sipp	rapporteur	ONERA DAFE, France

Contents

List of Figures

1 Introduction

1.1 Swirling flows: introduction

A flow of liquid or gas is said to be 'swirling' when its mean direction is aligned with its rotation axis, implying helical particle trajectories. This flow configuration corresponds generally to jet-like flows subject to solid body rotation.

The study of swirling flows is motivated by a large number of phenomena in nature and engineering. Such flows are encountered in many geophysical settings, such as tornadoes, dust devils, or waterspouts, see figure 1.1. In chemical and mechanical engineering the rotation of a fluid mixture is used to enhance mixing or separation of the various species by the action of centrifugal forces. It is also of great interest for many phenomena in external or internal aerodynamical applications. Relevant examples include the lift and drag properties of aircrafts or the mixing inside combustion chambers. In reactive flows, swirl is frequently used to achieve a larger spreading angle of the jet which in turn stabilizes the flame.

In spite of the fact that solid-body rotating flows have been investigated for more than a hundred years, there is still a large variety of phenomena which have not been completely understood yet. This can be justified by the highly nonlinear nature of the mechanisms at play, their three-dimensionality, the strong dependence on initial conditions, as well as the non-trivial modeling of the boundary conditions.

On one hand, the mathematical difficulties associated with the model equations (incompressible Navier-Stokes equations in their simplest form) make it unlikely that fully analytical methods for solving partial differential equations will be of great help in the near future. On the other hand, the laboratory experiments reproducing these phenomena are generally too complex, do not yield full information about the flow fields, and are sometimes also very expensive. Given this situation the principal hope for progress for the investigation of swirling flows lies in the use of direct numerical simulations, which combine the advantages of both mathematical and physical approaches. All related methods will be discussed in detail in the next sections of this dissertation.

Figure 1.1: (a) Tornado roping out near Springer, Oklahoma, May 6 2001; (b) dust devil; (c) Photograph of waterspouts taken in August 1999 near the coast of Albania from the ferry boat "Greece-Italy" by Roberto Giudici.

1.2 Vortex breakdown and its applications

1.2.1 Definition and classification

Typical features of swirling jet flows are the curvature effects due to the azimuthal circulation. This results in a radial pressure gradient which influences the development of the shear layers typical of jet-like flows. As a non-trivial result, complex recirculation zones appear, leading to complex phenomena such as vortex breakdown. Sometimes two or more states can co-exist for the same values of the control parameters (bistability), leading to hysteresis and sudden transitions between various flow states. As we shall see, such complex dynamics are of both fundamental and practical interest.

Vortex breakdown arises in swirling flows with non-zero azimuthal and axial components of velocities. It was discovered at the end of the 1950's and is still a broadly discussed topic in the fluid community today. Roughly speaking, such a phenomenon occurs when rotation effects becomes comparable or larger than advection effects within the jet. As we shall see, the concept of 'vortex breakdown' is not universal and several different types can be identified. Usually 'vortex breakdown' is defined as a dramatic change in the structure of the flow core[7, 91], with the noticeable appearance of stagnation points followed by regions of reversed flow referred to as the vortex breakdown bubble, as shown in figure 1.2. Leibovich[58] defined vortex breakdown as "a disturbance characterized by the formation of an internal stagnation point on the vortex axis, followed by a reversed flow in a region

of limited axial extend".
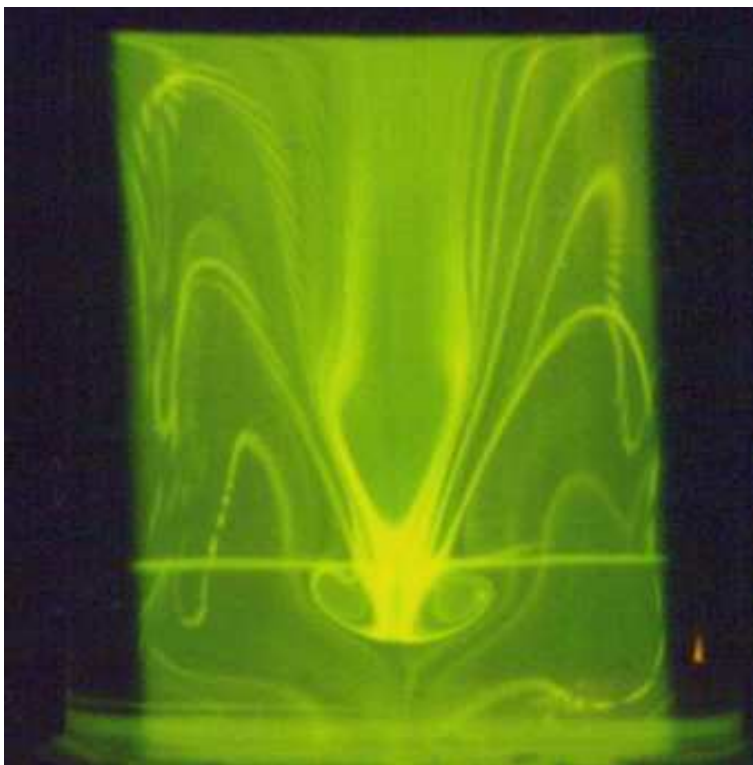
Figure 1.2: Unsteady vortex breakdown in a closed cylindrical container by S. Harris.

Vortex breakdown phenomenon can be observed either in axisymmetric form, so-called breakdown bubble, in the non-axisymmetric spiral, or in "double-helix-type" form[91]. Bubble-type breakdown (as already mentioned above) is characterized by a nearly axisymmetric region of reversed flow with a stagnation point located on the axis.

The other predominant vortex breakdown form is of spiral type. Experimentally, by introducing dye along the vortex axis, this type of breakdown manifests itself by a non-axisymmetric kink on the dye filament, followed by a corkscrew-shaped twisting of the dye.[58] The spiral structure rotates in the same direction as the surrounding fluid.

The less commonly observed double-helix type occurs only for low (jet-based) Reynolds numbers and high swirl. The original filament along the vortex axis is decelerated and expands into a sightly curved triangle sheet. Each half of the sheet is wrapped around the other to form the double helix.[92]

1.2.2 Vortex breakdown in tornadoes

Vortex breakdown has been documented in tornadoes.[75, 67] Tornadoes occur in a large variety of shapes and sizes, and the flow within them can range considerably in complexity.

Walko [110] discussed the vortex line configuration of a tropical tornado, when vortex lines trace paths which are oriented axially through the vortex core and spread radially outward in all directions up to a distance of several core diameters before reaching the surface friction layer. The convergence of vortex lines causes an increase of both the swirl and the axial velocity.
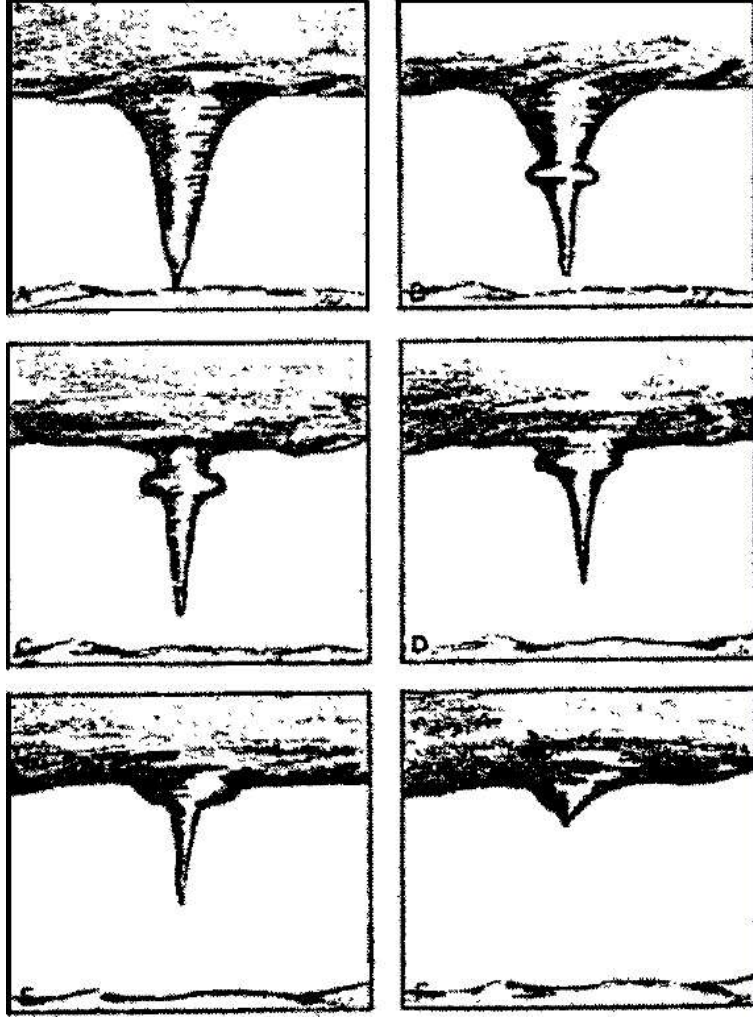
Figure 1.3: Stretching of a vortex breakdown-like phenomena, appeared in South Platte Valley tornadoes of June 7, 1953, adapted from Reber[77].

The occurence of vortex breakdown in tornadic mesocyclones has been inferred from observations of a downdraft near the central axis of the mesocyclonic vortex.[15, 109] In practice the occurrence of vortex breakdown in tornadoes decreases the swirl velocity and thus makes the tornado less destructive[23], see figure 1.3. The appearance of vortex breakdown in tornadoes makes it unstable, thus leading to the decrease of the destructive effect of this disaster. In such a way an understanding and control of vortex breakdown can be used by environmental engineers to artificially destroy tornadoes. This motivates the understanding of the underlying flow dynamics.

1.2.3 Vortex breakdown at the tip of delta wings

Vortex breakdown is also of great interest in aeronautical applications. The characteristic flow pattern in the wake of Delta wings is the formation of a pair of leading-edge vortices at the tip of the wings for a given angle of attack. The vortices are created by the roll-up of the shear layers separating at the leading edge and carried downstream by the free-stream velocity. The swirling flow reattaches to the upper surface and can separate again to form secondary, even tertiary vortices. Between the two primary vortices, the flow attaches to the wing. The two vortices are characterized by very high speeds, inducing a low pressure zone behind them. This causes an additional lift force called "vortex lift" which increases as long as the angle of attack is not too large.
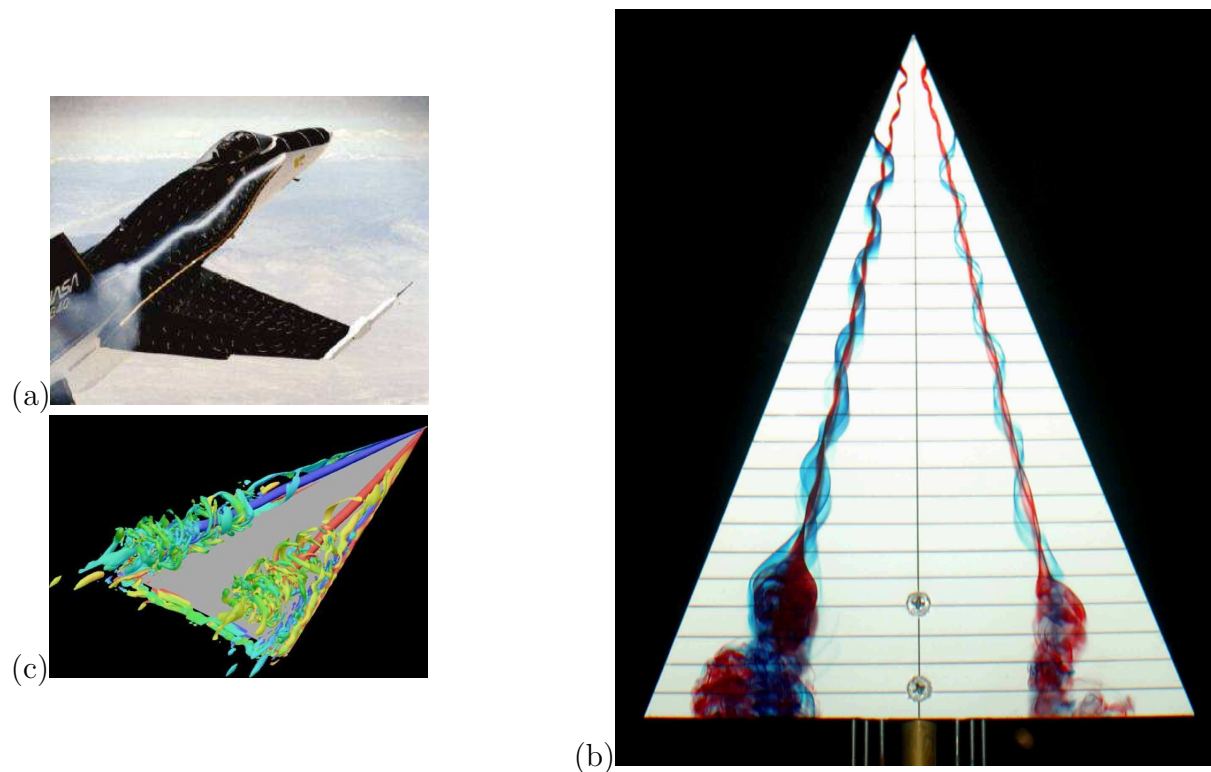
Figure 1.4: Vortex breakdown on a delta wing with high angle of attack: (a) F-18 HARV, NASA Dryden Flight Research Center; (b) flow gallery of fluid mechanics group of Department of Mechanical Engineering, National University of Singapore; (c) ONERA.

As the angle of attack increases, these leading edge vortices experience a sudden disorganization, known as vortex breakdown, see figure 1.4 (a). It can be described by a rapid deceleration of both the axial and swirl components of the mean velocity, together with a dramatic expansion of the vortex cores. The flow undergoing breakdown appears very turbulent. As the position of breakdown moves upstream with an increasing angle of attack,

this ultimately leads to the loss of lift and stall of the Delta wing. Experiment -(a) and (b)- and numerical simulations -frame (c)- shown in figure 1.4 illustrate the propagation and amplification downstream of the helicoidal structure, leading to the subsequent turbulence.

The first experiments on Delta wings were performed in the 1950's [65, 76] in order to enhance aircraft performance (particularly in the context of fighter aircrafts). It was demonstrated that vortex breakdown not only causes a loss of lift, as described above, but can also cause high roll movement in case breakdown occurs over one wing only.[73]

All the phenomena described (drop in lift, drop in drag, rolling instabilities) altogether lead to a loss of aircraft control.[26] This again is a strong motivation for understanding and predicting the occurrence of vortex breakdown. The use of numerical simulations can allow a careful optimization of future aircraft wings, which not only possess larger lift but also safer stability characteristics for a wide range of angles of attack.

1.2.4   Combustion and cyclone chambers

Combustion dynamics is under increasing consideration in order to develop more compact, more efficient and less polluting burners. This task requires a detailed understanding of the dynamics of the swirling flow as well as the effects of the interaction with the flame structure.

Most fuel injectors contain devices triggering swirl in the flow, and there are many studies about the influence of swirl on the combustor behavior. The swirl is frequently used to stabilize the flame near the burner exit, using the recirculation bubble of vortex breakdown as a flame holder.[38, 6] The recirculation zone is detached from any boundary, which is extremely advantageous as the flame will not have any negative effect on the walls. In the premixed case, burned particles are trapped in this breakdown zone where they induce a region of higher temperature. Heat transfer from this hot region to the surrounding swirling flow helps to stabilize the flame as well as to burn more of the reactants, thereby improving combustion effectiveness[98] and reducing unwanted pollutants. In the nonpremixed case where liquid fuel is injected into a swirling flow of air, the hot breakdown zone serves as a noninvasive flame holder where fuel particles are trapped for longer residence times. As a consequence, the quality of the mixing of air and fuel is improved as mentioned in Ref.[85].

Cyclone chambers used in many engineering devices, such as vacuum cleaner, and various particle separators. The swirling flow exerts a centrifugal force on the particles so that they eventually hit the cyclone wall, lose momentum and fall down. Clean gas can thus leave the cyclone separator through a central orifice.

The spiral mode of vortex breakdown has also been observed in the exhaust regions of cyclone chambers, and can result in a vortex "whistle".[38] For higher swirl, the vortex precesses downstream and can extend into the cyclone. Vortex core precession (i.e. the spiral mode of vortex breakdown) has been observed in long cyclonic dust separators. This

precession motion is known to prevent the dust removal process.

For other technological applications depending on the structure of the vortex break-down, see the reviews Refs. [91, 92]. Understanding the mechanisms governing the vortex behavior (origin, development and breakdown with further evolution) in technological devices allows for a determination of the optimal operating regimes.

1.3 Previous investigations and state of the art

It was emphasized in Ref.[46] that "despite more than four decades of extensive studies, there is no consensus on what constitutes vortex breakdown, let alone its mechanism". In this section we will review the main works in connection with the present study.

1.3.1 Experimental investigations

Early experimental investigations of vortex breakdown were carried out in flows above Delta wings at high angles of attack, where a significant flow-field variation in the axial direction as well as axisymmetric disturbances were observed. A major drawback of Delta wing experiments is that the axial and azimuthal velocity cannot be varied independently.

Most of the subsequent fundamental experimental studies were hence carried out in better, more controlled set-ups. For instance, the use of an open cylindrical pipe container allows one to get rid of unpredictable ambient disturbances, *i.e.* by imposing well-defined boundary conditions.[44, 91, 30, 106]

Most of the observations in pipes concern the different flow states of vortex breakdown. The flow is then characterized by two parameters, namely the Reynolds number Re (based on the diameter of the pipe and the mean axial velocity) and the swirl parameter S (the ratio between the azimuthal velocity in the vortex core and the axial velocity, i.e. $S = \dfrac{u_\theta}{u_x}$). Varying Re and S in a slightly diverging pipe, Sarpkaya[91, 92] identified three different modes of vortex breakdown, respectively the bubble, spiral and double-helix types, see for instance figure 1.5. Using a similar experimental set-up Faler and Leibovich[30] identified up to seven distinct modes including the usual bubble and spiral types as well as the double helix type. Other identified states can be considered as variants of these. Lately a new form of vortex breakdown was found by Billant et al.[13] in which the vortex takes the form of an open conical sheet, see figure 1.6.

Althaus et al.[3] used a constant diameter pipe to show that both bubble and axisymmetric type breakdown are typical of low Re, whereas only spiral type breakdown has been found to occur at high Re. However, Leibovich[58] pointed out that Re controls primarily the diameter of the vortex core rather than the flow dynamics. It thus seems reasonable to re-define a Reynolds number in terms of the vortex core diameter, which represents the
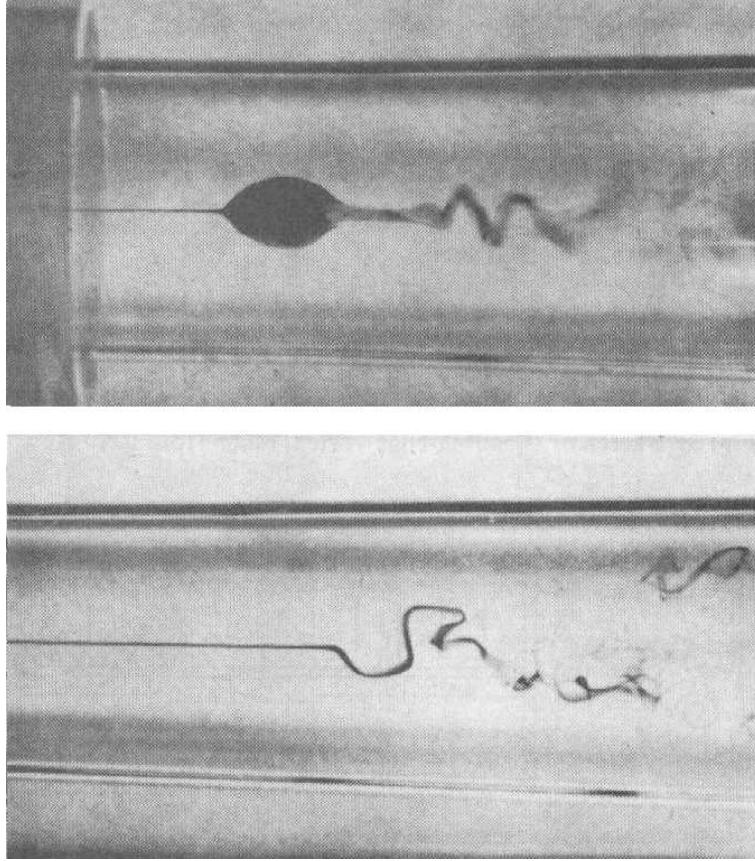
Figure 1.5: Bubble or axisymmetric form (on the top), and spiral form (on the bottom) of vortex breakdown in a tube, Re=4000 (based on the diameter of the tube).[29]

characteristic viscous length scale for a swirling flow.[59]

Importantly, experiments by Sarpkaya[91, 92] showed that in a certain range of parameters, both bubble and spiral breakdown types may randomly appear in time, even if the external flow conditions are held constant. Escudier & Zehnder[28] reported random and unpredictable transitions between different kinds of breakdown.

Recently, Liang and Maxworthy[63] identified a super-critical Hopf bifurcation for a Reynolds number of $Re = 1000$ (based on the diameter of the nozzle section of the apparatus, corresponding to the vortex core). This self-sustained oscillation was observed in the inner shear layer between the central reverse flow and the conical jet, thus having the appearance of spiral-type vortex breakdown.

Sarpkaya[93] reported that an imposed adverse axial pressure gradient can cause an upstream shift in the location of vortex breakdown, and in some cases even initiate the breakdown. The confinement imposed by the tube constriction is found to be critical for the occurrence of breakdown: Sarpkaya[93], Escudier & Zehnder[28] and Althaus, Brüker & Weimer[2] found that the pressure gradient induced by the diverging tube makes break-
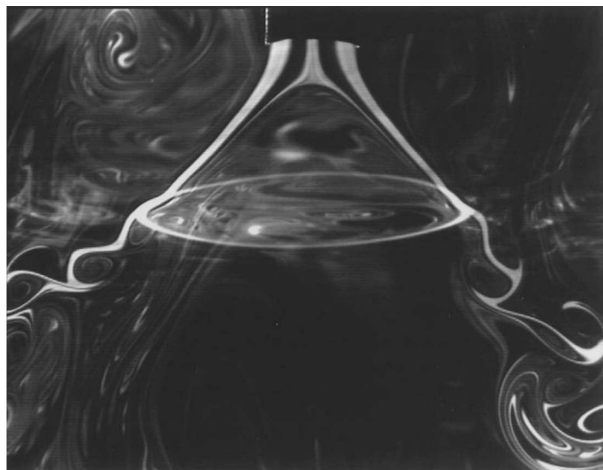
Figure 1.6: Cone form of vortex breakdown, Re = 606.[13]

down occur at lower Reynolds number than in a straight pipe. This physical feature allows for the identification of another important control parameter, namely the externally imposed pressure gradient.

In free swirling jets, experimental investigations of vortex breakdown have been conducted at high Reynolds numbers and have mainly focused on velocity distributions and associated turbulence fluctuations.[31, 74]

1.3.2 Theoretical and numerical studies

The phenomenon of vortex breakdown is extremely complex and it is hence difficult to obtain enough experimental data details to fully understand and comprehend the mechanisms it involves. Given this situation theoretical and numerical techniques are a reasonable and attractive way to obtain additional information on the structure of the breakdown, as well as to identify the range of parameters affecting its occurrence and development.

Axisymmetric vortex breakdown

Squire[102] and Benjamin[7, 8, 9] independently developed analytical theories. They both considered an axisymmetric, inviscid, and steady vortex and suggested the existence of a 'critical state' separating a 'subcritical' from a 'supercritical' flow state. In the subcritical case, disturbances can propagate upstream and downstream, and standing waves are supported. In the supercritical one, only downstream propagation is possible. Squire considered breakdown as an accumulation of upstream travelling disturbances at the locus of the critical state (like in the case of a shock wave), whereas Benjamin thought of breakdown as an abrupt change, i.e. a transition with finite amplitude, between two conjugate flow states (like a hydraulic jump in an open-channel flow).

Escudier and Keller[27] and Keller et al.[52] extended Benjamin's conjugate-state transition ideas and introduced the concept of a two-stage transition, i.e. the breakdown is assumed to occur in two different stages, as illustrated in figure 1.7. The first stage is an
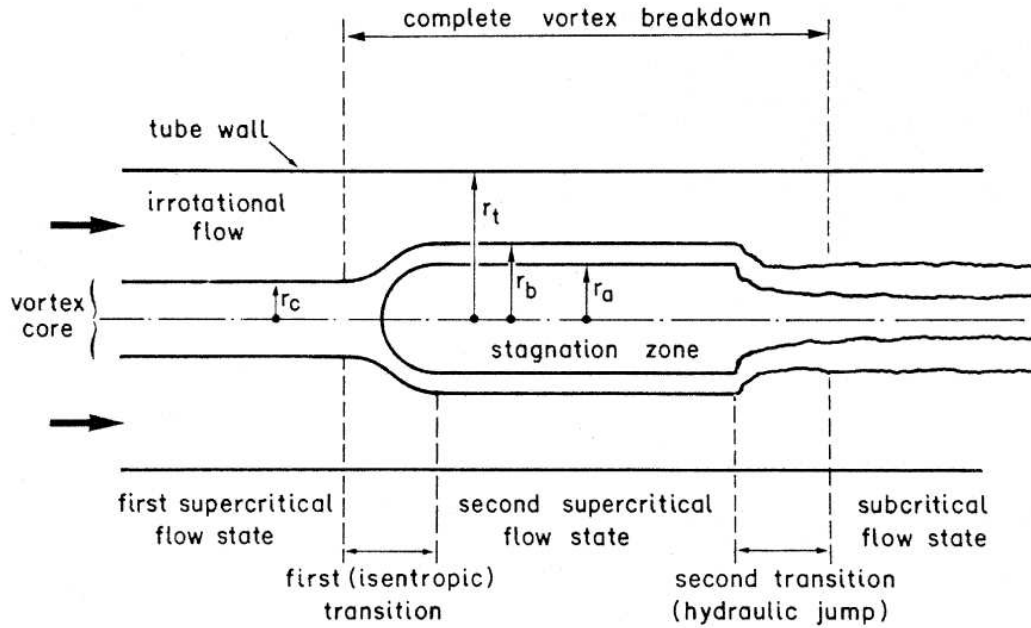
Figure 1.7: Schematic diagram of the transition theory Escudier and Keller,[27] taken from the review of Lucca-Negro.[66]

isentropic transition from the upstream supercritical flow to an intermediate supercritical flow. There is no change in the flow force (or momentum flux) even for a large-scale transition. The second stage is a jump-like transition to the final subcritical flow state. The intermediate supercritical state consists of a zone of nearly stagnant fluid surrounded by a region of potential flow. The two zones are separated by a layer of rotational fluid originating in the upstream vortex core, which is subject to an intense shear. The instability and subsequent roll-up of this shear layer at large Re were regarded by Escudier & Keller[27] as an explanation for the occurrence of the spiral form of breakdown, while the basic breakdown process is axisymmetric.

Later, Derzho & Grimshaw[25] conducted an asymptotic study of large-amplitude solitary waves occuring in an inviscid incompressible axisymmetric rotating flow inside an infinitely long circular tube. They were able to construct analytical solutions which describe recirculation zones with reversed flow, located on the axis of the tube. Derzho & Grimshaw[25] found that although the structure of the recirculation zone is universal, the presence of solitary waves is quite sensitive to the actual axial and rotational velocity configuration upstream. Their theoretical model is capable of predicting multiple-state solutions, the flow around the separation bubble, as well as its shape. However, this model can not be completely confirmed numerically due to the assumption of an infinitely long

circular tube and of vanishing viscosity.

Non uniqueness of the steady state solution

One important characteristic assumption of all numerical investigations performed before 1986 is that computed steady state solutions are unique. Táasan[104] and Hafez et al.[40] demonstrated the existence of a branch of nontrivial (non-columnar) states, i.e. standing solitary wave solutions intersecting the branch of trivial (columnar) solutions at a simple bifurcation point.
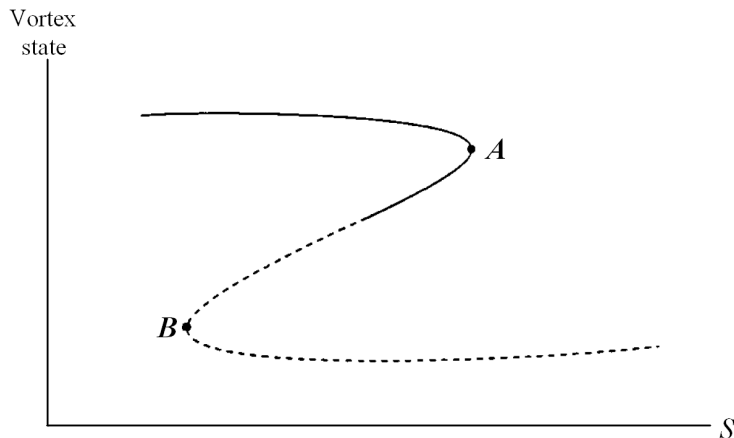
Figure 1.8: Representative solution diagram relating the various vortex states to the swirl parameter S. A corresponds to the primary limit point; B corresponds to the secondary limit point; the black line corresponds to the non-reversed flow, dashed line corresponds to the reversed flow. Adapted from Ref.[12]

Beran[10] also observed non-unique solutions of the steady Navier-Stokes equations for swirling flows inside pipes. The numerical work of Beran & Culick[12] showed clear evidence for the non-uniqueness of the solutions for large Re, which physically manifests itself by the abrupt formation of a reversed flow above a critical value of the swirl S. As a consequence, for sufficiently large Re vortex breakdown occurs abruptly as S is increased. In a diagram displaying the path of the solution as a function of S (see figure 1.8), the non-uniqueness arises through the formation of two limit points A and B along the solution path, between which the vortex has three possible states. Solution paths for $Re \geq O(1000)$ are characterized by an ensemble of three flow types: columnar, soliton and vortex breakdown state with reversed flow. For smaller values of Re, viscous forces are strong enough to damp out this limit point behavior, hence only one unique solution exists.

Lopez[64] considered the same pipe geometry as Beran & Culick[12], and also observed a hysteretic behavior. The unsteady branch co-exists with the previously found stable steady solution branch and originates from a turning point bifurcation. It was claimed that this
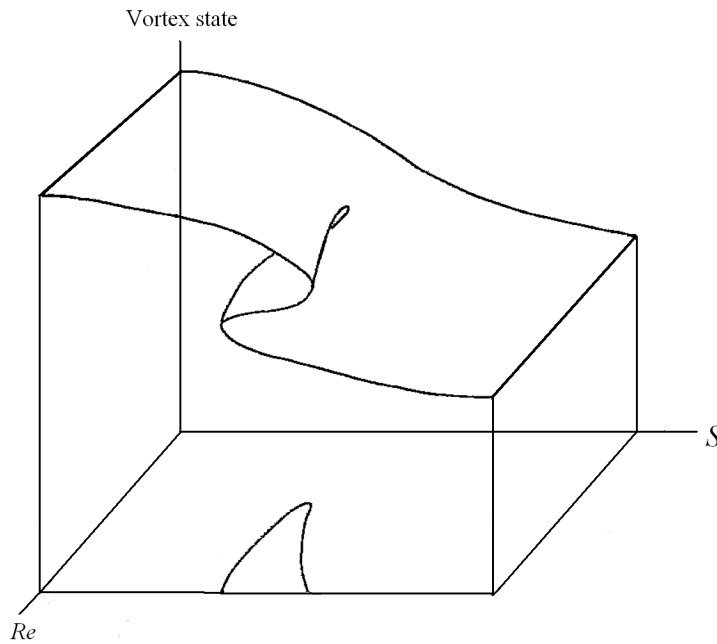
Figure 1.9: Schematic view of the steady solution surface in parameter space (Re, S). Adapted from Ref.[64]

type of bifurcation structure in the (Re, S)-parameter space suggests the possibility for hysteresis , see for instance figure 1.9. Such a complex dynamics was actually observed in the numerical study of Lopez[64] and Beran & Culick[12]. Similar to Lopez[64], Darmofal[22] showed that the columnar and vortex breakdown branches are stable to small axisymmetric disturbances, whereas the equilibrium state (in the fold) connecting the columnar and the vortex breakdown states is unstable.

Wang & Rusak[113] investigated the unsteady Euler equations describing a swirling flow in a finite-length constant-area pipe. They performed a stability analysis of the incompressible inviscid vortex breakdown under the hypothesis of axisymmetry. They found that the axisymmetric breakdown evolves from an initial columnar swirling flow to another relatively stable equilibrium state, representing a flow around a separation zone, as the result of the loss of stability of the columnar base flow when the swirl rate of the incoming flow exceeds a critical threshold. Wang & Rusak[113] also showed the existence of two characteristic swirl levels of the incoming pipe flow, S_0 and S_1 ($S_0 < S_1$), determined by solving a system of ordinary differential equations. Swirling columnar flows with a swirl level S less than the threshold level S_0 are stable to all axisymmetric disturbances. In the range $S_0 < S < S_1$ the flow may evolve into one of two distinct steady states, depending on the shape and amplitude of the initial disturbances. When the disturbances are sufficiently small they will decay in time and the flow will return to a columnar state. However, when

the initial disturbances are large enough, they will grow and evolve nonlinearly towards a state characterized by a large stagnation region within the swirling flow, called the vortex breakdown solution. When $S > S_1$, initial disturbances always grow and evolve again into a vortex breakdown solution. As the incoming swirl level is increased above S_0 and is near or above S_1, the columnar swirling flow loses its stability and a breakdown state develops. These authors point out that the mechanism is governed by the propagation of small- and large-amplitude disturbances in the pipe and their interaction with the inlet conditions. This study shows quite good agreement with the numerical computations of Beran & Culick[12] and Lopez[64] already discussed above.

In another subsequent study, Wang & Rusak[114] considered the effect of a small viscosity on a near-critical axisymmetric incompressible swirling flow in a straight pipe of finite axial extent. They demonstrated the singular behavior of a regular expansion of the solution in terms of the small viscosity parameter around the critical swirl S_1. This singularity suggests that large-amplitude disturbances may be induced by the small viscosity when the incoming flow has a swirl level around S_1. The small-disturbance analysis, developed by Wang & Rusak[114] shows that a small but finite viscosity breaks the transcritical bifurcation of solutions of the Euler equations at the critical swirl S_1 into two branches of viscous solutions. It was observed that these branches fold at two limit points $S_{c\nu 1}$ and $S_{c\nu 2}$ near S_1, with a finite gap between them. This means that no near-columnar equilibrium state can exist for an incoming flow with a swirl close to the critical level, and the flow must develop large disturbances in this swirl range. Beyond this range, two equilibrium states may co-exist. When Re is decreased this special behavior uniformly changes into a branch with a single equilibrium state for each incoming swirl. This special behavior of viscous solutions shows good agreement with the numerical simulations of the axisymmetric Navier-Stokes equations by Beran & Culick[12]. These results are summarized in figure 1.10.

In another study Rusak[81] also investigated the effect of small inlet azimuthal vorticity perturbations. He obtained the bifurcation of solutions at the critical swirl S_1 with a finite gap between the two branches. He noticed that positive inlet azimuthal vorticity perturbations may be used to delay vortex breakdown to higher swirl levels whereas negative perturbations induce the appearance of vortex breakdown at levels below the critical swirl.

Effect of an imposed pressure gradient

The effect of a variable cross-sectional area of a tube (inducing a pressure gradient), on a rotating flow was studied first by Batchelor[5] at the end of 1960's. He noticed that the solution families for inviscid swirling flows in a diverging pipe undergo a fold as the swirl is increased. At the same time Lambourne[53] examined analytically the effect of an imposed pressure gradient on an inviscid vortex. The results indicate the formation of a reversed flow and show the existence of a critical swirl threshold, beyond which dramatic changes of flow structure occur.
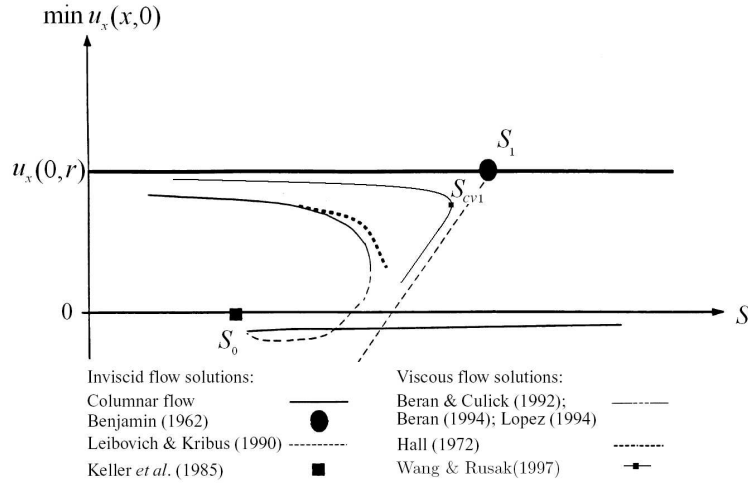
Figure 1.10: The bifurcation diagram of steady solutions of Euler or Navier- Stokes equations (summary of the previous results). Adapted from Ref. [114]

In the 1990's, Buntine & Saffman[17] examined the development of an inviscid steady swirling flow inside a finite-length diverging pipe. Their numerical computations result in a bifurcation diagram with a turning point for S at which the branch of solutions folds, and two equilibrium solutions exist in a certain range of swirl below this limit level. They also claimed that, in case a stagnation point appears along the pipe outlet, non-regular solutions exhibiting a separation zone must develop, and the flow inside the separation zone cannot be determined solely by the inlet conditions.

Rusak et al.[84] also investigated the effect of a small pipe divergence on an inviscid, incompressible, near-critical axisymmetric swirling flow in a finite pipe. Similarly to a previous study,[114] they demonstrated the singular behavior of a regular expansion solution, in terms of the pipe divergence parameter σ, around the critical swirl S_1. They found that the divergence σ breaks the transcritical bifurcation of solutions of the flow into two equilibrium solution branches. These branches fold at limit swirl levels $S_{c\sigma1}$ and $S_{c\sigma2}$ near the swirl S_1 resulting in a finite gap that separates the two branches. No columnar axisymmetric state can exist within this gap-range of incoming swirl. Beyond this range, two steady states may co-exist under the same boundary conditions. Rusak et al.[84] also found that when the pipe divergence is increased, there is a gradual change of solution with no fold. Rusak & Judd[83] found that an exchange of stability occurs at $S = S_{c\sigma1}$ for the non-columnar vortex family. The near-columnar states are stable, whereas the states with large disturbances are unstable. Also, the near-columnar states lose their stability as the swirl level approaches $S_{c\sigma1}$. Therefore, when the swirl level of the incoming flow is above $S_{c\sigma1}$, the flow in the pipe must develop transition, with large-amplitude perturbations leading to the vortex breakdown state.

Recently Leclaire & Sipp[55] investigated theoretically the effect of the inlet boundary conditions on the bifurcation diagram in a pipe of finite axial length. Steady solutions were obtained using weakly nonlinear analysis and numerical simulations. They computed respectively the accelerated and decelerated branches of solutions and investigated the influence of the pipe cross-section on the solutions.

Three-dimensional vortex breakdown

Gatski and Spall[34] performed numerical simulations of spiral-type vortex breakdown. They pointed out that this type of breakdown is characterized by an off-centered stagnation point which is rotating around the axis.

Later Ruith and al.[79] described the physical formation of the axisymmetric quasi-steady bubble breakdown state and suggested that this configuration becomes unstable to helical disturbances in the wake of the bubble, thus triggering helical breakdown modes. For higher swirl parameter the single helix is replaced by a pulsatile double-helix breakdown mode. They also investigated the effect of Re on the structure of the vortex breakdown. Increasing Re leads to one axisymmetric breakdown bubble, which is replaced by two bubbles for even larger Re. A further increase in Re renders the flow periodic in time. A similar sequence leading to multiple breakdown bubbles was obtained also for the swirl parameter S. It is worth mentioning that, unfortunately, the spatial resolution used for large Re was not sufficient, and that some of the results for higher Re are not robust with respect to the numerical resolution.

Gallaire et al.[33] interpreted the spiral form as a nonlinear global mode originating at the convective/absolute instability transition point for the axisymmetric breakdown state. They emphasized that the breakdown bubble is equivalent to the presence of a bluff body, the wake of which becomes absolutely unstable.

In another investigation Gallaire & Chomaz[32] tried to identify the mode selection mechanism responsible for the appearance of a double-helix structure in the pre-breakdown stage, for which the circulation vanishes away from the jet. Stability properties were directly retrieved from numerical simulations of the linear impulse response for different values of the swirl parameter.

Recently Herrada & Fernandez-Feria[45] studied the appearance and development of vortex breakdown in a straight pipe without wall friction. The numerical simulations showed that the basic form of breakdown is axisymmetric and a transition to helical breakdown modes is caused by an instability inside the original recirculation bubble. Varying the Reynolds number and the swirl parameter, two unstable modes were found with either a helical or double-helical structure. Numerical simulations showed that the frequency of the helical flows increases with the swirl parameter.

General vortex breakdown review

As already mentioned above, vortex breakdown has multiple applications leading to numerous theoretical, numerical and experimental investigations, see for example the reviews of Hall,[41, 42] Leibovich,[58, 60] Wedermeyer,[115] Escudier,[26] Stuart,[103] Delery,[24] Ash and Khorrami,[4] Althaus et al.,[2] Sarpkaya[95] Spall & Snyder[100] and Lucca-Negro & O'Doherty.[66] Considering all these studies, it appears that a complete scenario is still to be proposed and approved. Another weak point is the constant simplification of the problem made by imposing well-defined boundary conditions mimicking the presence of lateral walls, closer to experiments inside a pipe or a straight cylinder than to vortex breakdown phenomena as they occur in nature.

1.4 Outline of the thesis

This dissertation is a numerical and analytical investigation of the axisymmetric vortex breakdown under the assumption of *open* lateral and outlet boundaries. Therefore it sheds light on a wider range of physical phenomena involving vortex breakdown.

The present thesis consists of three chapters. In chapter I an overview of the numerical tools employed in this work is presented. Chapter I also discuses the numerical resolution issues relative to numerical simulation, as well as the validation of the obtained results.

Chapter II is dedicated to the discussion of the effect of viscosity on the vortex breakdown solution. Chapter II also describes the asymptotic analysis of the solution behavior, the results of the numerical simulations and their robustness with respect to numerical accuracy.

In the first part of chapter III we present the effect of an external pressure gradient on the structure of the viscous vortex breakdown solution obtained numerically. We compare these results to the theoretical predictions. The second part of chapter III focuses on the temporal dynamics of the axisymmetric vortex breakdown solution with a recirculation zone near the viscous critical point $S_{c\nu 1}$. In the last part of chapter III we discuss the temporal stability characteristics of the three-dimensional rotating flow with recirculation bubble. Finally, all the results and perspectives for future work are summarized in the Conclusions.

The appendix contains a validation of the numerical continuation algorithm in the case of a simple one-dimensional problem.

2 Numerical Methodology

This chapter is dedicated to the explanation of the numerical techniques used throughout this dissertation. The mathematical model and the direct numerical simulation algorithm are described in details. We present two methods for the stabilization of unstable steady solutions, namely the Selective Frequency Damping (SFD) and the Recursive Projection Method (RPM). A method for continuation along the corresponding solution branches is presented, based on the RPM algorithm. The last part of this chapter discusses the validation of the numerical code and the related spatial resolution issues.

2.1 Mathematical model

As mentioned in the Introduction, the aim of the present study is to shed light on the physical behavior and stability characteristics of vortex breakdown in an open flow. The current mathematical flow model consists of an approximation of the flow geometry, and governing equations which describe the physics of the flow inside the considered domain.

2.1.1 Flow Configuration

Figure 2.1 shows a schematic diagram of a turbulent jet in a cylindrical domain of outer radius R and axial length x_0. Cylindrical coordinates are used, where x, r, and θ denote the axial, radial, and azimuthal directions, respectively.
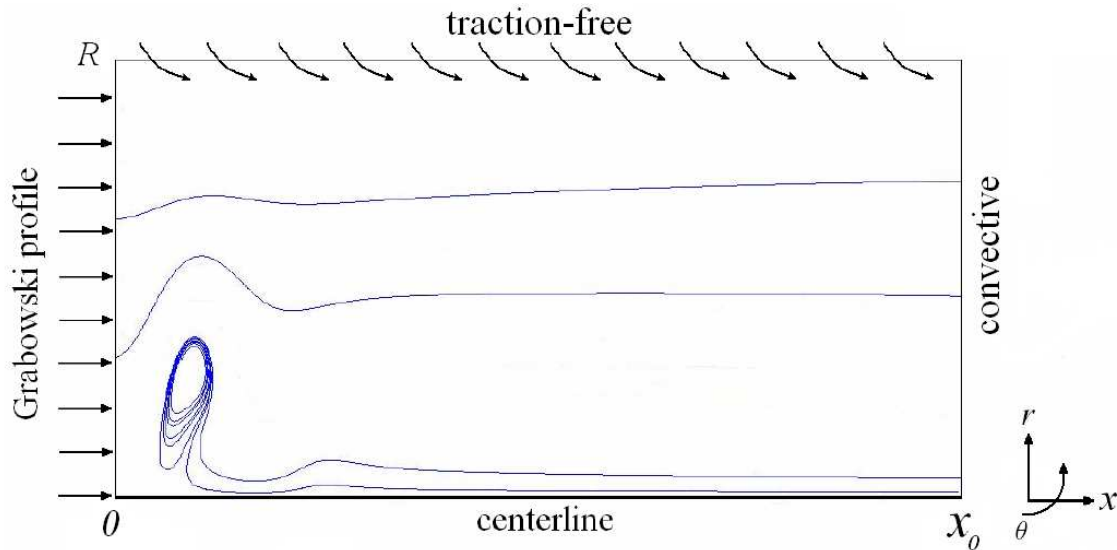
Figure 2.1: A schematic diagram of the flow configuration.

The flow enters through the inlet (located on the left of the domain in figure 2.1). The characteristic radius of the jet vortex core under investigation is r_{core}. The characteristic velocity is chosen as the inlet axial velocity, u_{x0}. As the jet develops downstream, ambient fluid is entrained into the flow. The main purpose of the simulation is to leave the boundaries open to model the behavior of the fluid passing through them. In this case, the flow outside the domain of interest can affect the flow inside. In order for the jet flow to exit the domain, the outlet boundary must also remain open. The open outlet boundary allows for the propagation of disturbances into the inside flow which is essential for the vortex breakdown phenomenon.

2.1.2 Equations of motion

In the previous section details of the flow configuration associated with the boundaries of the cylindrical domain were considered. This section is dedicated to the equations describing the motion of unsteady, axisymmetric, incompressible viscous fluid in the absence of gravity. In order to derive this system of equations, conservation of mass and momentum of fluid must be considered. The use of non-dimensional quantities allows the resulting system to be easily applied to a broad range of similar problems.

Swirling flow is described by several physical and geometrical parameters such as the radius of the vortex core, r_{core}, the inlet axial u_{x0}, radial u_{r0} and azimuthal $u_{\theta 0}$ velocity components, viscosity and density ρ. These parameters can be combined to form two non-dimensional parameters: the Reynolds number Re and the swirl number S. As mentioned above we consider an incompressible fluid with constant density, $\rho = 1$. The Reynolds number is here defined as

$$Re = \frac{u_{x0} r_{core}}{\nu},$$

where ν is the kinematic viscosity of the fluid. The second important non-dimensional parameter is the swirl number, defined as the ratio of the azimuthal velocity at the edge of the core to the axial freestream velocity at the inlet:

$$S = \frac{u_{\theta 0}(r_{core})}{u_{x0}}.$$

We nondimensionalize equations of motions with the following characteristic quantities:

- length $[L] = r_{core}$

- density $[\rho] = 1$

- velocity $[U] = u_{x0}$

- time $[T] = \frac{r_{core}}{u_{x0}}$.

The definition of the swirl parameter S implies $u_{\theta 0}(r = 1) = S$ for the azimuthal velocity profile at the inlet.

After nondimensionalization the axisymmetric Navier-Stokes and continuity equations read:

$$\frac{\partial u_x}{\partial t} + u_x \frac{\partial u_x}{\partial x} + u_r \frac{\partial u_x}{\partial r} + \frac{\partial p}{\partial x} - \frac{1}{Re}\left(\frac{\partial^2 u_x}{\partial x^2} + \frac{\partial^2 u_x}{\partial r^2} + \frac{1}{r}\frac{\partial u_x}{\partial r}\right) = 0,$$
$$\frac{\partial u_r}{\partial t} + u_x \frac{\partial u_r}{\partial x} + u_r \frac{\partial u_r}{\partial r} - \frac{u_\theta^2}{r} + \frac{\partial p}{\partial r} - \frac{1}{Re}\left(\frac{\partial^2 u_r}{\partial x^2} + \frac{\partial^2 u_r}{\partial r^2} + \frac{1}{r}\frac{\partial u_r}{\partial r} - \frac{u_r}{r^2}\right) = 0, \quad (2.1)$$
$$\frac{\partial u_\theta}{\partial t} + u_x \frac{\partial u_\theta}{\partial x} + u_r \frac{\partial u_\theta}{\partial r} + \frac{u_r u_\theta}{r} - \frac{1}{Re}\left(\frac{\partial^2 u_\theta}{\partial x^2} + \frac{\partial^2 u_\theta}{\partial r^2} + \frac{1}{r}\frac{\partial u_\theta}{\partial r} - \frac{u_\theta}{r^2}\right) = 0,$$

$$\frac{\partial u_x}{\partial x} + \frac{1}{r}\frac{\partial}{\partial r}\left(ru_r\right) = 0.$$

It is important to note that we will use only non-dimensionalized parameters and equations in the following sections.

2.1.3 Boundary conditions

At the inlet, the Grabowski profile [37] is used for the radial velocity, where axial and azimuthal velocity components are defined piecewise for the regions inside and outside of a characteristic radius. The Grabowski profile represents a smooth change from solid body rotation inside the characteristic radius to a potential flow farther away, see figure 2.2.
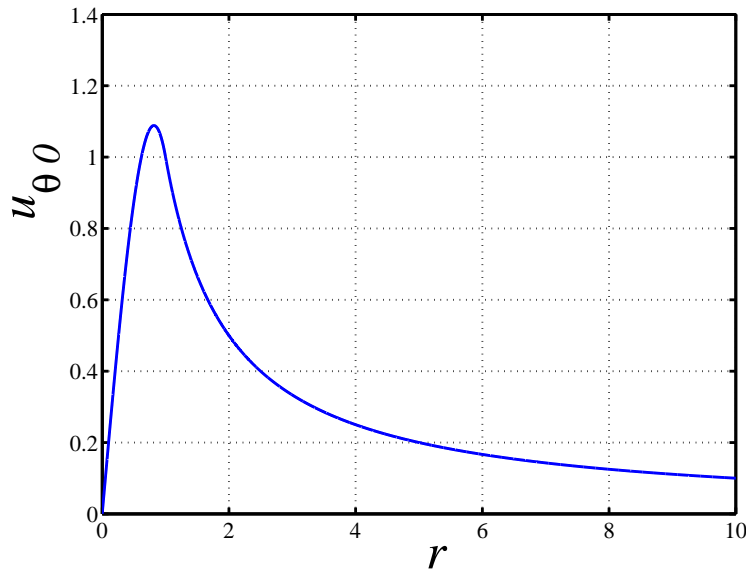
Figure 2.2: Dependence of the azimuthal velocity component on the radius for the Grabowski profile. [37]

The velocity profile at the inflow boundary is assumed to be axisymmetric and constant over time

$$
\begin{aligned}
&u_x(0,r) = 1,\\
&u_r(0,r) = 0,\\
&u_\theta\left(0, 0 \le r \le 1\right) = Sr(2 - r^2),\\
&u_\theta\left(0, 1 \le r\right) = S/r.
\end{aligned}
\tag{2.2}
$$

The inlet condition at $x = 0$ was chosen in order to approximate the experimentally-measured velocity in vortex cores such as those of trailing vortices, and were used by Mager[68] in his analytical investigation of vortex breakdown.

As previously mentioned, the lateral boundary must remain open to allow entrainment of the external fluid into the domain. To accomplish this goal, a no normal viscous traction boundary condition in the radial direction is used [14]

$$\tau \cdot \boldsymbol{n} = 0$$

where τ represents the viscous stress tensor and $\boldsymbol{n}$ stands for the unit normal vector in the lateral directions. In cylindrical coordinates this equation can be rewritten in component form as

$$
\begin{aligned}
\frac{\partial u_r}{\partial r}(x, R) &= 0, \\
\frac{\partial u_r}{\partial x}(x, R) + \frac{\partial u_x}{\partial r}(x, R) &= 0, \\
\frac{\partial u_\theta}{\partial r}(x, R) - \frac{u_\theta}{r}(x, R) &= 0.
\end{aligned}
\tag{2.3}
$$

In order to allow for mass and momentum to be exchanged across the outlet boundary, the outflow convective boundary conditions used in the numerical computations read

$$\frac{\partial u_x}{\partial t} + C\frac{\partial u_x}{\partial x} = 0, \quad \frac{\partial u_r}{\partial t} + C\frac{\partial u_r}{\partial x} = 0, \quad \frac{\partial u_\theta}{\partial t} + C\frac{\partial u_\theta}{\partial x} = 0. \tag{2.4}$$

Following Ruith et al.[79] we choose the convective velocity to be $C = 1$. In the steady case, equations (2.4) reduce to

$$\frac{\partial u_x}{\partial x} = 0, \quad \frac{\partial u_r}{\partial x} = 0, \quad \frac{\partial u_\theta}{\partial x} = 0,$$

which has the advantage not to depend on the value of C.

Due to the axisymmetry of the flow, we also impose the conditions $u_r(x, 0) = 0$ and $u_\theta(x, 0) = 0$ at the centerline.

2.2 Direct Numerical Simulation

In order to carry out the research contained in this dissertation, a computer code has been adapted based on the code developed by Nichols [72] (calculation of reacting jets in the low Mach number approximation) to study constant-density viscous axisymmetric rotating flows. The system of partial differential equations is solved by a fourth-order Runge-Kutta scheme in time and a sixth-order discretization scheme in space similar to the one used in Ref.[72, 20]. Due to the complexity of the code, not every detail can be discussed. This section provides an overview of the algorithm used and then focuses on a few numerical issues that arose during the code development.

2.2.1   Mesh

The DNS code solves the Navier-Stokes equations and the continuity equation in cylindrical coordinates (2.1) on a staggered mesh, with highly accurate cell-centered sixth-order compact schemes discussed by Lele[62] (with the Fully Included Metrics (FIM), discretization of a differential equation and evaluation of derivatives directly on a nonuniform grid, which is based on the Taylor series expansion) used to compute spatial derivative in the x and r directions. The benefits of a staggered mesh include a more accurate representation of advection for large scales, but staggering also eliminates numerical modes with upstream propagating group velocity which otherwise would influence the stability properties of the overall flow.

In order to achieve a high resolution in the radial direction an algebraically mapped mesh was used[43]. Following Ref.[96], it is important to control the number of points in a specified subsection of the physical domain in order to achieve high accuracy. In the current investigation the flow dynamics dominates the area close to the centerline, leading to a local flow deceleration and the rise of recirculation region. The dynamics of the flow at the lateral boundary is important as well, since it allows for the entrainment of the external flow into the computational domain. Therefore the following mapping was used to cluster grid points near the lateral boundary $r = R$ and put half the grid points in the interior (most important) region $0 \leq r \leq R_{int}$

$$r = a\frac{1 + \hat{r}}{b - \hat{r}}, \quad -1 \leq \hat{r} \leq 1,$$

where

$$a = \frac{R_{int}R}{R - 2R_{int}}, \quad b = 1 + \frac{2a}{R}.$$

The grid point separation for this mapping is presented in the figure 2.3 as a function of the radius. A uniform mesh is used in the axial direction.

2.2.2   Boundary conditions

'Boundary conditions are sometimes said to be the 'bane' of computational fluid dynamics', see Ref. [71]. As was mentioned in the previous section, open boundaries (such as the lateral and outlet boundaries in the current problem) are especially challenging due to the fact that an effective boundary condition must model the motion of the fluid outside the computational domain, for which no information exists. In addition, while cylindrical coordinates have many advantages for the simulation of round jets, they introduce an apparent singularity in the governing equation at the centerline $r = 0$. Even if the centerline is not a true physical boundary, it must be treated carefully in order to avoid numerical difficulties associated with the apparent singularity.
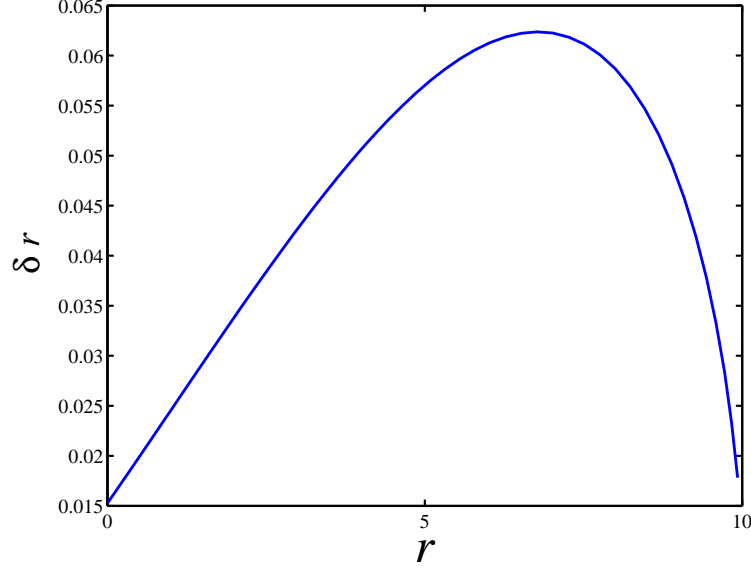
Figure 2.3: The distance between grid points as a function of radius; here we assumed that $R_{max} = 10$, $R_{int} = 2$, and the resolution in the radial direction is equal to 127 points.

Lateral boundary

As emphasized above, the lateral boundary must remain open to allow entrainment of fluid into the jet. To accomplish this goal, the zero normal viscous traction boundary condition (2.3) is used. To apply this boundary condition we must approximate derivatives in the radial and axial directions on the lateral boundary.
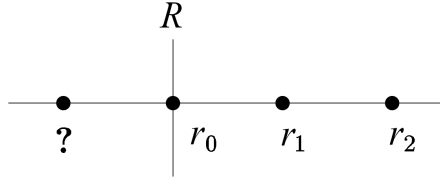
Figure 2.4: The discretization in the radial direction on the lateral boundary.

The radial derivative of any velocity component u_0 (the index 0 corresponds to the position on the lateral boundary $r = R$, see figure 2.4) can be written using one-sided approximations:

$$\left(\frac{\partial u}{\partial r}\right)_0 = \alpha u_0 + \beta u_1 + \gamma u_2,$$

where

$$\alpha = \frac{k_1 + k_2}{k_1 k_2}, \qquad \beta = -\frac{k_2}{(k_1)^2 - k_1 k_2}, \qquad \gamma = -\frac{k_1}{(k_2)^2 - k_1 k_2},$$

with $k_1 = R(0) - R(1)$ and $k_2 = R(0) - R(2)$. In this way the boundary conditions (2.3)

23

discretized in the r direction are:

$$(u_r)_0 = -\frac{\beta}{\alpha}(u_r)_1 - \frac{\gamma}{\alpha}(u_r)_2,$$

$$(u_x)_0 = -\frac{\beta}{\alpha}(u_x)_1 - \frac{\gamma}{\alpha}(u_x)_2 - \frac{1}{\alpha}\left(\frac{\partial u_r}{\partial x}\right)_0,$$

$$(u_\theta)_0 = -\frac{\beta}{\alpha - 1/R}(u_\theta)_1 - \frac{\gamma}{\alpha - 1/R}(u_\theta)_2.$$

The above equations are ordered so that u_r is computed at the boundary first, which is then used to calculate u_x at the boundary.

A compact scheme is used to compute the x derivatives, since this technique does not involve a significant amount of extra computations. The computations of $r-$ derivatives via compact schemes, however, would entail the involvement of data from the entire domain; for this reason one-sided differences are employed. Furthermore, the compact schemes themselves involve one-sided differences near the boundary and thus induce a loss accuracy near the boundary. Therefore, for additional accuracy at the lateral boundary a higher order one-sided finite difference scheme may be selected.

As mentioned before, the convective boundary condition for each velocity flux component (2.4) is imposed at the outlet. This boundary condition, also known as a non-reflective, radiative, absorbing or advective condition is spatially and temporally local and thus computationally very efficient to implement. In order to do so, a simple one-sided finite difference is used to approximate the $x-$ derivative at the outlet in (2.4). It was found that this naive discretization is sufficient and numerically efficient.

Centerline treatment

The centerline boundary condition used for the numerical simulations in this thesis was adapted from that of Constantinescu & Lele[19]. To derive the centerline boundary condition, we consider the following series expansion of a single-valued variable, S, about the centerline for the axisymmetric case (no dependance on the angle θ):

$$S(r) = \sum_{n=0}^{\infty} a_n r^{2n}. \tag{2.5}$$

This result can easily be obtained by considering the symmetry with respect to $r = 0$.

At the centerline the above expansion reduces trivially to: $S(0) = a_0$. And the centerline condition for the r-derivative is $\frac{\partial S}{\partial r}(0) = 0$. According to Constantinescu & Lele[19] the power series expansion for a multi-valued variable, M, takes a slightly modified form:

$$M(r) = \sum_{n=1}^{\infty} a_n r^{2n-1},$$

24

meaning that in the limit $r \to 0$, $M(0) = 0$ and $\dfrac{\partial M}{\partial r}(0) = a_1$. Summarizing the above, the complete centerline condition for a single-valued variable is $\dfrac{\partial S}{\partial r}(0) = 0$ and for a multi-valued variable is $M(0) = 0$.

We define $\mathbf{r}$ as a unit vector pointing away from the centerline. This vector changes direction across the centerline, which means that certain flow variables change sign to compensate and thus are multi-valued at the centerline. This occurs due to the definition of the coordinate system and does not depend on any sort of physical discontinuity. Considering the flow convecting perpendicularly to the centerline, the radial velocity u_r is negative as the flow approaches the centerline from one side and then changes to being positive as soon as the flow crosses the centerline and starts moving away from it; from a physical point of view, however, it remains continuous.

A key property in the relation between single-valued and multi-valued variables in cylindrical coordinates is that taking the radial derivative of a single-valued variable will result in a variable that can be multi-valued at the centerline. Therefore, the multi-valued variables must be antisymmetric in the vicinity of the centerline; the converse is also true, meaning that taking the r-derivative of a multi-valued variable will yield a single-valued variable. Multiplying or dividing by r has the same effect, changing between single and multi-valued variables. Therefore, the variables:

$$u_x, \quad u_x\frac{\partial u_x}{\partial x}, \quad u_r\frac{\partial u_x}{\partial r}, \quad \frac{\partial^2 u_x}{\partial x^2}, \quad \frac{\partial^2 u_x}{\partial r^2}, \quad \frac{1}{r}\frac{\partial u_x}{\partial r}, \quad \frac{1}{r}\frac{\partial(ru_r)}{\partial r},$$

are single-valued at the centerline, while the variables:

$$u_r, \quad u_r\frac{\partial u_r}{\partial r}, \quad \frac{u_\theta^2}{r}, \quad \frac{\partial^2 u_r}{\partial x^2}, \quad \frac{\partial^2 u_r}{\partial r^2}, \quad \frac{1}{r}\frac{\partial u_r}{\partial r}, \quad \frac{u_r}{r^2},$$

and

$$u_\theta, \quad u_r\frac{\partial u_\theta}{\partial r}, \quad \frac{u_r u_\theta}{r}, \quad \frac{\partial^2 u_\theta}{\partial x^2}, \quad \frac{\partial^2 u_\theta}{\partial r^2}, \quad \frac{1}{r}\frac{\partial u_\theta}{\partial r}, \quad \frac{u_\theta}{r^2}$$

are multi-valued at the centerline. For the radial and azimuthal momentum equation at the centerline, diffusion and convection terms are assumed to be zero.

Since u_x is a single-valued variable, using the expansion (2.5) around the centerline:

$$u_x(x, r) = \sum_{n=0}^{\infty} a_n(x)r^{2n} = a_0(x) + \sum_{n=1}^{\infty} a_n(x)r^{2n},$$

we get:

$$\frac{\partial^2 u_x}{\partial r^2}(x, 0) = \frac{\partial u_x}{\partial r}\left(\sum_{n=1}^{\infty} 2na_n(x)r^{2n-1}\right)(0) = \left(\sum_{n=1}^{\infty} 2n(2n-1)a_n(x)r^{2n-2}\right)(0) = 2a_1(x)$$

and

$$\frac{1}{r}\frac{\partial u_x}{\partial r}(x,0) = \left(\frac{1}{r}\sum_{n=1}^{\infty} 2n a_n(x) r^{2n-1}\right)(0) = 2a_1(x).$$

Hence at the centerline the singular term in the axial momentum equation $\frac{1}{r}\frac{\partial u_x}{\partial r}$ is equal to $\frac{\partial^2 u_x}{\partial r^2}$. The same way it can be shown that $\frac{1}{r}\frac{\partial(r u_r)}{\partial r} = 2\frac{\partial u_r}{\partial r}$ in the continuity equation.

Taking into account all the above, the full incompressible Navier-Stokes equations (2.1) on the centerline have the form:

$$\frac{\partial u_x}{\partial t}(x,0) + u_x\frac{\partial u_x}{\partial x}(x,0) + \frac{\partial p}{\partial x}(x,0) - \frac{1}{Re}\left(\frac{\partial^2 u_x}{\partial x^2}(x,0) + 2\frac{\partial^2 u_x}{\partial r^2}(x,0)\right) = 0,$$
$$\frac{\partial u_r}{\partial t}(x,0) = 0,$$
$$\frac{\partial u_\theta}{\partial t}(x,0) = 0,$$
$$\frac{\partial u_x}{\partial x}(x,0) + 2\frac{\partial u_r}{\partial r}(x,0) = 0.$$

Most of the numerical error associated with compact differencing are due to the one-side differences near the boundaries. This can cause serious problems for computing radial derivatives on a cylindrical mesh, if the compact derivative is taken from the centerline in the lateral direction. Since the centerline forms an endpoint for the compact scheme, the numerical errors will tend to concentrate about the centerline in this case. In order to avoid such numerical errors near the centerline, Constantinescu & Lele[19] suggest computing radial derivatives across the entire domain, from one lateral boundary to the other. This tends to concentrate numerical errors due to the differencing scheme near the lateral boundaries only, away from the region of interest. The computation is then performed in the full domain $(-R < r < R, 0 < x < x_0)$. In that case, data fields may be associated with a unit vector which changes sign across the centerline; such fields include the radial and azimuthal velocities. Data values mapped to $(-R, x_0)$ must be multiplied by -1 for consistency at the centerline.

2.2.3 Projection method

A popular numerical solution for Navier-Stokes equations is based on operator splitting. This means the system (2.1) is split into a series of simpler equations, such as an advection-diffusion equation, a Poisson equation, and updates. The evolution of the velocity consists of two main steps. First we compute a predicted velocity, later the velocity is corrected by projection onto divergence-free vector fields.

Here, for simplicity the governing equations (2.1) are conveniently rewrite in operator form

$$\frac{\partial \mathbf{u}}{\partial t} + \mathbf{u} \cdot \nabla \mathbf{u} = -\nabla p + \frac{1}{Re} \nabla^2 \mathbf{u}, \tag{2.6}$$

together with the equation of continuity

$$\nabla \cdot \mathbf{u} = 0, \tag{2.7}$$

where $\mathbf{u}$ is the entire velocity field $(u_x, u_r, u_\theta)^T$.

The simplest discretization in time leads to an expression for the velocity at the $n+1$ step:

$$\mathbf{u}^{n+1} = \mathbf{u}^n + \triangle t \left(-\mathbf{u}^n \cdot \nabla \mathbf{u}^n - \nabla p^n + \frac{1}{Re} \nabla^2 \mathbf{u}^n \right),$$

where $\triangle t$ is the time step, and $\mathbf{u}^n$ is the velocity at time step n. It can be easily shown that the velocity $\mathbf{u}^{n+1}$ from the expression above does not satisfy the continuity equation (2.7), *i.e.* $\mathbf{u}^{n+1}$ is not yet the velocity at the new time level $n+1$. Instead, this velocity can be considered as a predicted $\mathbf{u}^*$, and the velocity at time level $n+1$ can be found as $\mathbf{u}^{n+1} = \mathbf{u}^* + \mathbf{u}^c$, where $\mathbf{u}^c$ is a correction.

The predicted velocity is calculated from

$$\mathbf{u}^* = \mathbf{u}^n + \triangle t \left(-\mathbf{u}^n \cdot \nabla \mathbf{u}^n + \frac{1}{Re} \nabla^2 \mathbf{u}^n \right) \tag{2.8}$$

with proper boundary conditions which will be derived below. As one can see for the predicted velocity we do not use the pressure computed at the previous time step n. This projection method is often referred to as the pressure-free projection method. [18]

The velocity at time level $n+1$ is

$$\mathbf{u}^{n+1} = \mathbf{u}^n + \triangle t \left(-\mathbf{u}^n \cdot \nabla \mathbf{u}^n - \nabla p^{n+1} + \frac{1}{Re} \nabla^2 \mathbf{u}^n \right)$$

Subtracting equation (2.8) from the equation above one yields an expression for $\mathbf{u}^c$:

$$\mathbf{u}^c = \mathbf{u}^{n+1} - \mathbf{u}^* = -\triangle t \nabla p^{n+1},$$

that is

$$\mathbf{u}^{n+1} = \mathbf{u}^* + \mathbf{u}^c, \quad \mathbf{u}^c = -\triangle t \nabla p^{n+1}.$$

The velocity $\mathbf{u}^{n+1}$ must satisfy the continuity equation (2.7)

$$\nabla \cdot \mathbf{u}^{n+1} = \nabla \cdot \mathbf{u}^* + \nabla \cdot \mathbf{u}^c = \nabla \cdot \mathbf{u}^* - \triangle t \nabla^2 p^{n+1} = 0,$$

which leads to a Poisson equation for the pressure p^{n+1}

$$\nabla^2 p^{n+1} = \frac{1}{\triangle t} \nabla \cdot \mathbf{u}^*. \tag{2.9}$$

The solution of the Poisson equation will be described in the next section.

After computing p^{n+1} from (2.9) the velocity must be updated

$$\mathbf{u}^{n+1} = \mathbf{u}^* - \triangle t \nabla p^{n+1}. \tag{2.10}$$

Now we need to find the proper boundary conditions for $\mathbf{u}^*$:

$$\mathbf{u}^* = \mathbf{u}^{n+1} + \triangle t \nabla p^{n+1}.$$

The velocity at the new time level must satisfy the following inlet boundary conditions

$$\mathbf{u}^{n+1}(0, r) = \mathbf{g}(r) \tag{2.11}$$

where $\mathbf{g}$ is a vector-function of the inlet profile (2.2). Substitution (2.11) into the expression for the predicted velocity gives the inlet boundary condition

$$\mathbf{u}^*(0, r) = \mathbf{g}(r) + \triangle t \nabla p^{n+1}(0, r).$$

When calculating $\mathbf{u}^*$ we still have no information about p^{n+1}, which is needed to impose the proper inlet boundary condition for the predicted velocity $\mathbf{u}^*$. We, therefore, take the pressure from the previous time step n:

$$\mathbf{u}^*(0, r) = \mathbf{g}(r) + \triangle t \nabla p^n(0, r). \tag{2.12}$$

The inlet boundary condition for the predicted velocity must satisfy the following condition:

$$u_x^*(0, r) = u_{x0}$$
$$u_r^*(0, r) = \triangle t \frac{\partial p^n}{\partial r}(0, r)$$
$$u_\theta^*(0, r) = u_{\theta 0}.$$

The splitting algorithm can be summarized as follows:
1) Compute the predicted velocity $\mathbf{u}^*$ from (2.8) with boundary conditions (2.12).
2) Compute p from the Poisson equation (2.9).
3) Compute the new velocity $\mathbf{u}^{n+1}$ from equation (2.10).

2.2.4 Poisson equation

To solve the Poisson equation (2.9) boundary conditions for the pressure have to be employed. Since the inlet profile (2.2) is fixed and since diffusion terms can be neglected (the boundary layer is almost 16 times smaller than Δx even for the smallest Reynolds numbers $Re = 200$), the pressure at the inlet for the axisymmetric case must be a solution of the following system:

$$u_x \frac{\partial u_x}{\partial x} + \frac{\partial p}{\partial x} = 0,$$
$$u_x \frac{\partial u_r}{\partial x} - \frac{u_\theta^2}{r} + \frac{\partial p}{\partial r} = 0.$$

Since the inlet radial velocity is zero, it can be shown from the continuity equation that $\frac{\partial u_x}{\partial x}(0, r) = 0$, giving the following condition for the pressure at the inlet:

$$\frac{\partial p}{\partial x}(0, r) = 0. \tag{2.13}$$

For the outlet boundary commonly a homogeneous Dirichlet condition is used, $p(x_0, r) = 0$. However, in the current case we have to compensate for the centrifugal force created by the azimuthal rotation which yields $\frac{\partial p}{\partial r} \neq 0$ at the outlet leading to[78]:

$$\frac{\partial p}{\partial x}(x_0, r) = 0. \tag{2.14}$$

Following Boersma[14] for the case of open jets we can impose the Dirichlet condition on pressure at the lateral boundary $p(x, R) = 0$.

The axisymmetric Poisson equation (2.9) in cylindrical coordinates has the form:

$$\frac{\partial^2 p}{\partial x^2} + \frac{\partial^2 p}{\partial r^2} + \frac{1}{r}\frac{\partial p}{\partial r} = f,$$
$$f = \frac{1}{\triangle t}\nabla \cdot \mathbf{u}^* = \frac{1}{\triangle t}\left(\frac{\partial u_x^*}{\partial x} + \frac{1}{r}\frac{\partial}{\partial r}(ru_r^*)\right). \tag{2.15}$$

Taking into account inlet and outlet boundary conditions (2.13)-(2.14) we can apply the forward cosine FFT with $\lambda = \pi/x_0 i$, where i is an integer (for more details see Ref.[21]), which reduces the problem to the solution of the following 1-dimensional Poisson equation:

$$L(r) = \frac{\partial^2 \tilde{p}}{\partial r^2} + \frac{1}{r}\frac{\partial \tilde{p}}{\partial r} - \lambda^2 \tilde{p} = \tilde{f}.$$

Using the previous centerline treatment this equation evaluated at $r = 0$ reduces to

$$L(r) = 2\frac{\partial^2 \tilde{p}}{\partial r^2} - \lambda^2 \tilde{p} = \tilde{f}.$$

Given $\tilde{f}$ we want to solve for $\tilde{p}$, using the following compact scheme at each grid index i:

$$\alpha \tilde{p}_{i-1} + \tilde{p}_i + \beta \tilde{p}_{i+1} = a\tilde{f}_{i-1} + b\tilde{f}_i + c\tilde{f}_{i+1}. \tag{2.16}$$

In terms of $\tilde{p}$ and its derivatives at position i,

$$\tilde{p}_{i-1} = \sum_{n=0}^{N} \frac{1}{n!} \frac{\partial^n \tilde{p}}{\partial r^n} (-k_1)^n,$$
$$\tilde{p}_{i+1} = \sum_{n=0}^{N} \frac{1}{n!} \frac{\partial^n \tilde{p}}{\partial r^n} (k_2)^n,$$
$$\tilde{f}_{i-1} = \sum_{n=0}^{N} \frac{1}{n!} \frac{\partial^n L(r)}{\partial r^n} (-k_1)^n,$$
$$\tilde{f}_i = L(r),$$
$$\tilde{f}_{i+1} = \sum_{n=0}^{N} \frac{1}{n!} \frac{\partial^n L(r)}{\partial r^n} (k_2)^n,$$

where $k_1 = r_i - r_{i-1}$ and $k_2 = r_{i+1} - r_i$. For a variable mesh, like the one used in the code, we have $k_1 \neq k_2$. The above expansions are substituted into the compact scheme (2.16); and we then solve for α, β, a, b, c so that the lowest order terms exactly cancel. This is accomplished using the following Maple code:

```
 1: restart;
 2: numterms := 4:
 3: T1 := add(p[n]*delta^n/n!, n=0..numterms):
 4: L(r) := diff(p(r),r,r) + diff(p(r),r)/r - (lambda^2)*p(r);
 5: T2 := add(subs([seq(diff(p(r),[seq(r,i=1..ii)])=p[ii], ii=0..numterms+2)],
    diff(L(r), [seq(r,i=1..n)]))*delta^n/n!, n=0..numterms);
 6: P1 := subs(delta=-k[1], T1):
 7: P2 := subs(delta=0, T1):
 8: P3 := subs(delta=k[2], T1):
 9: F1 := subs(delta=-k[1], T2):
10: F2 := subs(delta=0, T2):
11: F3 := subs(delta=k[2], T2):
12: Truncation := alpha*P1 + P2 + beta*P3 - a*F1 - b*F2 - c*F3:
13: Truncation := collect(Truncation, [seq(p[i],i=0..numterms+2)]):
14: Trunc_coeffs := [seq(coeff(Truncation, p[i]), i=0..numterms+2)]:
15: sols := simplify(solve({seq(Trunc_coeffs[i]=0, i=1..5)}, {alpha, beta, a, b, c})):
16: simplify(subs(k[1]=Delta, k[2]=Delta, subs(sols, Trunc_coeffs)));
```

17: lhs(sols[4]);
18: subs(k[1]=2*r, k[2]=r, sols[4]);
19: CodeGeneration[Fortran](subs(k[1]=k1, k[2]=k2, convert(sols, list)), optimize=true, declare=[k1::float, k2::float, r::float, kk::float, nn::float]);

In this program the variables T1 and T2 (lines 3 and 5, respectively) define the general series expansion. The number N of terms retained is controlled by the variable 'numterms' defined on line 2. Using this general expansions we can calculate expansion for $\tilde{p}_{i-1}$, $\tilde{p}_{i+1}$, $\tilde{f}_{i-1}$ and $\tilde{f}_{i+1}$, expressed by the variables P1, P3, F1, F3 (lines from 6 to 11). We then substitute these variables into the expression for the compact scheme (2.16) (line 12), collect coefficients for each derivative of $\tilde{p}$ (line 13) and find values of α, β, a, b and c such that all the coefficients at each derivative of $\tilde{p}$ are exactly zero (line 15). The last statement of the Maple code (line 19) produces a piece of Fortran code to calculate these coefficients.

It is important to note that this calculation is only needed once at the start of the simulation, assuming that the mesh spacing does not change over time. In order to find the pressure $\tilde{p}$ we need to solve the system $A\tilde{p} = \tilde{f}$, where the matrix M is tridiagonal:

$$
\begin{pmatrix}
1 & \beta_1 & 0 & 0 & 0 & \ldots & 0 \\
\alpha_2 & 1 & \beta_2 & 0 & 0 & \ldots & 0 \\
0 & \alpha_3 & 1 & \beta_3 & 0 & \ldots & 0 \\
\ldots & & & & & & \\
0 & 0 & \ldots & \alpha_{N_R-1} & 1 & \beta_{N_R-1} & 0 \\
0 & 0 & \ldots & 0 & \alpha_{N_R-1} & 1 & \beta_{N_R-1} \\
0 & 0 & \ldots & 0 & 0 & \alpha_{N_R} & 1
\end{pmatrix}
\begin{pmatrix}
\tilde{p}_1 \\
\vdots \\
\tilde{p}_{i-1} \\
\tilde{p}_i \\
\tilde{p}_{i+1} \\
\vdots \\
\tilde{p}_{N_R}
\end{pmatrix}
=
\begin{pmatrix}
\tilde{f}_1 \\
\vdots \\
\tilde{f}_{i-1} \\
\tilde{f}_i \\
\tilde{f}_{i+1} \\
\vdots \\
\tilde{f}_{N_R}
\end{pmatrix}.
$$

This system can be easily reduced using the following transformation

$$
\eta_1 = 1, \quad \hat{f}_1 = \frac{\tilde{f}_1}{\eta_1}, \quad \gamma_i = \frac{\beta_{i-1}}{\eta_{i-1}}, \quad \eta_i = 1 - \alpha_i \gamma_i, \quad \hat{f}_i = \frac{\tilde{f}_i - \alpha_i \hat{f}_{i-1}}{\eta_i}, \quad i = 2 \ldots N_R,
$$

to a new system $B\tilde{p} = \hat{f}$, where B is in upper triangular form

$$
\begin{pmatrix}
1 & \gamma_2 & 0 & 0 & \ldots & 0 \\
0 & 1 & \gamma_3 & 0 & \ldots & 0 \\
\ldots & & & & & \\
0 & 0 & \ldots & 0 & 1 & \gamma_{N_R} \\
0 & 0 & \ldots & 0 & 0 & 1
\end{pmatrix}
\begin{pmatrix}
\tilde{p}_1 \\
\vdots \\
\tilde{p}_i \\
\vdots \\
\tilde{p}_{N_R}
\end{pmatrix}
=
\begin{pmatrix}
\hat{f}_1 \\
\vdots \\
\hat{f}_i \\
\vdots \\
\hat{f}_{N_R}
\end{pmatrix}.
$$

This problem is trivially solved by starting from the bottom and substituting backwards:

$$
\tilde{p}_{N_R} = \hat{f}_{N_R}, \quad \tilde{p}_i = \hat{f}_i - \gamma_{i+1}\tilde{p}_{i+1}, \quad i = N_R - 1 \ldots 1.
$$

It is important to note that we need to find α β, a, b, c, γ and η only once at the start of the simulation, assuming that the mesh spacing does not change. The coefficients calculated for a particular mesh spacing are then applied at each timestep of the simulation, when the solution of the Poisson equation is required. After calculating $\tilde{p}$ we do the backward cosine FFT (Ref.[21]) and obtain the physical pressure.

2.3 Steady state solutions

The steady states of interest are particular solutions of the governing equations, though with all time derivatives equal to zero ($\dfrac{\partial \bullet}{\partial t} = 0$). To reach a stable steady state numerically, we can simply use the DNS code: advancement of the time-dependent Navier–Stokes equations can be performed until the L_2-norm of the increment of the velocity field changes less than, say, 10^{-11} over one physical time unit. Two additional numerical techniques were developed here to accelerate the convergence and/or to tackle cases where steady states are linearly unstable.

Consider the general nonlinear system

$$\frac{\partial \mathbf{u}}{\partial t} = f(\mathbf{u}), \quad \mathbf{u} = (u_x, u_r, u_\theta)^T, \tag{2.17}$$

along with the corresponding initial and boundary conditions for $\mathbf{u}$, in our case the system (2.17). A steady state $\mathbf{u}_s$ is then given by

$$\frac{\partial \mathbf{u}_s}{\partial t} = f(\mathbf{u}_s) = 0. \tag{2.18}$$

If the solution $\mathbf{u}_s$ is stable, it will attract all trajectories in the neighborhood, if it is unstable, the system will quickly diverge from $\mathbf{u}_s$.

2.3.1 Selective Frequency Damping (SFD)

The SFD method[1] for computing steady solutions of the system (2.17) proceeds by adding a dissipative relaxation term proportional to the high-frequency content of the velocity fluctuations:

$$\begin{aligned}
\frac{\partial \mathbf{u}}{\partial t} &= f(\mathbf{u}) - \chi(\mathbf{u} - \bar{\mathbf{u}}), \\
\frac{\partial \bar{\mathbf{u}}}{\partial t} &= (\mathbf{u} - \bar{\mathbf{u}})\omega_c.
\end{aligned} \tag{2.19}$$

Here ω_c is the filter cut-off frequency, related to the unstable frequencies to be damped. ω_c should be smaller than all possible unstable frequencies. χ is the control coefficient (or the

control gain). It is related to the unstable growth rates and should be chosen large enough to damp all unstable modes.

As a guideline, Akervik et al.[1] have chosen the regularization parameter χ to be twice the growth rate of the dominant disturbance and have selected the cutoff frequency in such a way that the unstable disturbances are well within the damped region, i.e. $\omega_c \approx 1/2\omega_{dist}$.

It is important to note that SFD only works when the system (2.19), linearized about the sought-after steady state, has only complex unstable eigenvalues. In the case presented in the second chapter of this dissertation, when the steady-state solution corresponds to a standing solitary wave bifurcating from the turning point $S_{c\nu1}$ (see figure 1, Ref. [108]), the most unstable eigenvalue (lying outside the unit circle) is real, which means that there is no frequency to be damped by the method.

In another case of the third chapter, however, when a Hopf bifurcation exists along the vortex breakdown solution branch, we find two complex conjugate unstable eigenvalues, see figure 2.5. In this case, when the frequency and the growth rate of the instability can easily be estimated, SFD shows good convergence, see figure 2.6.
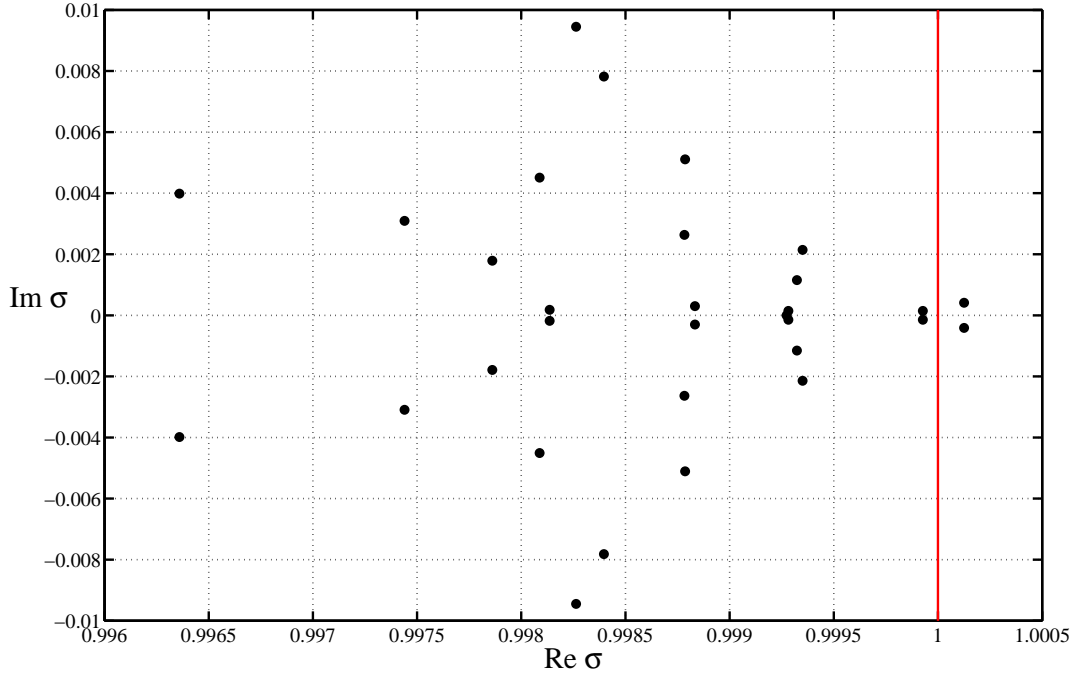
Figure 2.5: Zoom of the spectrum of complex eigenvalues σ of the right-hand side part of the Navier-Stokes equations ($Re = 1000$, $S = 0.743755$, vortex breakdown state). Eigenvalues lying on the right of the red line are unstable.
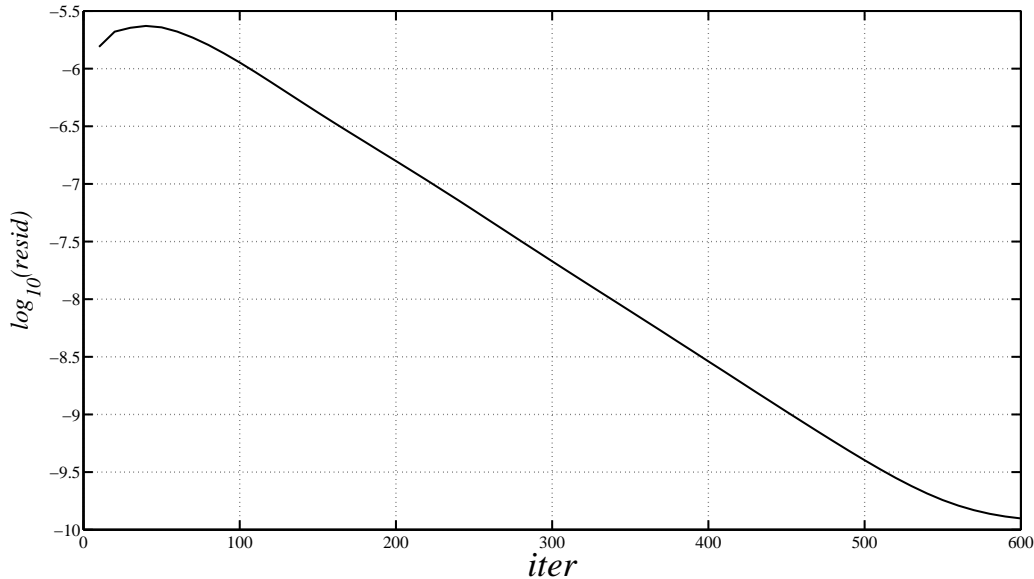
Figure 2.6: Convergence rate for $Re = 1000$, $S = 0.7437553$, vortex breakdown state. Here we deal with two complex conjugate eigenvalues, which determine the growth rate and the frequency of the dominant perturbations, $\sigma = 1.000125$, $\omega_{pert} = 4.122565 \cdot 10^{-4}$.

2.3.2 Recursive Projection Method (RPM)

The RPM[97] stabilizes fixed-point iteration procedures for solving (2.18) by first computing the projection onto the unstable subspace. Within this subspace, an iterative Newton-Raphson iterations is used, while fixed point iterations are used in the complementary subspace. The method is extremely effective compared to standard Newton solvers when the dimension of the unstable subspace is small compared to the dimension of the full system [70, 36, 35].

In order to find the equilibrium solution u_s of the problem (2.18) one frequently employs iterative procedures of the form:

$$u^{n+1} = u^n - Mf(u^n), \tag{2.20}$$

where M is a matrix chosen to produce the convergence in an efficient manner. For example, $M = \dfrac{\partial f}{\partial u}(u^n)$ corresponds to the Newton method.

Regardless of the choice for M the relation (2.20) can be rewritten in the form:

$$F(u^n) \equiv u^n - Mf(u^n).$$

In this case the spatially discretized problem (2.18) can be reduced to the following fixed point iteration scheme (Picard iteration):

$$u^{n+1} = F(u^n), \quad u^n \in \mathbb{R}^N \quad F : \mathbb{R}^N \to \mathbb{R}^N. \tag{2.21}$$

34

The system (2.21) can be linearized around the sought steady state. The Taylor series of $F(u^{n+1})$ at the point $u^{n+1} = u^n + \delta u$ is given by

$$F(u^{n+1}) = F(u^n) + \frac{\partial F}{\partial u}(u^n)\delta u + O((\delta u)^2). \tag{2.22}$$

The first order term $O(\delta u)$ is the Jacobian matrix of F evaluated at $u = u^n$:

$$J(u^n) = \frac{\partial F}{\partial u}(u^n). \tag{2.23}$$

The asymptotic rate of convergence of the fixed point iteration (2.21) is determined by the dominant eigenvalues of the Jacobian matrix J evaluated at the steady solution u_s. Even if initially the associated residual ($||u^{n+1} - u^n||_2$) drops fast, the asymptotic convergence rate, which depends on the dominant eigenvalue (λ_1) of the Jacobian matrix, will be low if the modulus of this eigenvalue is close to one

$$||u_s - u^{n+1}|| \approx |\lambda_1|||u_s - u^n||.$$

If all eigenvalues of J lie within the unit circle, the algorithm is asymptotically convergent in the neighborhood of u_s and the linear asymptotic convergence factor is the modulus of the largest eigenvalue of J. In the case where there are some stable eigenvalues very close to the boundary of the unit circle ($1 - \delta < |\lambda| < 1$, where $\delta \ll 1$), the Picard iteration method converges very poorly. If some eigenvalues lie outside the unit circle, convergence fails.

We suppose here that m eigenvalues λ (typically m is smaller than 10) of the Jacobian matrix lie either outside the unit disk or very close to its boundary, as shown in figure 2.7. We can define a subspace $\mathbb{P}$ associated with the m corresponding eigenvectors. Let Z be an orthonormal basis in $\mathbb{P}$. $Z \in \mathbb{R}^{N \times m}$ satisfies the equations

$$JZ = Z\Lambda,$$
$$Z^T Z = I_m,$$

where $I_m \in \mathbb{R}^{m \times m}$ is the identity matrix and $\Lambda \in \mathbb{R}^{m \times m}$ is a square matrix with eigenvalues $\lambda_1, \ldots, \lambda_m$. We can also define the orthogonal complement $\mathbb{Q} = \mathbb{P}^\perp$ with its orthonormal basis $Z_q^T Z_q = I_{N-m}$. From the definition of $\mathbb{Q}$ it follows that $Z^T Z_q = 0$ and $Z_q^T Z = 0$. $P = ZZ^T$ and $Q = Z_q Z_q^T$ are orthogonal projectors on $\mathbb{P}$ and $\mathbb{Q}$, respectively. Hence the subspaces $\mathbb{P}$ and $\mathbb{Q}$ allow us to split any state u into two parts, the least stable part $p = Pu$ and and its orthogonal complement $q = Qu$:

$$u = Pu + Qu.$$
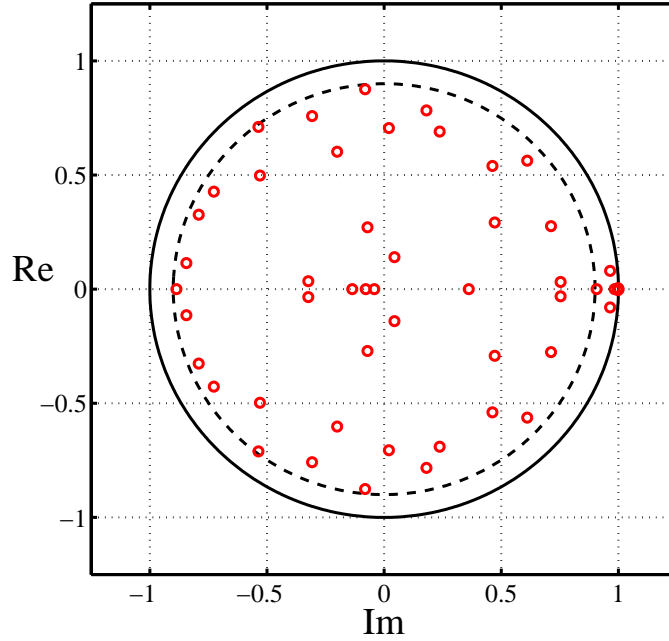
Figure 2.7: The solid line indicates the boundary of the unit disk, the dashed line indicated the boundary of the disk $K_\delta = \{|z| \leq 1 - \delta\}$. Eigenvalues lying outside K_δ are the most unstable.

We can rewrite the iterative formula (2.21) using the unique decomposition:

$$
\begin{aligned}
q^{n+1} &= QF(u^n) = F(u^n) - PF(u^n), \\
p^{n+1} &= PF(u^n) = PF(p^n + q^n), \\
u^{n+1} &= p^{n+1} + q^{n+1}.
\end{aligned}
\tag{2.24}
$$

The Q-part of the present iterative scheme converges if p^n is fixed. However, for fixed q^n the P-part fails to converge. RPM replaces the P-part of the iteration scheme by a Newton step

$$
p^{n+1} = PF(p^{n+1} + q^n).
$$

Using the first order Taylor expansion of $\delta p^n = p^{n+1} - p^n$ we derive the following relation at the first order in $O(\delta p_n)$:

$$
\delta p^n = PJP\delta p^{n-1} + PJQ\delta q^{n-1}.
$$

If P is an accurate projection, $PJQ = 0$.

Since the restriction of the Jacobian J onto the subspace $\mathbb{P}$ is given by the following projection:

$$J_p(u^n) = PJ(u^n)P,$$

the Newton step for p^{n+1} can be rewritten in the following way (here we neglect the terms of order $O((\delta p)^2)$ and higher):

$$(I - J_p(u^n))(p^{n+1} - p^n) = PF(p^n + q^n) - p^n.$$

Hence the *stabilization procedure* has the form

$$\begin{aligned}
q^{n+1} &= F(u^n) - PF(u^n), \\
p^{n+1} &= p^n + (I - J_p(u^n))^{-1}(PF(u^n) - p^n), \\
u^{n+1} &= p^{n+1} + q^{n+1}.
\end{aligned} \tag{2.25}$$

If sufficiently close a fixed point, the Newton iteration converges quadratically. The dimension of the subspace associated with the projection $P = ZZ^T$ is assumed small ($m \ll N$), hence the cost of solving the linear system of equations for the Newton step stays reasonable especially compared to the standard Newton-Raphson scheme which requires the inversion of an $n \times n$ system. The Jacobian matrix is never formed explicitly since it only occurs in the form of matrix-vector products. We express the action of the Jacobian matrix via a finite-difference approximation. With $Z = [Z_1 \ldots Z_m] \in \mathbb{R}^{N \times m}$ we form:

$$JZ_i \approx \frac{1}{\epsilon_i}[F(u + \epsilon_i Z_i) - F(u)], \quad \epsilon_i = 10^{-7}\frac{||u||}{||Z_i||}, \quad i = 1 \ldots m. \tag{2.26}$$

In this way applying J to each column of Z requires only one additional evaluation of the function $F(u + \epsilon_i Z_i)$. Usually it is sufficient to use a first-order finite-difference scheme, since the error $O(\epsilon^2)$ is in general smaller than the error associated with, for example, the approximate projections.

If we are close to a fixed point, the extracted basis will be sufficiently accurate. By monitoring the convergence of the Q-part we can identify the dominant eigenspace. Using a Taylor expansion of $\Delta q^n = q^{n+1} - q^n$, we derive the following relation:

$$\Delta q^n = QJQ\Delta q^{n-1} + QJP\Delta p^{n-1}.$$

If P is an exact projection of an invariant subspace of J, we have $QJP = 0$. If the rate of convergence of q^n degrades we can suppose that some of eigenvalues of QJQ are approaching the unit circle. Analytically the above expression on recursion gives $\Delta q^n = (QJQ)^n \delta q^0$. Asymptotically these vectors will tend to converge towards dominant (least

stable) eigenspace of QJQ. Hence, these vectors $\{\Delta q^n, \Delta q^{n-1}, \ldots, \Delta q^{n-L+1}\}$ form an approximate L-dimensional Krylov space for the projected Jacobian QJQ. However, since we do not know J, we monitor Δq^n from Picard iterations for q (2.25):

$$\Delta q^n = q^{n+1} - q^n, \quad \Delta q^{n-1} = q^n - q^{n-1} \ldots.$$

A geometrical interpretation of the above procedure is shown on figure 2.8.
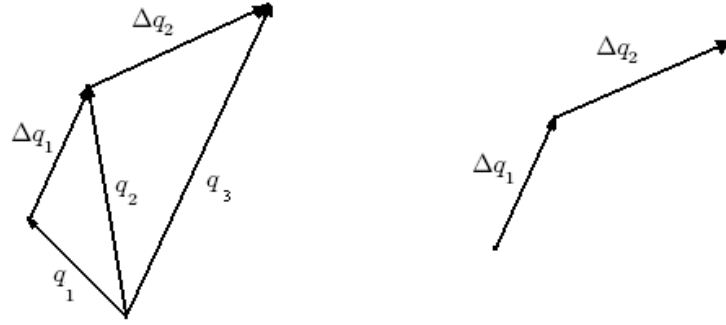
Figure 2.8: The geometrical interpretation of the computation Δq.

Via a QR-factorization, an orthogonal basis is extracted. The QR-factorization, computed by the 'modified Gram-Schmidt' procedure:

$$[\Delta q^n, \Delta q^{n-1}, \ldots, \Delta q^{n-L+1}] = DT, \tag{2.27}$$

with $T \in \mathbb{R}^{L \times L}$ upper triangular and $D \in \mathbb{R}^{N \times L}$ orthogonal, where L is the number of Krylov vectors Δq used. A Krylov acceptance ratio (or Krylov acceptance criterion) k_a is introduced as a criterion for adding vectors to the basis. If $|t_{j,j}| \geq k_a |t_{j+1,j+1}| \, j = 1, \ldots, L-1$, the dominant eigenspace is j-dimensional and we add the first j columns of $D = [D_1 \ldots D_j]$ to the basis Z. The method checks the k_a-criteria at a user-specified rate. According to this criterion the method decides itself how many vectors must be added to the basis.

For linear problems, it can be shown[70] that the obtained basis (in exact arithmetics) is equivalent to the basis obtained from an Arnoldi decomposition based on the normalized residuals $[\Delta q] = \{\Delta q^n, \Delta q^{n-1}, \ldots, \Delta q^{n-L+1}\}$. In this way k_a can also be interpreted as a criterion to estimate whether the matrix $[\Delta q]$ is rank-deficient or not.

For an orthonormal basis $V \in \mathbb{R}^{N \times k}$ the Arnoldi decomposition reads

$$QJQV = VG + fe_m^T, \quad V \in \mathbb{R}^{N \times k}, \quad G \in \mathbb{R}^{k \times k}, \quad f \in \mathbb{R}^{N \times 1}, \tag{2.28}$$

where $f = g_{k+1}v_{k+1}$ is residual vector orthogonal to the basis V and e_k is the unit vector along the k-th direction.

Combining the QR-factorization $V = D_j T_j$ with (2.28), the Arnoldi decomposition associated with $[\Delta q]$ is obtained:

$$QJQD_j - D_j H = f e_j^T T_j^{-1} = r_j e_j^T, \quad ||r_j||_2 = h_{j+1,j}$$

where $H = T_j G T_j^{-1}$ is the Hessenberg matrix. The subdiagonal elements of H are related the the diagonal elements of T_j as:

$$h_{i+1,i} = e_{i+1}^T T_j G T_j^{-1} e_i = \frac{t_{i+1,i+1}}{t_{i,i}}, \quad i = 1, \dots, j-1.$$

The accuracy of the approximate eigenvectors, can be computed by solving the eigenvalue problem $Hx = x\theta$, with $y = D_j x$ and $||y||_2 = 1$:

$$||(QJQ - \theta I)x||_2 = ||r_j e_j^T y||_2 = ||r_j||_2 |e_j^T y| \leq \frac{t_{j+1,j+1}}{t_{j,j}},$$

which shows that the residual of the computed eigenspace for QJQ is bounded by the inverse of Krylov ratio k_a.

Note that the value of k_a is problem-dependent; for example, in Ref. [35] different values of k_a are presented. Numerical experiments for the estimation of k_a are presented in figure 2.9.
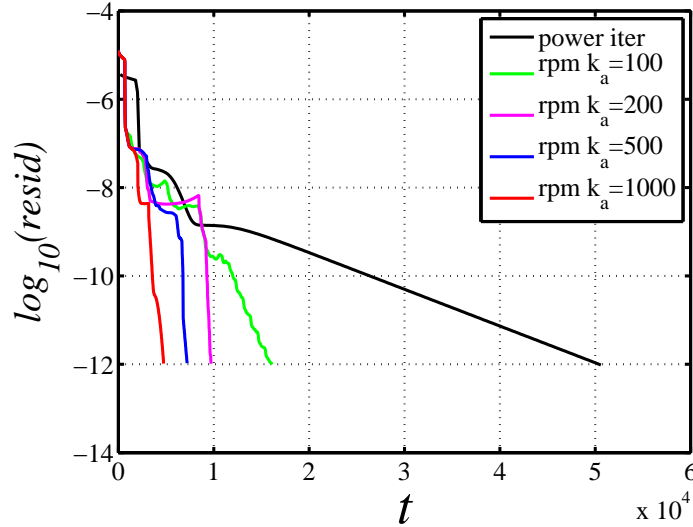
Figure 2.9: The convergence rate ($Re = 1000$, $S = 0.7896962337$, stable branch) for different Krylov acceptance ration $k_a =$: red curve $k_a = 1000$, blue $k_a = 500$, magenta $k_a = 200$, green $k_a = 100$ and black curve DNS.

Using the basis Z we can then produce a projection of the Jacobian onto the space $\mathbb{P}$. The eigenvalues of the $m \times m$ matrix $H = Z^T JZ$ (the projected Jacobian) correspond to

the eigenvalues of J with the largest absolute values. The eigenvalues and corresponding eigenvectors of this matrix H can be found at relatively low cost.

During the course of the iteration, the extracted basis can become unnecessarily large, for instance when some eigenvalues have re-entered to the unit disk. In such a case too many vectors have been added to the basis due to an excessively small k_a-value. It is then essential to rearrange the basis, leaving only the eigenvectors, corresponding to eigenvalues outside the unit disk or very close to its boundary.

In the actual computations, we introduce coordinate variable z for the representation $p \in \mathbb{P}$ in the basis Z:

$$z \equiv Z^T p = Z^T u, \quad z \in \mathbb{R}^m,$$

so $p = Zz$ and $u = Zz + q$.

The iteration (2.25) in the subspace $\mathbb{P}$ can be written in these variables:

$$z^{n+1} = z^n + \left(I - Z^T J(u^n) Z\right)^{-1} \left(Z^T F(u^n) - z^n\right).$$

The numerical algorithm RPM, implemented in the current numerical simulations, can be summarized below:

The numerical algorithm RPM:

input the predicted (u^0);
$n \leftarrow 0$; $u \leftarrow F(u^0)$;
build the Krylov vectors $[\Delta q] = \{F(u^{L+1}) - F(u^L), \ldots, F(u^2) - F(u)\}$;
$q \leftarrow F(u^{L+1})$; $\hat{F} \leftarrow F(u^{L+2})$;
factorization $[\Delta q] = DT$;
k_a**- criterion: find** j**; projection basis:** $Z \leftarrow [D_1, \ldots D_j]$;
evaluate (JZ); $H \leftarrow Z^T JZ$;
while $(||(u - \hat{F})||_2 > tol)$

      $q_{old} \leftarrow q$;
      projection: $z \leftarrow Z^T z$; $q \leftarrow u - Zz$;
      numerical stabilization iteration:
            $z \leftarrow z + (I - H)^{-1}(Z^T \hat{F} - z)$;
            $q \leftarrow \hat{F} - ZZ^T \hat{F}$;
      $u \leftarrow Zz + q$; $\hat{F} \leftarrow F(u)$;
      $\Delta q^n = q - q_{old}$;
      $n \leftarrow n + 1$;
      if: $(n > n_{max})$
           update basis:
               factorization$[\Delta q^{n_{max}}, \ldots, \Delta q^{n_{max}-L+1}] = DT$;
               k_a**- criterion: find** j; $Z \leftarrow \{Z, D_1, \ldots D_j\}$; $Z \leftarrow orth(Z)$;
           improve basis accuracy:
               evaluate (JZ); $H \leftarrow Z^T JZ$;
               calculate eigenvalues and eigenvectors: $[v, e] \leftarrow eigen(H)$;
               select eigenvectors, for which eigenvalue lie outside K_δ: $V \leftarrow v$;
               $Z \leftarrow orth(ZV)$;
           evaluate (JZ); $H \leftarrow Z^T JZ$;
           $n \leftarrow 0$
      end if
end while.

2.3.3 Pseudo-arclength RPM continuation [97, 50]

Procedure

We describe now the continuation procedure adopted to follow steady state solutions as an external parameter λ is varied, regardless of their linear stability. The method is based on an adaptation of the RPM algorithm described above. In principle, once a solution $u(\lambda)$ is known for a given value of λ, it can be used as an initial guess for the next solution $u(\lambda + \Delta\lambda)$, and convergence of the scheme defined by Eq. (2.25) is expected for $\Delta\lambda$ small enough. This assumes that the Jacobian operator $(I - PJP)^{-1}$ is nonsingular in a neighborhood of the solution $u_s(\lambda)$. However, for some values of λ, the solution $u(\lambda)$ becomes unstable and can bifurcates back at a saddle node bifurcation, see for instance figure 2.10. These values of λ are associated with folds and saddle-node bifurcations. In the neighbourhood of such a parameter λ, there exists a value $\lambda = \lambda_c$ for which $[I - PJ(u(\lambda_c), \lambda_c)P]^{-1}$ is singular. Near $\lambda = \lambda_c$ the system (2.25) can become seriously ill-conditioned. This singularity makes the continuation impossible whereas these are precisely the parameter values we are interested in.
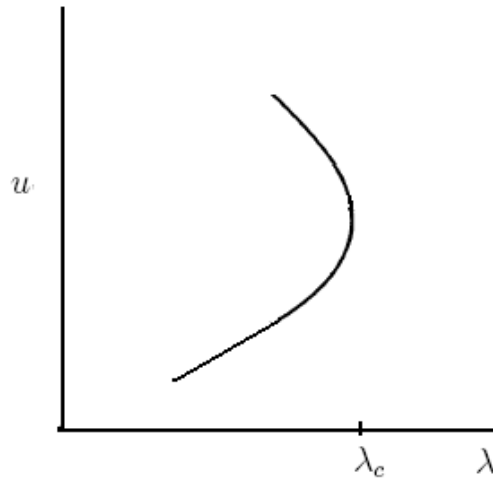
Figure 2.10: A schematic bifurcation of a solution.

In order to overcome this limitation, the pseudo-arclength continuation method was used[51], coupled to the RPM algorithm. This section describes the numerical procedure.

In order to perform the continuation, the phase-space corresponding to the solution vector p is enlarged by adding one dimension corresponding to the real parameter λ. A new real parameter s is introduced in order to parameterize the continuation path $\Gamma(s)$ in the enlarged phase-space (p, λ). s represents an arclength variable along Γ and will be increased monotically during the continuation using a *imposed* step Δs. The iterative solver is required to find the next point $(p + \Delta p, \lambda + \Delta\lambda)$ on Γ at the given pseudo-arclength

$s + \Delta s$, with $\Delta s^2 = (\Delta p, \Delta p) + (\Delta \lambda)^2$, which requires appending an additional constraint (the pseudo-arclength constraint) to the system (2.25). We thus enforce the additional scalar relation $N(p, \lambda, s) = 0$, where $N(p, \lambda, s) = \dot{p}^T \Delta p + \dot{\lambda} \Delta \lambda - \Delta s$. Here $(\dot{p}, \dot{\lambda})$ represents the tangent vector along the solution path $\Gamma(s)$, which can be approximated at first order using $\dot{p} = \Delta p / \Delta s$ and $\dot{\lambda} = \Delta \lambda / \Delta s$. As for the derivation of Eq. (2.25), the next point $(p + \Delta p, \lambda + \Delta \lambda)$ is a simultaneous zero of both $I - PF$ and N; it is found by using a first-order Taylor interpolation around (p, λ), shooting along the tangent vector $(\dot{p}, \dot{\lambda})$ with a step $(\Delta p, \Delta \lambda)$.

The full Newton-Raphson iteration for the pseudo-arclength continuation thus reads:

$$\begin{pmatrix} I - PJP & -F_\lambda \\ N_p & N_\lambda \end{pmatrix} \begin{pmatrix} \Delta p \\ \Delta \lambda \end{pmatrix} = \begin{pmatrix} PF(u, \lambda) - p \\ -N(p, \lambda, s) \end{pmatrix}, \tag{2.29}$$

where $F_\lambda \equiv (PF(u, \lambda))_\lambda$ and $N_p = (N(p, \lambda, s)_p$.

Geometrical interpretation

Geometrically, the relation $N(p, \lambda, s) = 0$ can be interpreted as a multi-dimensional right-angled triangle, where Δp and $\Delta \lambda$ are the short sides and Δs is the hypotenuse, whose length is held fixed. The lengths of Δp and $\Delta \lambda$ can vary under the constraint of constant Δs. Schematically, figure 2.11 (left) corresponds to a case of a large step in the parameter λ leading to a small change in the solution p. Figure 2.11 (right) represents the case when a small change in parameter λ causes a significant change in the solution p.
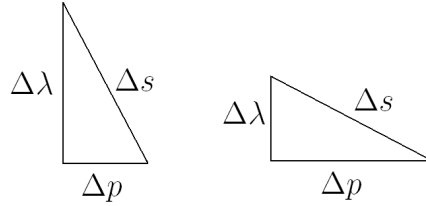
Figure 2.11: Geometric interpretation of the pseudo-arclength normalization.

In the continuation process, the decomposed system (2.24) with a new scalar constraint results in the following re-ordered system:

$$\begin{aligned} q &= QF(u, \lambda), \\ p &= PF(u, \lambda), \\ u &= p + q \\ N(p, \lambda, s) &= 0. \end{aligned} \tag{2.30}$$

Since the restriction of $[I - J(u(\lambda), \lambda)]^{-1}$ on the subspace $\mathbb{P}$ is potentially singular while the restriction onto $\mathbb{Q}$ is not, Shroff and Keller [97] performed the pseudo-arclength continuation only within the small dimensional subspace $\mathbb{P}$. This justifies why the pseudo-arclength

normalization $N(p, \lambda, s) = 0$ is independent of q. The solution branch is parameterized by s as $\Gamma(s):\{u(s), \lambda(s)\}$ with $u(s) = p(s) + q(s)$ and $\lambda(s)$ satisfying (2.30).
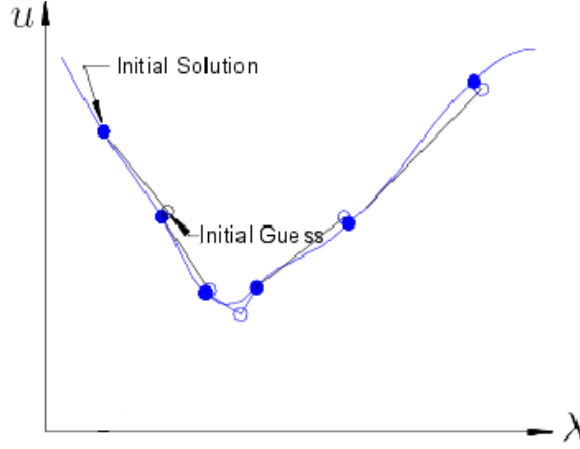
Figure 2.12: Schematic pseudo-arclength continuation in the enlarged $(\mathbf{u}, \lambda)$ space using predictor-solver procedure.

The implemented pseudo-arclength RPM uses an iterative predictor-solver scheme: given two points on Γ: (u^{n-1}, λ^{n-1}) and (u^n, λ^n) we predict the new solution using simple linear extrapolation:

$$\begin{aligned} \lambda^{n+1} &= 2\lambda^n - \lambda^{n-1}, \\ u^{n+1} &= 2u^n - u^{n-1}, \end{aligned} \tag{2.31}$$

for a fixed Δs, for example, see figure 2.12, where the initial solution guess is shown by black circle. Than we correct this predicted solution by Newton method and obtain the final solution (corresponding blue circle). The solver step uses the Newton-Raphson method for the variables p and λ, see (2.29), and a fixed point iteration for q with a first-order correction term $[QF(u^n, \lambda^n)]_\lambda \Delta \lambda^n$. This correction term is introduced since λ changes during the iteration. The resulting iteration is:

$$q^{n+1} = QF(u^n, \lambda^n) - [QF(u^n, \lambda^n)]_\lambda \Delta \lambda^n$$

$$\begin{pmatrix} I - PJ^n P & -F_\lambda^n \\ N_p & N_\lambda \end{pmatrix} \begin{pmatrix} \Delta p^n \\ \Delta \lambda^n \end{pmatrix} = \begin{pmatrix} PF(u^n, \lambda^n) - p^n \\ -N(p^n, \lambda^n, s) \end{pmatrix}, \tag{2.32}$$

where $\Delta p = p^{n+1} - p^n$, $\Delta \lambda = \lambda^{n+1} - \lambda^n$.

Using expression (2.32), the iteration scheme can be written as:

$$q^{n+1} = QF(u^n, \lambda^n) - [QF(u^n, \lambda^n)]_\lambda \Delta \lambda^n$$

$$\begin{pmatrix} p^{n+1} \\ \lambda^{n+1} \end{pmatrix} = \begin{pmatrix} p^n \\ \lambda^n \end{pmatrix} - [M^n]^{-1} \begin{pmatrix} p^n - PF(u^n, \lambda^n) \\ N(p^n, \lambda^n, s) \end{pmatrix}, \tag{2.33}$$

where

$$M^n = \begin{pmatrix} I - PJ(u^n)P & -F_\lambda \\ \dot{p}^T & \dot{\lambda} \end{pmatrix}. \tag{2.34}$$

Shroff and Keller [97] demonstrated that M can be nonsingular when $I - PJP$ is singular, enabling the pseudo-arclength procedure to continue past (singular) fold points.

In the actual computations, we introduce coordinate variable z for the representation $p \in \mathbb{P}$ in the basis Z:

$$z \equiv Z^T p = Z^T u, \quad z \in \mathbb{R}^m,$$

so $p = Zz$ and $u = Zz + q$.

The iteration (2.33) in the subspace $\mathbb{P}$ can be written in these variables:

$$q^{n+1} = QF(u^n, \lambda^n) - [QF(u^n, \lambda^n)]_\lambda \Delta \lambda^n$$
$$\begin{pmatrix} z^{n+1} \\ \lambda^{n+1} \end{pmatrix} = \begin{pmatrix} z^n \\ \lambda^n \end{pmatrix} - [M^n]^{-1} \begin{pmatrix} z^n - Z^T F(u^n, \lambda^n) \\ N(z^n, \lambda^n, s) \end{pmatrix}, \tag{2.35}$$

where

$$M^n = \begin{pmatrix} I - ZJ(u^n)Z & -Z^T F_\lambda \\ \dot{z}^T & \dot{\lambda} \end{pmatrix} \tag{2.36}$$

and $N(z^n, \lambda^n, s) = \dot{z}^T \Delta z + \dot{\lambda} \Delta \lambda - \Delta s$.

Update of the dominant eigenspace

As the continuation along $\Gamma(s)$ progresses, the dominant eigenspace of J might change, rendering our estimate of the basis Z inaccurate. We decide to update the columns of Z by performing one step of an orthogonal power iteration after each continuation step:

$$Z \leftarrow \mathrm{orth}(JZ),$$

i.e., we orthogonalize the columns of JZ using a Gram-Schmidt orthogonalization procedure. This step requires minimal work: in particular, no additional function evaluation is needed. Shroff[97] states that one power iteration per continuation step is sufficient to maintain Z up to a reasonable accuracy level.

Note that the extracted basis can sometimes become unnecessarily large, which can considerably slow down the convergence. This can happen for the following various reasons:

- the eigenvalues have reapproached the disk $|\lambda| < K_\delta$ ($K_\delta < 1 - \delta$)

- too many vectors have been added to the basis due to a low k_a-value

In both cases unnecessary directions should better be deflated from the basis. We therefore decrease the size of Z by considering the $m \times m$ matrix $H = Z^T J Z$. The eigenvalues of H form a subset of those of J; we would like them to consist only of those outside the disk K_δ. After each continuation step we compute the eigenvalues and eigenvectors of H, which is not expensive since m is a small number. In case there are $\hat{m}$ eigenvalues of H lying outside K_δ ($\hat{m} < m$), we select the $\hat{m}$ corresponding eigenvectors and form the real basis $V \in \mathbb{R}^{m \times \hat{m}}$. The columns of ZV are then a good approximation of the desired basis. Thus we can perform the substitution:

$$Z \leftarrow \operatorname{orth}(ZV).$$

The numerical algorithm RPM for pseudo-arclength continuation can be summarized as follows:

---

input previous solutions and basis $(u^{-1}, \lambda^{-1}, u^0, \lambda^0, Z^0)$;
do $i = 0...i_{max}$

    use extrapolation (2.31): u, λ;

     $\hat{F} \leftarrow F(u, \lambda)$; $Z \leftarrow Z^0$;

    improve basis accuracy:

        evaluate (JZ); $H \leftarrow Z^T JZ$; $[v, e] \leftarrow eigen(H)$;

        select eigenvectors, for which eigenvalue lie outside K_δ: $V \leftarrow v$;

        $Z \leftarrow orth(ZV)$;

    $z_0 \leftarrow Z^T u_0$; $z \leftarrow Z^T u$; **calculate** $N(z, \lambda, \Delta s)$, $resid = ||(u - \hat{F})||_2 + ||N||_2$;

    calculate M **form (2.36)**; $n \leftarrow 0$

    while $(resid > tol)$

        $q_{old} \leftarrow q$;

        numerical stabilization iteration (2.35): q, z, λ; $u \leftarrow Zz + q$;

        $\hat{F} \leftarrow F(u, \lambda)$; $N \leftarrow N(z, \lambda, \Delta s)$; $resid = ||(u - \hat{F})||_2 + ||N||_2$;

        $\Delta q^n = q - q_{old}$; $n \leftarrow n + 1$;

        if: $(n > n_{max})$

            update basis:

                $[\Delta q^{n_{max}}, \ldots, \Delta q^{n_{max}-L+1}] = DT$;

                k_a**- criterion: find** j; $Z \leftarrow \{Z, D_1, \ldots D_j\}$; $Z \leftarrow orth(Z)$;

            improve basis accuracy:

                evaluate (JZ); $H \leftarrow Z^T JZ$; $[v, e] \leftarrow eigen(H)$;

                select eigenvectors: $V \leftarrow v$;

                $Z \leftarrow orth(ZV)$;

            $z_0 \leftarrow Z^T u_0$; $z \leftarrow Z^T u$;

            calculate $N(z, \lambda, \Delta s)$, $resid = ||(u - \hat{F})||_2 + ||N||_2$;

            calculate M **form (2.36)**; $n \leftarrow 0$;

        end if

    end while

    $Z^0 \leftarrow orth(JZ)$; $u^{-1} \leftarrow u^0$; $u^0 \leftarrow u$; $\lambda^{-1} \leftarrow \lambda^0$; $\lambda^0 \leftarrow \lambda$;
end do.

2.4 Validation

The present numerical investigations are carried out for the computational domain with dimensions $R = 10$ and $x_0 = 20$, which has been shown to be sufficiently large to avoid any deformation of the vortex breakdown by the downstream and lateral boundaries (Ruith et al.[78]). The numerical resolution of reference is ($N_R = 127$, $N_x = 257$) with the corresponding timestep $\Delta t = 0.01$. Both the minimal spatial and the temporal resolutions used in the present study are nearly twice that used by Ruith et al.[79] ($N_R = 61$, $N_x = 193$, $\Delta t = 0.025$) and about four times those used by Grabowski & Berger[37] ($N_R = 61$, $N_x = 31$, $\Delta t = 0.11$). The spatial numerical scheme for solving Poisson equation is the fourth order, which permit to have the fourth order accuracy of the code.

2.4.1 Steady states

A swirling jet is chosen as a representative test case with the governing parameters $Re = 200$ and $S = 1.095$. This choice is identical to the reference case considered by Grabowski & Berger[37] and by Ruith et al.[78]. The streamfunction was computed for a comparison with Ruith et al.[79]. Figure 2.13 shows streamline patterns obtained from the current numerical simulations (frame a) and from Ruith et al. (frame b).
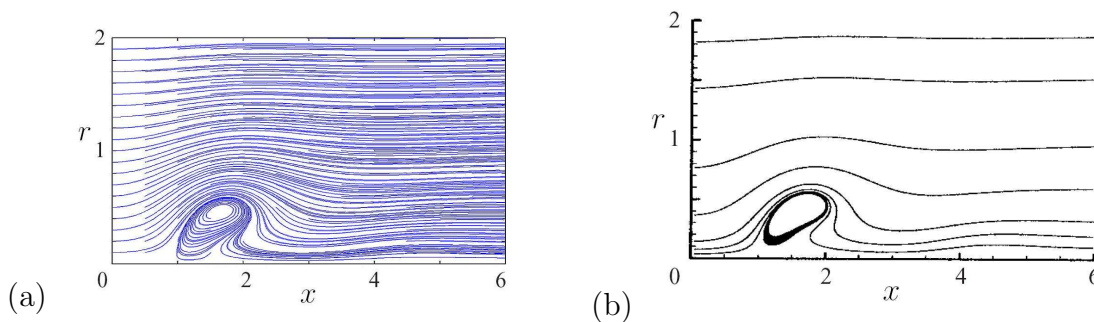
Figure 2.13: Reference case: $Re = 200$, $S = 1.095$. Projected streamlines in the half plane for the axisymmetric steady state (a) compared with the streamlines obtained by of Ruith et al. (b) (adapted from figure 3 (a) of Ref.[79]).

We also show a comparison of the profiles for all velocity components with the results from Ruith et al.[79], see Figure 2.14. The velocity components are shown here at various radial positions $r = 0$ (solid line), $r = 1$ (dashed line) and $r = 8$ (dash-dotted line). The first column corresponds to the original results of Ruith et al.[78], the second column to the velocity calculated by current DNS. From the comparison of the figures we found a negligible difference in axial and radial velocity components and small difference in the azimuthal velocity (around the point $x = 2$), where we observe in our case that the local minimum is lower than in the case of Ruith et al.[78]. Still we can conclude that the results
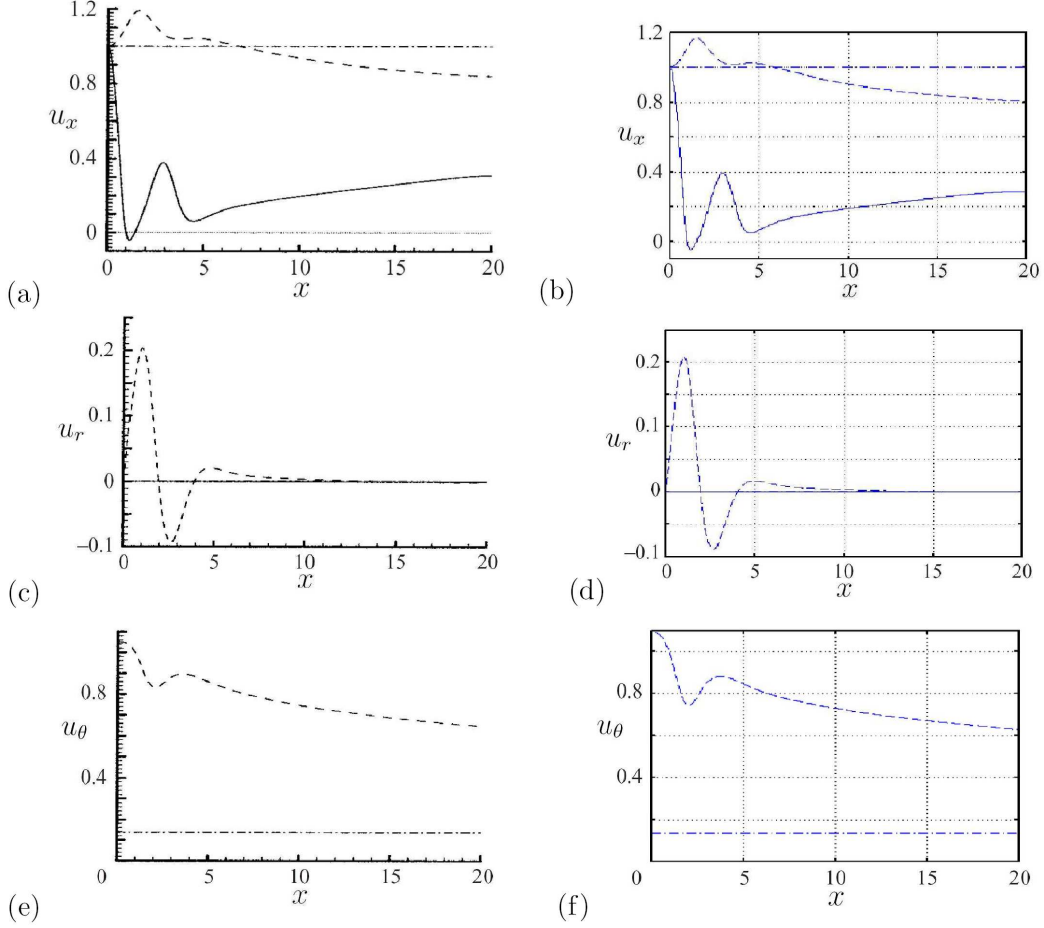
Figure 2.14: Reference case: axial (a) and (b), radial (c) and (d) and azimuthal (e) and (f) velocity components at different radial positions (solid line: $r = 0$, dashed line: $r = 1$, dash-dotted line: $r = 8$) as a function of the axial position. Left column: graphics adapted from figure 7 of Ref.[79]; right column: present numerical simulations.

of our DNS match quite close the results of Ruith et al.[79].

2.4.2 Temporal Dynamics

In order to validate the temporal dynamics, we compare again our numerical simulations to the results of Ruith et al.[79]. Figure 2.15 displays the time evolution of the azimuthal vorticity ω_θ. We superimpose the normalized vorticity contours of Ruith et al.[79] (black lines) on our results (colored lines). In both cases, the azimuthal vorticity ω_θ is normalized using the maximum positive and minimum negative levels for both the positive and negative contours, respectively. The increment in ω_θ is $\Delta\omega_\theta = 0.1$.

In both numerical simulations the initial condition at $t = 0$ corresponds to the columnar
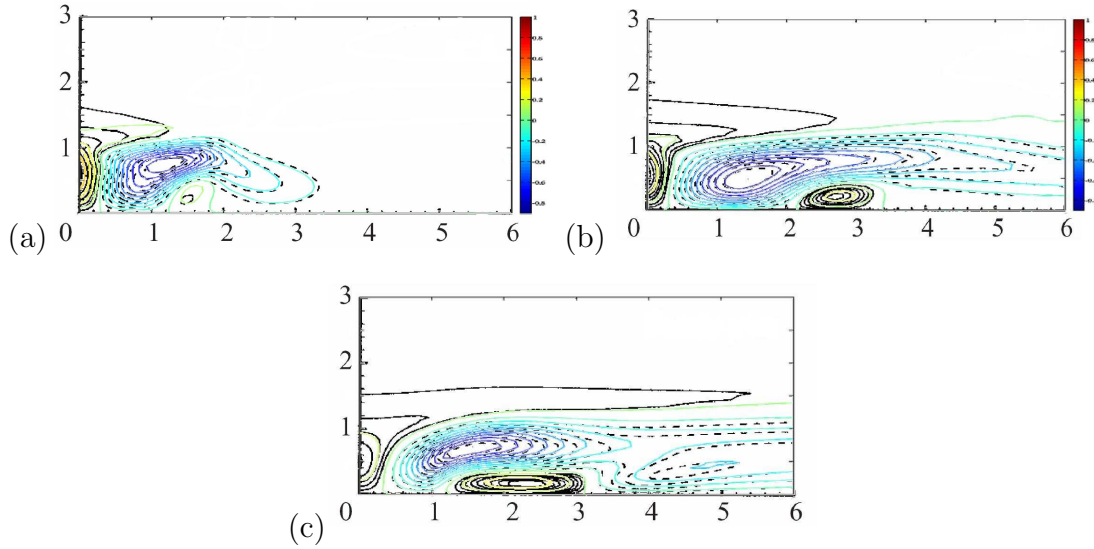
Figure 2.15: Reference case: temporal evolution of azimuthal vorticity ω_θ: (a) $t = 2$, (b) $t = 5$ and (c) steady state. Black dashed and solid contours correspond to negative and positive vorticity, respectively, calculated by Ruith et al. (frame (a) figure 5, Ref. [79]), colored contours with corresponding colorbar on the right correspond to our simulations.

vortex, not shown here. Negative azimuthal vorticity ω_θ becomes visible already at $t = 2$, see frame (a), figure 2.15.

The agreement between the present calculations and those by Ruith et al.[79] is here excellent. Minor differences can be detected in the vorticity contours, see figure 2.15, though their order of magnitude is comparable to the accuracy of the graphic contour interpolation.

Note that the spatial scheme used here is of better order than in Ruith et al. (4th compared to 2nd), and that the resolution is finer ($N_R = 127$, $N_x = 257$ compared to $N_R = 61$, $N_x = 193$). The temporal scheme used here is also of order 4, with a smaller timestep ($\Delta t = 0.01$) than Ruith et al. ($\Delta t = 0.025$, order not specified).

2.4.3   Influence of the Reynolds number Re

Since the present numerical investigations were carried out for various values of the Reynolds numbers Re, we need to compare our computations to those by Ruith et al.[79] for several values of Re as well. Here the parameter $S = 1.095$ is kept constant, while Re is varied from $Re = 100$ to $Re = 500$.

Figure 2.16 displays a comparison of the streamline patterns for three different values of Re: 100, 300 and 500. The results closely match each other for $Re = 100$, see frames (a) and (b) in figure 2.16. For $Re = 300$, we note a little discrepancy in the streamline patterns: both recirculation bubbles are similar, however the wake behind the recirculation bubble (frame (d)) is slightly downstream of that computed in [79] (frame (c)). Increasing Re up
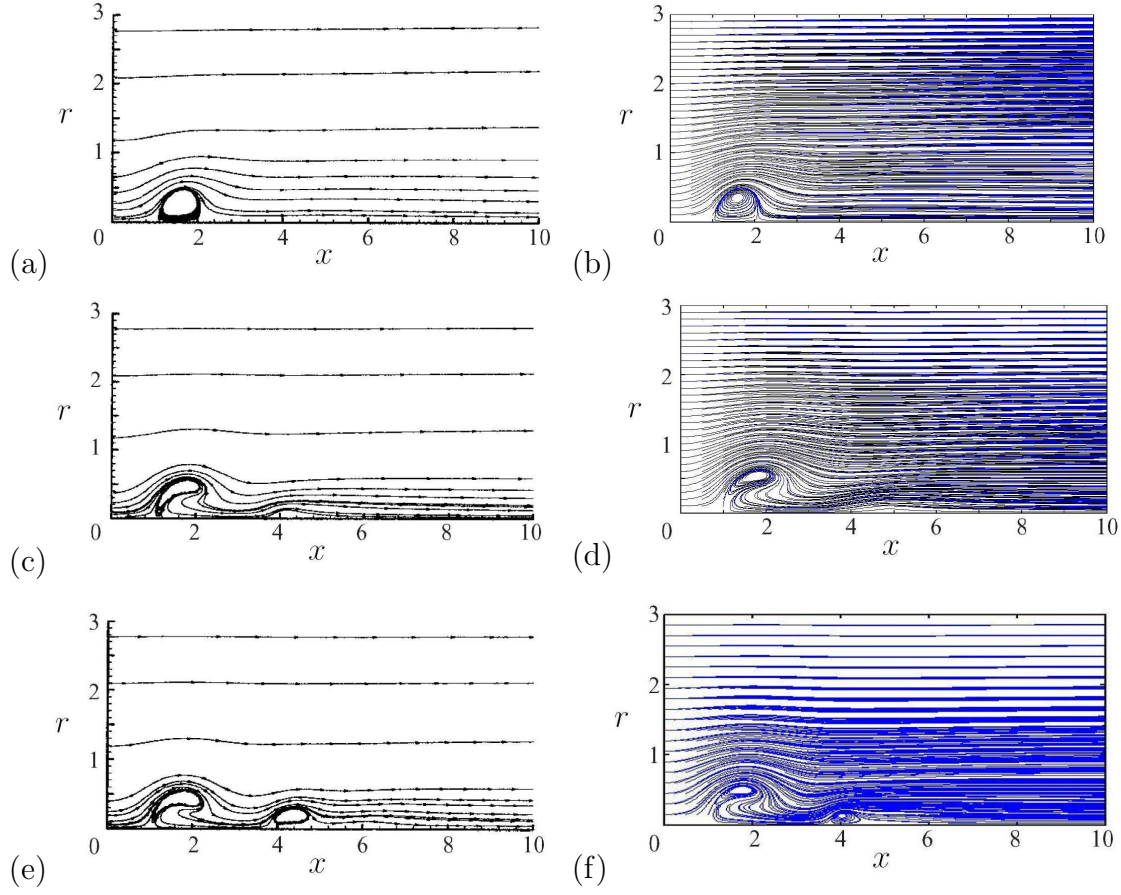
Figure 2.16: Streamline patterns for $S = 1.095$ with varying Re. Left column: graphics adapted from figure 18 of Ruith *et al.* [79]; right column: present numerical simulations. $Re = 100$: (a)-(b), $Re = 300$: (c)-(d), $Re = 500$: (e)-(f).

to 500, the match for the streamlines patterns becomes qualitative only. The recirculation bubbles have slightly different shapes; e.g. in our case the second bubble downstream is located closer to the first one.

In order to ensure that the spatial resolution we used in the comparison above is sufficient, we have increased the number of grid points by a factor of either two ($N_R = 253$, $N_x = 513$), three ($N_R = 379$, $N_x = 769$) and four ($N_R = 505$ and $N_x = 1025$) times in both axial and radial directions. We have focused on the most difficult case to resolve numerically, namely $Re = 500$. We use the following notations for the four different resolutions:

- N_1: ($N_R = 127$, $N_x = 257$) ('coarse')

- N_2: ($N_R = 253$, $N_x = 513$) ('double')

- N_3: ($N_R = 379$, $N_x = 769$) ('triple')
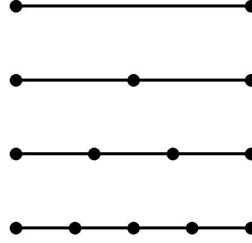
Figure 2.17: Schematic location of grid points for various meshes used in the code validation. From top to bottom : coarse grid, double, triple and quadruple resolution. The nth refined mesh ($n = 2, 3, 4$) is designed so that every n^{th} grid point coincides exactly with a grid point of the coarse mesh.

- N_4: ($N_R = 505$, $N_x = 1025$) ('quadruple', the 'finest' resolution assumed close to the exact solution)

In all cases, in order to facilitate pointwise comparison, special care was taken to ensure that all grid points of the coarse mesh N_1 coincide with some of the grid points of the refined mesh N_i (i=2,3,4), see figure 2.17. In the following, we refer to the solution obtained with quadruple resolution N_4 as to the *finest* reference solution, which is close to the exact solution. We compare this finest solution with other solutions computed using coarser grids, at spatial locations corresponding to the coarse grid N_1.

All results are displayed in figure 2.18. Figure 2.18 (a) displays the magnitude of the velocity $|\vec{u}_{N_4}| = \sqrt{(u_x^2 + u_r^2 + u_\theta^2)}$ for the finest solution N_4 and its maximum is 1.3, i.e. of $O(1.5)$.Figure 2.18 (b),(c),(d) are spatial maps of the error field $|\delta\vec{u}_n(x, r)|$ for resolutions $n = N_1$, N_2 or N_3 compared to the solution computed with resolution N_4, where for any given location (x, r), $\delta\vec{u}_n(x, r) = \vec{u}_n(x, r) - \vec{u}_{N_4}(x, r)$. In all cases the numerical discrepancies appear to be localized behind the recirculation bubble. Quantitatively, the maximum error is of the order of 51%, 14.6% and 4.12% for the resolutions N_1, N_2 and N_3, respectively. The coarsest N_1 and double N_2 resolutions can thus be considered as too low whereas the resolution N_3 is satisfying. This means that the recirculation bubble is very sensitive to the used grid point distance and its spatial structure for the case of the governing parameters $Re = 500$ and $S = 1.095$ can be well described only at very fine grids such as N_3 and N_4.

Figure 2.18(e) shows the error computed on the grid N_1, as a function of the resolution, using the $L^\infty-$ (blue line) and the L^2- (red line) norms. The L^∞-norm refers to the maximum of the error field $|\delta\vec{u}_n(x, r)|$ over all grid points: $||\delta\vec{u}||_\infty = \max_{x_i, r_j} |\delta\vec{u}(x_i, r_j)|$. The L^2-
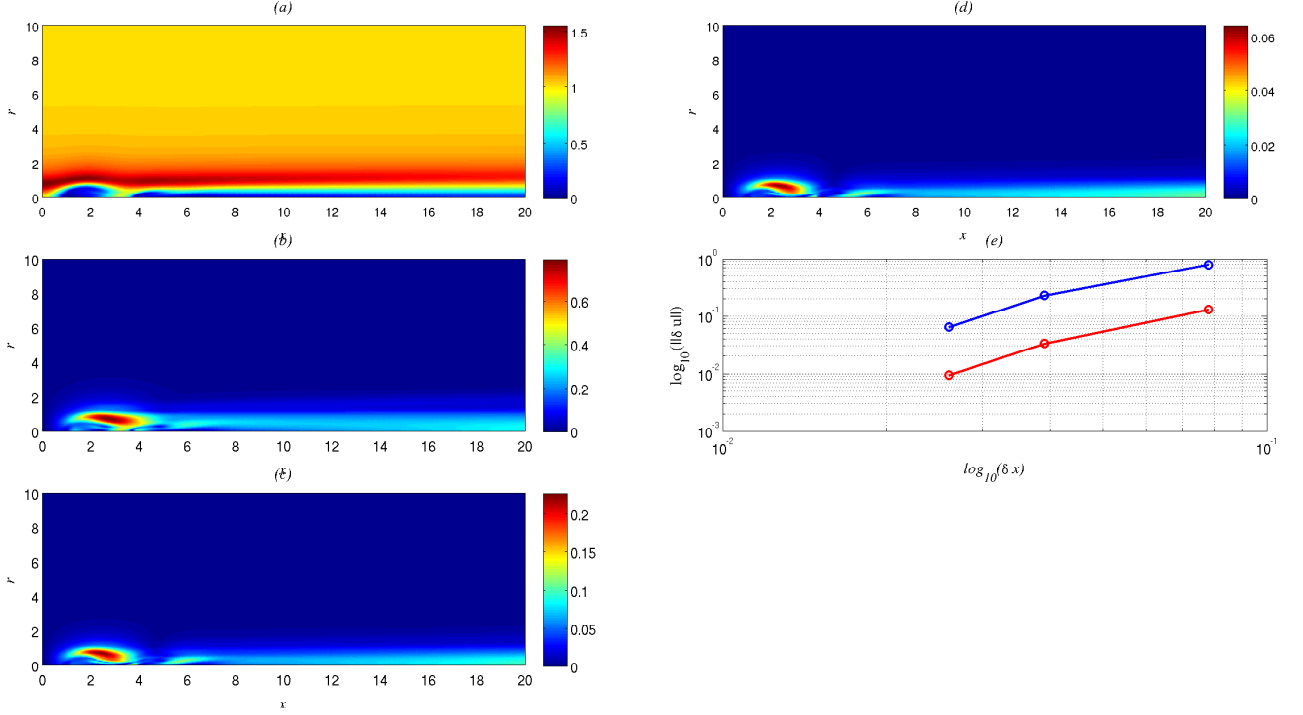
Figure 2.18: Resolution test for $S = 1.095$, $Re = 500$. Magnitude of the velocity of the finest solution using grid resolution N_4 (a). Field error for lower resolutions $|\delta\vec{u}_n(x,r)| = |\vec{u}_n(x,r) - \vec{u}_{N_4}(x,r)|$: $n = N_1$ (b), N_2 (c) and N_3 (d). $L^\infty-$ (blue) and L^2- (red) norms of the error field for various resolutions with step δx.

norm is the Euclidian norm over the whole grid mesh: $||\delta\vec{u}||_2 = \sqrt{\dfrac{1}{N_R N_x} \displaystyle\sum_{i=1}^{N_x} \sum_{j=1}^{N_R} |\delta\vec{u}(x_i, r_j)|^2}$.

Not that it is *not* the energy norm of the error field since it does not take into account the r factor for the cylindrical integration, nor any weight factors due to the non uniformity in r of the grid. The slopes interpolated from figure 2.18(e) for the resolutions N_2 and N_3 are both close to 3, which suggests third order for the spatial scheme. Note that the expected fourth order for the method requires in principle asymptotically small grid spacing. There is a trend towards increasing order visible in figure 2.18(e), suggesting that 4th order can only be reached by prohibitively expensive grid resolutions.

This whole study leads to the conclusion that the triple resolution N_3 ($N_R = 379$, $N_x = 769$) is sufficient for the case at hand. Moreover, further increases in resolution have shown that the corresponding solution is numerically robust. Importantly, this comparison also shows that the number of grid points used by Ruith et al.[79] is not sufficient to properly resolve the spatial structure of the vortex breakdown for $Re = 500$ and $S = 1.095$. This justifies the poor quantitative agreement obtained in figure 2.16.

3   Viscous Effect

This chapter discusses the effects of a finite viscosity on the the bifurcation diagram for axisymmetric swirling jets. The first part of the chapter corresponds to an article published in the journal Physics of Fluids in 2009. This part sheds light on the appearance of the bifurcation structure of the viscous solution, using asymptotic analysis and numerical simulation. The second part demonstrates the robustness of these results with respect to the numerical resolution.

3.1 The Bifurcation Structure of Viscous Steady Axisymmetric Vortex Breakdown with Open Lateral Boundaries

Elena Vyazmina,Joseph W. Nichols, Jean-Marc Chomaz, Peter J. Schmid

Abstract

The effect of small viscosity on the behavior of the incompressible axisymmetric flow with open lateral and outlet boundaries near the critical swirling number has been studied by numerical simulations and asymptotic analysis. This work extends the theoretical studies of Wang and Rusak and numerical results of Beran and Culick to the case of flow with open lateral and outlet boundaries. In the inviscid limit the columnar flow state constitutes a solution that is known to become unstable at a particular swirl parameter. An asymptotic expansion shows that for small perturbations about this inviscid state an exchange of stability gives rise to a double saddle node bifurcation. The solution of the Euler equations breaks into two branches of the Navier–Stokes equations with a gap between the branches in which no near-columnar flow can exist. Around this region, two steady state solutions exist for the same boundary conditions, one close to the columnar state, the other corresponding to either an accelerated or a decelerated state. This bifurcation structure is verified by numerical simulations, where the Navier–Stokes solutions are computed using branch continuation techniques based on the recursive projection method. For relatively small Reynolds numbers the numerically computed bifurcation curve does not exhibit any characteristic fold and thus no hysteresis behavior. In this case, only a single equilibrium solution is found to exist, which changes monotonically from the quasi-columnar state to the breakdown solution. For large Reynolds numbers, however, the numerically determined bifurcation diagram confirms the fold structure characterized by the disappearance of the nearly columnar state via a saddle node bifurcation. Using the minimum axial velocity on the axis as a measure of the flow state we show that the agreement between theory and numerics is asymptotically good.

3.1.1 Introduction

Vortex breakdown is a feature of many flows that have both axial and azimuthal velocity components; these flow fields are known as swirling flows. It is characterized by an abrupt and dramatic change in the structure of the axisymmetric core, which leads to the appearance of stagnation points on or near the axis of symmetry followed by regions of reversed

flow referred to as the vortex breakdown bubble.

The study of vortex breakdown is of great interest to, among other fields, aerodynamics and combustion physics. Breakdown also arises in a number of natural settings such as tornadoes, dust devils and water spouts. [39] Its occurrence in the flow over delta wings at high angles of attack can have a significant effect on lift, drag and pitching moment as reported by Hummel and Srinivasan. [47] For the design of combustion chambers, Beer and Chigier [6] and Faler and Leibovich [30] emphasized the importance of understanding the flow structure of vortex breakdown. In this configuration, breakdown is intentionally triggered to improve air-fuel mixing and thus produce a more stable and compact flame as well as a more complete combustion process.

Scientific interest in explaining this nonlinear phenomenon has produced a great body of experimental, numerical and theoretical studies. In addition, several review articles on vortex breakdown have appeared: see, for example, Refs. [41, 58, 60, 26, 24, 95, 4, 2, 87, 82]. According to these reviews various stability criteria have been developed and proposed over the years. Despite a great deal of progress, many details of the vortex breakdown process are still poorly understood, and the continued study of this phenomenon is essential both for fundamental reasons and for the development of different technological devices such as hydrocyclon separators, [48] combustion chambers, [26] nozzles and other applications where swirl plays an important role.

In an early study, Squire [101] and Benjamin [7] investigated inviscid, incompressible, axisymmetric, swirling flow in a pipe. They defined a critical level of swirl S_{cB} when infinitely long small-amplitude axisymmetric standing waves appear in the flow. Supercritical vortex flow with a swirl of $S < S_{cB}$ does not support such waves, whereas subcritical flow with $S > S_{cB}$ does.

Leibovich [57] revealed that the critical state is a singular point for the inviscid steady flow. Using weakly nonlinear asymptotic analysis he observed a branch of the steady-state Euler equations that bifurcates at the critical swirl from the columnar state and continues into the region $S < S_{cB}$. This branch describes a standing solitary wave arising from the base columnar state in an infinitely long pipe.

Keller et al.[52] considered inviscid axisymmetric vortex breakdown in an infinitely long pipe characterized by a semi-infinite stagnation region with free boundaries on the base columnar flow. This solution describes the transition from a base inlet columnar state to another columnar state further downstream that has the same dynamics due to the conservation of axial momentum along the pipe. For a fixed vortical core radius at the inlet, this solution only exists for a specific swirl S_0 with $S_0 < S_{cB}$.

In a sequence of papers, Rusak and collaborators[82, 111, 112, 113, 88, 114, 84, 90, 81, 83] comprehensively investigated the dynamics and stability behavior of an incompressible axisymmetric vortex flow in a finite-length circular pipe. Fixed profiles for axial flow, circu-
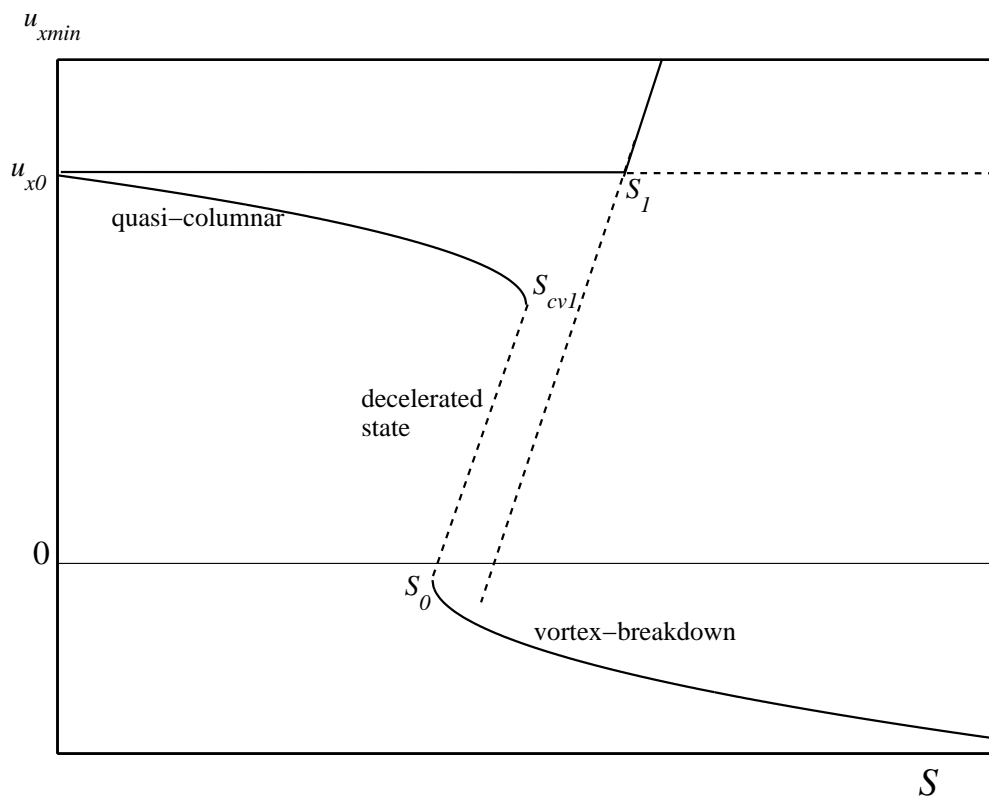
Figure 3.1: Qualitative bifurcation diagram for axisymmetric vortex breakdown for both inviscid and viscous flows. Here, u_{xmin} is the minimum axial velocity found at any point in the computational domain.

lation and azimuthal vorticity have been imposed at the inlet of the pipe, together with a zero-radial-velocity boundary conditions at the outlet. These conditions take into account the flow behavior observed in the experimental work of Bruecker and Althaus[16] who reported that the inlet flow did not change appreciably as vortex breakdown occurred. The same behavior has also been demonstrated in the numerical investigations of Beran, [11] Lopez [64] and Snyder and Spall. [99] Based on these conditions the theoretical work of Rusak and collaborators provides an encompassing picture of the physical mechanisms underlying axisymmetric vortex breakdown (see figure 3.1). The existence of three steady branches connected by two critical levels of swirl S_0 and S_1 ($S_0 < S_1$) has been shown, where the branch corresponding to the critical swirl S_1 represents an extension of Benjamin's [7] theory of vortex breakdown in an infinite pipe to the case of a finite-length pipe, while the branch associated with S_0 is an extension of Keller et al. [52] also to a finite-length pipe. As was reported by Wang and Rusak[113] the columnar state is absolutely stable for $S < S_0$, linearly stable for $S_0 < S < S_1$ and unstable for $S > S_1$. The solitary-wave branch connecting the states corresponding to the swirls S_0 and S_1 is unstable and describes axisymmetric travelling waves convecting downstream. The breakdown branch originating from the state with swirl S_0 is globally stable for any swirl $S > S_0$ (see figure 3.1).

The analysis of Wang and Rusak [113, 111, 112, 88] shows that the critical flow state at a swirl S_1 consists of a marginal equilibrium. Mathematically, it is well known that transcritical bifurcations, such as the one near swirl S_1, are structurally unstable, *i.e.*, any perturbation to the solution near the critical point can lead to significant changes in the bifurcation behavior and thus in the nature of the solution. [111, 112] When perturbed, the transcritical bifurcation at S_1 separates into two branches which no longer meet at S_1. For example, Lopez [64] found a fold indicating the existence of multiple solutions as well as hysteresis and limit point behavior, characteristic of a perturbed transcritical bifurcation.

At present, most theoretical and numerical investigations have primarily focused on swirling flow in pipes with corresponding boundary conditions. In this paper we generalized the analysis of swirling flows to the case with open lateral and outflow boundaries. This work furthermore extends the asymptotic analysis of Wang and Rusak [114] to this different set of lateral and outlet boundary conditions. While swirling flows in combustion chambers are confined, the geometry of these chambers is usually complex. Furthermore, vortex breakdown also occurs in applications where the flow is partially or fully unconfined such as the flow over delta wings or the geophysical flows mentioned above. Since both of these scenarios (complex confined geometry and unconfined geometry) have significantly different boundary conditions than those for flow in a pipe, we focus in the present paper on the influence of these boundary conditions on the vortex breakdown solutions obtained over the entire domain. This is accomplished by comparing results obtained with different boundary conditions using both an extended asymptotic analysis and direct numerical simulations.

The paper is organized as follows. Section II gives the equations governing viscous vor-

tex breakdown and provides a detailed description of the chosen boundary conditions. In section III the numerical simulations are presented. The critical swirl number is found in section IV. The asymptotic analysis of near critical swirling flow is provided in section V. Then, in section VI, the asymptotic and numerical solutions of the problem are compared and the relation between the present investigation and the breakdown of vortex flow in a pipe is discussed. Finally, our results are summarized in section VIII.

3.1.2   Mathematical Model

To model vortex breakdown, we consider an unsteady, axisymmetric, incompressible viscous flow of constant density ($\rho = 1$) in a cylindrical domain of outer radius R and axial length x_0. We use cylindrical coordinates where x, r and θ denote the axial, radial and azimuthal directions, respectively. Likewise, the components of velocity in the axial, radial and azimuthal directions are represented by u_x, u_r and u_θ, respectively, and p denotes the pressure. We note that the ordering of the velocity components used in this paper differs from the convention used in Ref. [114].

The flow is governed by the axisymmetric Navier–Stokes and continuity equations which, in nondimensional form, read

$$\frac{\partial u_x}{\partial t} + u_x\frac{\partial u_x}{\partial x} + u_r\frac{\partial u_x}{\partial r} + \frac{\partial p}{\partial x} - \frac{1}{Re}\left(\frac{\partial^2 u_x}{\partial x^2} + \frac{\partial^2 u_x}{\partial r^2} + \frac{1}{r}\frac{\partial u_x}{\partial r}\right) = 0,$$

$$\frac{\partial u_r}{\partial t} + u_x\frac{\partial u_r}{\partial x} + u_r\frac{\partial u_r}{\partial r} - \frac{u_\theta{}^2}{r} + \frac{\partial p}{\partial r} - \frac{1}{Re}\left(\frac{\partial^2 u_r}{\partial x^2} + \frac{\partial^2 u_r}{\partial r^2} + \frac{1}{r}\frac{\partial u_r}{\partial r} - \frac{u_r}{r^2}\right) = 0,$$

$$\frac{\partial u_\theta}{\partial t} + u_x\frac{\partial u_\theta}{\partial x} + u_r\frac{\partial u_\theta}{\partial r} + \frac{u_r u_\theta}{r} - \frac{1}{Re}\left(\frac{\partial^2 u_\theta}{\partial x^2} + \frac{\partial^2 u_\theta}{\partial r^2} + \frac{1}{r}\frac{\partial u_\theta}{\partial r} - \frac{u_\theta}{r^2}\right) = 0,$$

$$\frac{\partial u_x}{\partial x} + \frac{1}{r}\frac{\partial}{\partial r}\left(ru_r\right) = 0.$$

These equations have been nondimensionalized by a characteristic length equal to the radius of the vortex core, r_{core}, and a characteristic velocity taken as the inlet axial velocity, u_{x0}. This results in a Reynolds number defined as

$$Re = \frac{u_{x0} r_{core}}{\nu},$$

where ν is the kinematic viscosity of the fluid. We have stated the time-dependent governing equations since our numerical simulations solve these equations by timestepping and recursive projection until a steady state is reached, as described in a following section. The steady vortex breakdown states of interest then satisfy the above system of governing equations with the time-dependent terms equal to zero.

At the inlet, the nondimensional axial, radial and azimuthal velocity components are

prescribed as

$$u_x(0, r) = 1,$$
$$u_r(0, r) = 0,$$
$$u_\theta(0, r) = U_\theta(r')/u_{x0} = Su_{\theta 0}(r),$$

(3.1)

where U_θ is the dimensional azimuthal velocity profile in dimensional coordinates $r' = r \cdot r_{core}$. The nondimensional swirl parameter $S = U_\theta(r_{core})/u_{x0}$ represents the ratio of the azimuthal velocity at the edge of the core to the axial free-stream velocity. This definition of the swirl parameter enforces the normalization $u_{\theta 0}(1) = 1$ of the nondimensional azimuthal velocity profile at the inlet. The total velocity profile given by (3.1) is axisymmetric and will be held constant at the inlet of our domain. Among the velocity profiles in the category described by (3.1) are the Burgers vortex that was used by, *e.g.*, Beran and Culick [12] and the Grabowski profile introduced by Grabowski and Berger [37] and used recently by Ruith et al. [79]

At the outlet we apply Neumann boundary conditions for each velocity component as in Ruith et al. [79]

$$\frac{\partial u_x}{\partial x}(x_0, r) = 0, \quad \frac{\partial u_r}{\partial x}(x_0, r) = 0, \quad \frac{\partial u_\theta}{\partial x}(x_0, r) = 0.$$

(3.2)

At the centerline we impose the conditions $u_r(x, 0) = 0$ and $u_\theta(x, 0) = 0$ due to the axisymmetry of the flow.

As emphasized by Ruith et al.[78] the use of free-slip boundary conditions in the radial direction requires excessively large computational domains to avoid backscatter from the radial boundaries. To truncate the domain at smaller radii, one must allow for mass and momentum to be exchanged across the radial boundary and thus account for entrainment of exterior fluid into the jet. To this end, no-viscous-traction boundary conditions in the radial direction[14]

$$\tau \cdot \boldsymbol{n} = 0$$

are applied where τ represents the viscous stress tensor and $\boldsymbol{n}$ stands for the unit normal vector in the lateral directions. In cylindrical coordinates this equation can be rewritten in component form as

$$\frac{\partial u_r}{\partial r}(x, R) = 0,$$
$$\frac{\partial u_r}{\partial x}(x, R) + \frac{\partial u_x}{\partial r}(x, R) = 0,$$
$$\frac{\partial u_\theta}{\partial r}(x, R) - \frac{u_\theta}{r}(x, R) = 0.$$

(3.3)

For our present investigation we neglect the fact that the inlet azimuthal velocity does not exactly satisfy the lateral boundary conditions (3.3). Following the argument given by Ruith et al., [78] however, we note that for both the Grabowski and Burgers profile the

stress tensor component corresponding to the azimuthal velocity at the radial edge of the domain decays like $1/R^2$ and therefore can be neglected for sufficiently large radial domains.

We remind the reader that the majority of past theoretical investigations used a no-flux radial boundary condition (reflecting the conservation of the total mass flux across the pipe) as well as a zero radial velocity at the outlet. In our study we analyze the vortex breakdown problem with open lateral boundary conditions and purely convective behavior at the outlet.

3.1.3   Numerical Simulations

The numerical simulations are based on the incompressible time-dependent axisymmetric Navier–Stokes equations in cylindrical coordinates (x, r, θ). The computational domain has the dimensionless size $R = 10$ and $x_0 = 20$; it is numerically resolved by $n_r = 127$ and $n_x = 257$ grid points in the radial and axial directions, respectively, with a uniform mesh in the axial direction and with an algebraic mapped mesh [43] in the radial direction which clusters grid points near the centerline and the lateral boundaries. To reach a steady state, simulations of the time-dependent Navier–Stokes equations were run until the L_2-norm of the difference of the velocity field from one time-step to the next became smaller than 10^{-11}.

The Grabowski profile [37] is used for the radial velocity, and the axial and azimuthal velocity components are defined piecewise for the regions inside and outside a characteristic radius. The Grabowski profile represents a smooth change from solid body rotation inside the characteristic radius and potential flow farther away. The velocity profile at the inflow boundary is forced to be axisymmetric and constant over time

$$
\begin{aligned}
&u_x(0, r) = 1, \\
&u_r(0, r) = 0, \\
&u_\theta\left(0, 0 \leq r \leq 1\right) = Sr(2 - r^2), \\
&u_\theta\left(0, 1 \leq r\right) = S/r.
\end{aligned}
\tag{3.4}
$$

The outflow convective boundary conditions used in numerical computations

$$
\frac{\partial u_x}{\partial t} + C\frac{\partial u_x}{\partial x} = 0, \quad \frac{\partial u_r}{\partial t} + C\frac{\partial u_r}{\partial x} = 0, \quad \frac{\partial u_\theta}{\partial t} + C\frac{\partial u_\theta}{\partial x} = 0
$$

which reduces, for the steady state, to (3.2) used in theory, were the same as in Ruith et al.. [78] The numerical simulations were carried out for zero normal viscous stress boundary conditions (3.3) on the lateral frontier of the domain.

The incompressible Navier–Stokes equations are solved by a pressure projection method [18]. Spatial derivatives are approximated with sixth-order compact schemes, and a fourth-order Runge-Kutta scheme is used for integration in time. The code used in the present

study was adapted from a code used to study nonswirling variable-density jets. For further details, please see Ref. [72].

As a representative reference case, a swirling jet is selected with the dimensionless governing parameters of $Re = 200$ and $S = 1.095$. This choice is identical to the reference cases obtained by Grabowski and Berger [37] and by Ruith et al. [79] This results in simulations that closely match the streamline patterns presented in figure 3 frames a and b of Ruith et al. [79]

The Recursive Projection Method (RPM) of Shroff and Keller [97] is used as a tool to stabilize the fixed-point iterative procedure and also as a convergence accelerator. RPM seeks to identify the space associated with the dominant eigenvalues and to eliminate its negative influence on the original fixed-point iteration by combining it with Newton iterations for the identified subspace. Once a steady state is found, the eigenvalues determined by the RPM procedure give directly its stability properties.

In order to demonstrate the bifurcation structure of the flow, a quantitative measure of the flow is needed to monitor the development of the steady state solutions as the governing parameters are varied. An appropriate diagnostic quantity is u_{xmin}, the minimum of the axial velocity in the meridional half-plane, which is equivalent to the minimum of axial velocity in the entire domain. In the current investigation, two governing parameters are varied, the swirl parameter S and the Reynolds number Re. For each choice of these parameters we compute a steady-state branch of the solution, where each new steady-state computation uses the previously calculated steady-state as an initial condition.

In Figure 3.2, the steady-state solution branch for $Re = 200$ represents the spatial evolution of streamlines dependent on the swirl parameter. In the figure, steady state solutions were computed at 342 separate values of S, u_{xmin} was extracted from each of these solutions and the solid curve was plotted through these points using linear interpolation. Here, we observe the gradual change of the solution from the columnar state (a) to vortex breakdown states (d, e, f). From this bifurcation structure the development of recirculation bubbles can be studied. As the swirl increases, the appearance of a single recirculation bubble indicates the initial onset of vortex breakdown. In the figure, this occurs when the bifurcation curve passes through point (c), where u_{xmin} first becomes negative owing to the presence of recirculation. As the swirl parameter increases further yet, a second recirculation bubble forms just downstream of the first, as shown in state (f).

In a similar fashion as figure 3.2, figure 3.3 shows the steady-state solution branch for $Re = 1000$, together with the swirl-dependent spatial evolution of the streamlines. In this case, 373 separate steady state solutions were computed, slightly more than in the previous case. More solutions were needed because of the small arc-length parameter necessary for continuation in the vicinity of the critical point labeled (b) in figure 3.3 where the slope of the bifurcation curve becomes vertical. This critical point (b) divides the stable columnar branch of the bifurcation curve from the unstable branch. The streamline pattern of solu-
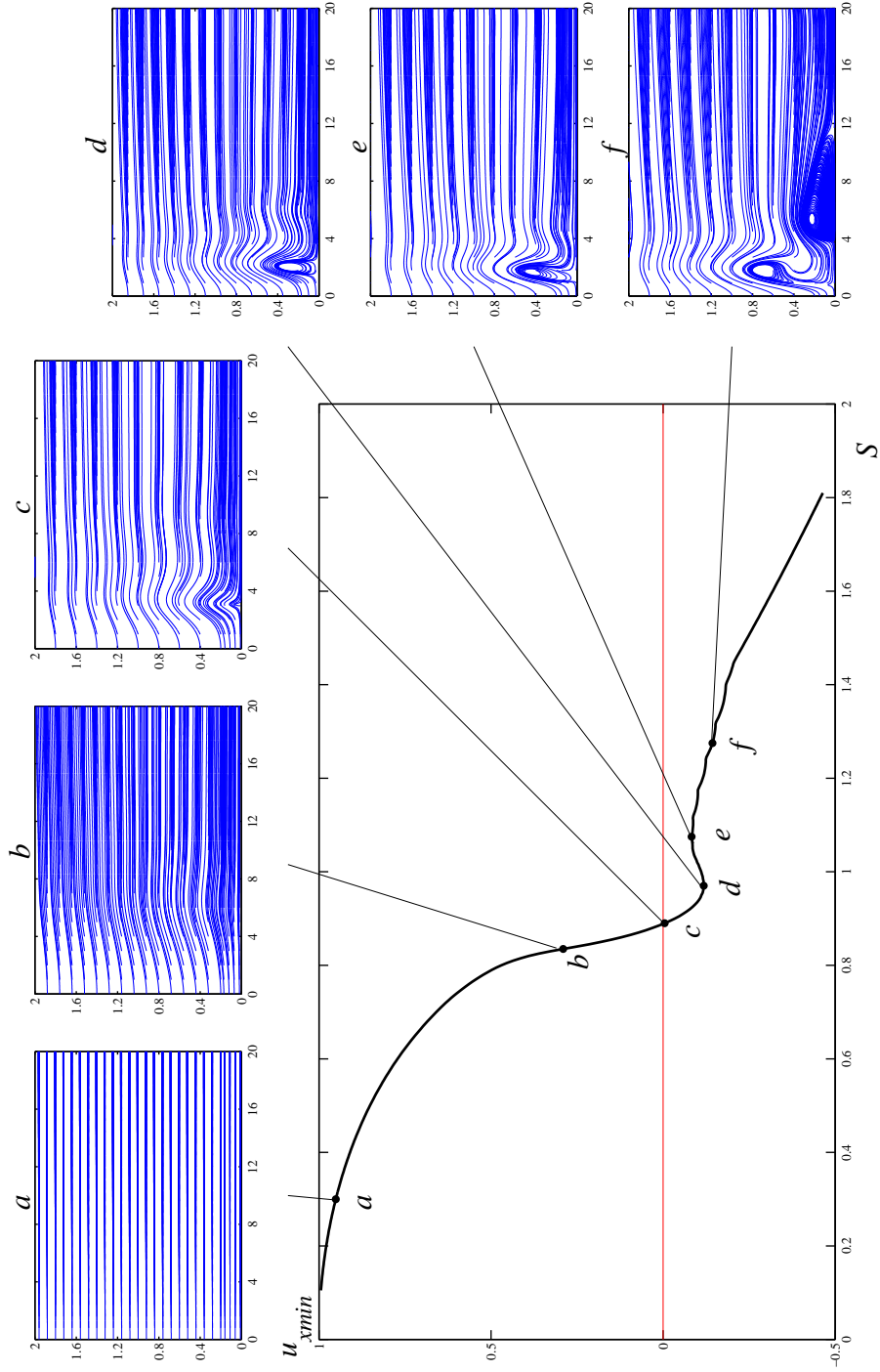
Figure 3.2: Bifurcation diagram describing the formation of vortex breakdown as the swirl is increased. The minimum axial velocity u_{xmin} is plotted as a function of the swirl number S for $Re = 200$. Each point along the bifurcation curve corresponds to a steady-state solution of the Navier–Stokes equations. The streamlines of some of the corresponding characteristic steady-states are shown on the top and on the right. The wiggles on the bifurcation diagram visible after $S = 1$ are converged (i.e. identical when the resolution is increased), they disappear when a less specific measure is taken as for example the overall mean value of u_x.
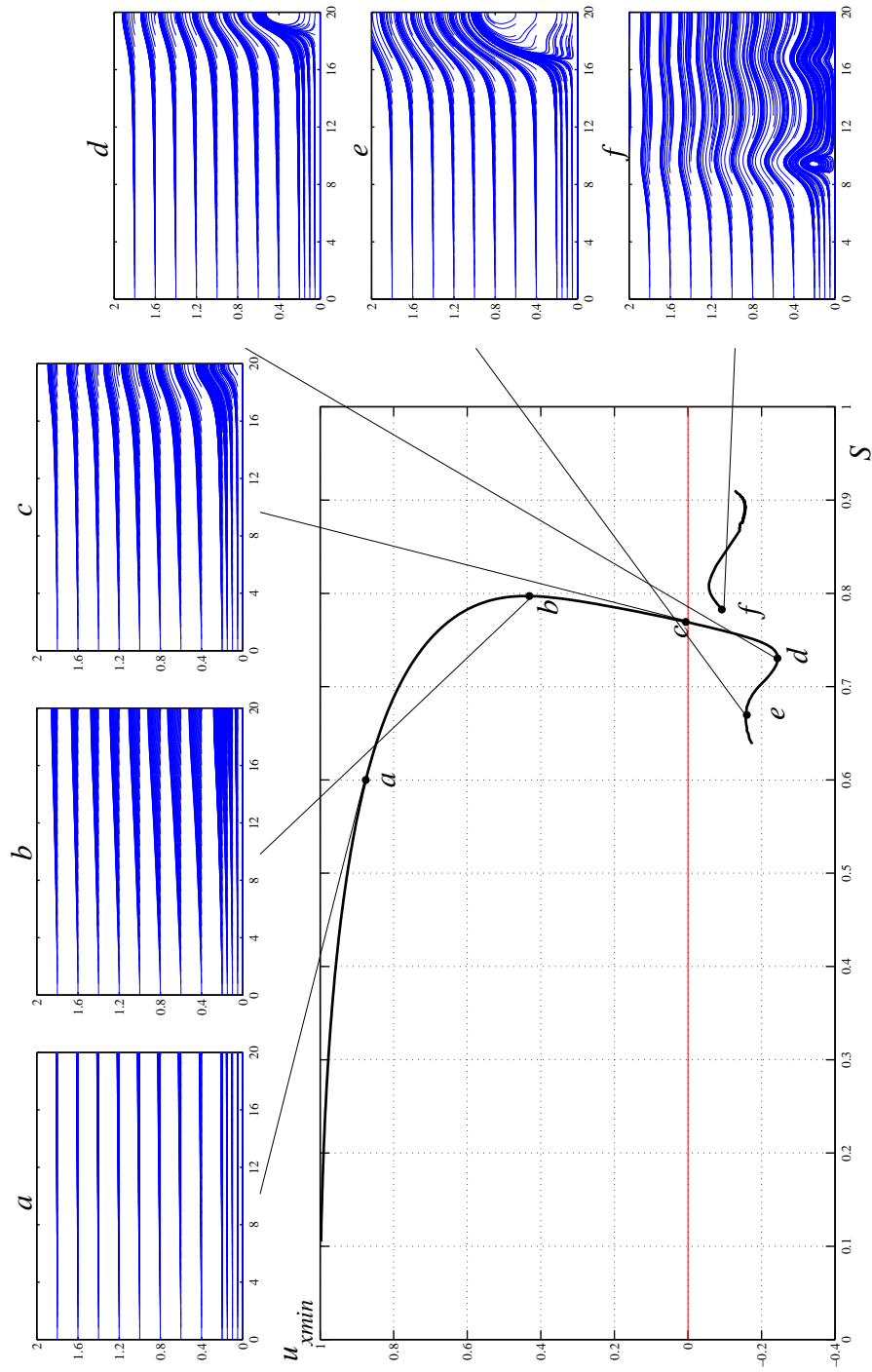
Figure 3.3: Bifurcation diagram describing the formation of vortex breakdown as the swirl is increased. The minimum axial velocity u_{xmin} is plotted as a function of the swirl number S for $Re = 1000$. Each point along the bifurcation curve corresponds to a steady-state solution of the Navier–Stokes equations. The streamlines of some of the corresponding characteristic steady-states are shown on the top and on the right.

65

tion state (a) in figure 3.3 is representative of the branch corresponding to the columnar state, which is characterized by relatively large positive values of u_{xmin}. Beyond the critical point (b), perturbations of the flow propagate downstream and a subsequent generation of the recirculation bubble is observed close to the outlet, as shown by the streamline plots corresponding to solution states (d) and (e). This is in contrast to the calculations shown in figure 3.2 where the recirculation bubble forms closer to the inlet, and means that the higher Reynolds number flow strongly interacts with outlet boundary conditions. Also in contrast to the previous calculations, where stable solutions are found along the entire bifurcation curve for $Re = 200$, solutions found beyond the critical point for $Re = 1000$ are linearly unstable. It is important to note, however, that the solutions become linearly unstable only beyond the critical point in the $Re = 1000$ case, and so this branch is referred to as the unstable steady-state branch to distinguish it from the stable columnar branch. Initializing DNS with this unstable state, we observe an exponential departure away from the initial condition and eventual convergence to the stable columnar branch. In the case of pipe flow, the unstable steady-state branch connects two stable branches (columnar and vortex breakdown), which are part of one curve with a fold as described by Ref. [64]. For the case considered here we found the spatial structure of the vortex breakdown branch to be highly sensitive to the swirl parameter when Reynolds numbers are high. This prevented us from following this entire branch and connecting it to the unstable one. In this region, a continuation increment of 10^{-5} or 10^{-6} on swirl parameter was needed to follow the bifurcation curve. In addition, each point along the curve required approximately 10^5 iterations to converge to a steady solution; therefore, this would require a total of 10^{10} iterations to traverse the necessary range of swirl numbers. Small portions of the vortex breakdown branch have been computed exhibiting one (streamline pattern (f), figure 3.3) or two bubbles depending on the swirl number value.

By examining the flow behavior (see the streamline patterns in figure 3.3) it is easy to conclude that the problem strongly depends on the outlet boundary conditions, *i.e.* the manner in which velocity perturbations leave the computational domain. The Neumann outlet boundary conditions allow an open recirculation region to exist. From a physical point of view this bubble comes from the outlet, and for a larger domain the vortex breakdown state will appear at smaller swirl parameter, and the recirculation bubbles will again form at the outlet in a similar way to figure 3.3.

3.1.4   The critical state of inviscid swirling flow

We consider a steady base flow given by an inviscid solution of the steady Euler equations which corresponds to transport downstream of the inlet boundary conditions (3.1). This base flow will be perturbed by an infinitesimal disturbances as:

$$u_x(x,r) = u_{x0} + \epsilon u_{x1}(x,r) + \dots,$$
$$u_r(x,r) = \epsilon u_{r1}(x,r) + \dots,$$
$$u_\theta(x,r) = S u_{\theta 0}(r) + \epsilon u_{\theta 1}(x,r) + \dots,$$
$$p(x,r) = p_0(r) + \epsilon p_1(x,r) + \dots,$$

where $\epsilon \ll 1$. Substitution into the Euler and continuity equations and considering only terms which are first order in ϵ results in the linearized equations:

$$
\begin{aligned}
u_{x0}\frac{\partial u_{x1}}{\partial x} + \frac{\partial p_1}{\partial x} &= 0, \\
u_{x0}\frac{\partial u_{r1}}{\partial x} + \frac{\partial p_1}{\partial r} - 2\frac{u_{\theta 0}u_{\theta 1}}{r}S &= 0, \\
u_{x0}\frac{\partial u_{\theta 1}}{\partial x} + \frac{u_{r1}}{r}\frac{\partial(ru_{\theta 0})}{\partial r}S &= 0, \\
\frac{\partial u_{x1}}{\partial x} + \frac{1}{r}\frac{\partial(ru_{r1})}{\partial r} &= 0.
\end{aligned}
\tag{3.5}
$$

Eliminating pressure from the first two equations of (3.5) we arrive at:

$$
\begin{aligned}
u_{x0}\frac{\partial^2 u_{r1}}{\partial x^2} - u_{x0}\frac{\partial^2 u_{x1}}{\partial xr} - 2\frac{u_{\theta 0}}{r}S\frac{\partial u_{\theta 1}}{\partial x} &= 0, \\
u_{x0}\frac{\partial u_{\theta 1}}{\partial x} + \frac{u_{r1}}{r}\frac{\partial(ru_{\theta 0})}{\partial r}S &= 0, \\
\frac{\partial u_{x1}}{\partial x} + \frac{1}{r}\frac{\partial(ru_{r1})}{\partial r} &= 0.
\end{aligned}
\tag{3.6}
$$

Subsequent substitution of the continuity equation and the expression for $u_{\theta 1}$ into the first equation of (3.6) reduces system (3.5) to the linear partial differential equation for the radial velocity, u_{r1}:

$$
\begin{aligned}
\frac{\partial}{\partial r}\left(\frac{1}{r}\frac{\partial ru_{r1}}{\partial r}\right) + \frac{\partial^2 u_{r1}}{\partial x^2} + S^2\frac{2u_{\theta 0}u_{r1}}{r^2 u_{x0}^2}\frac{\partial(ru_{\theta 0})}{\partial r} &= 0, \\
u_{r1}(x,0) = 0, \qquad\qquad \frac{\partial u_{r1}}{\partial r}(x,R) &= 0, \\
u_{r1}(0,r) = 0, \qquad\qquad \frac{\partial u_{r1}}{\partial x}(x_0,r) &= 0.
\end{aligned}
\tag{3.7}
$$

Equation (3.7) can be rewritten in the form $Lu_{r1} = 0$, where L is a linear partial differential operator defined by the following expression:

$$
L = \frac{\partial}{\partial r}\left(\frac{1}{r}\frac{\partial}{\partial r}r\right) + \frac{\partial^2}{\partial x^2} + S^2\frac{2u_{\theta 0}}{r^2 u_{x0}^2}\frac{\partial(ru_{\theta 0})}{\partial r}.
\tag{3.8}
$$

It is important to point out that this problem has nontrivial solutions only for specific values of S, corresponding to the bifurcation points. For other values of S, if a non-steady linear solution were computed, it would have a growth rate different from zero.

The solution of (3.7) $u_{r1}(x,r) = A\tilde{u}_{r1}(x,r)$ is obtained by separation of variables according to

$$
\tilde{u}_{r1}(x,r) = \sin(\lambda x)\Phi(r),
$$

where A denotes amplitude. The first eigenvalue S_1 of (3.7) defines the critical swirl of the flow. The critical swirl S_1 is a bifurcation point of solution branches of the steady Euler equation obtained by the above separation with $\lambda = \dfrac{\pi}{2x_0}$, where $\Omega_1 = S_1^2$ and $\Phi(r)$ are determined by the eigenvalue problem

$$\frac{d}{dr}\left(\frac{1}{r}\frac{d(r\Phi(r))}{dr}\right) + \left(-\lambda^2 + \Omega_1 \frac{2u_{\theta 0}}{r^2 u_{x0}^2}\frac{d(ru_{\theta 0})}{dr}\right)\Phi(r) = 0,$$

$$\Phi(0) = 0, \qquad \frac{d\Phi}{dr}(R) = 0. \tag{3.9}$$

The associated perturbation velocities are

$$\tilde{u}_{x1}(x,r) = (\cos(\lambda x) - 1)\frac{1}{\lambda}\frac{1}{r}\frac{d(r\Phi(r))}{dr},$$

$$\tilde{u}_{\theta 1}(x,r) = (\cos(\lambda x) - 1)\frac{S_1}{\lambda u_{x0}}\frac{\Phi(r)}{r}\frac{d(ru_{\theta 0})}{dr}.$$

Since we are solving the inviscid problem we do not enforce the lateral and outlet boundary conditions on the axial and azimuthal velocities deduced from $\tilde{u}_{r1}$.

3.1.5 Asymptotic expansion of near-critical swirling flows in the large Reynolds number limit

For small viscosities and small departure from the inviscid critical swirl S_1 we consider the perturbation approach used by Wang and Rusak [114] about the critical inviscid solution for S_1. They have shown that two small parameters have to be introduced measuring the viscosity and the closeness to the critical inviscid state $\Delta\Omega$ to maintain a uniformly valid solution in the neighborhood of the critical swirl. We let $\Omega = S^2$, $\Omega_1 = S_1^2$, and anticipating the dominant balance valid when perturbing a transcritical bifurcation, we set $\Omega = \Omega_1 + \epsilon\Delta\Omega'$ and $\nu = \epsilon^2\nu'$ with $\Delta\Omega' = O(1)$, $\nu' = O(1)$. We then assume a perturbed solution in the form

$$\begin{aligned}
u_x(x,r) &= u_{x0} + \epsilon u_{x1}(x,r) + \epsilon^2 u_{x2}(x,r) + \dots, \\
u_r(x,r) &= \epsilon u_{r1}(x,r) + \epsilon^2 u_{r2}(x,r) + \dots, \\
u_\theta(x,r) &= Su_{\theta 0}(r) + \epsilon u_{\theta 1}(x,r) + \epsilon^2 u_{\theta 2}(x,r) + \dots, \\
p(x,r) &= p_0(r) + \epsilon p_1(x,r) + \epsilon^2 p_2(x,r) + \dots,
\end{aligned} \tag{3.10}$$

where $\epsilon \ll 1$. The perturbation variables u_{x1}, u_{r1}, $u_{\theta 1}$ satisfy the following boundary conditions:

$$u_{x1}(0,r) = 0, \quad u_{r1}(0,r) = 0, \quad u_{\theta 1}(0,r) = 0,$$

$$u_{r1}(x,0) = 0, \quad u_{\theta 1}(x,0) = 0.$$

$$\frac{\partial u_{r1}}{\partial r}(x, R) = 0$$

$$\frac{\partial u_{r1}}{\partial x}(x_0, r) = 0.$$

We enforce the same boundary conditions on the higher-order terms u_{x2}, u_{r2}, $u_{\theta 2}$.

At leading order ϵ we recover the linear equation (3.7) with $S^2 = \Omega_1$, which can be formally written as $Lu_{r1} = 0$, where L is defined by (3.8). As described in section IV the solution of this equation is

$$u_{r1}(x, r) = A\tilde{u}_{r1}(x, r) = A \sin(\lambda x)\Phi(r),$$

with A as an arbitrary amplitude to be determined by compatibility equations at higher order, $\lambda = \dfrac{\pi}{2x_0}$ and $\Phi(r)$ as the solution of (3.9).

At second order the linearized operator L applied to u_{r2} is forced by terms stemming from the lower-order solution

$$
\left[u_{x0}\frac{\partial}{\partial r}\left(\frac{1}{r}\frac{\partial r u_{r2}}{\partial r}\right) + u_{x0}\frac{\partial^2 u_{r2}}{\partial x^2} + \Omega_1\frac{2u_{\theta 0}u_{r2}}{r^2 u_{x0}}\frac{\partial(r u_{\theta 0})}{\partial r} \right] =
$$

$$
= -A^2\left[\left(-\frac{\tilde{u}_{r1}}{r} + \tilde{u}_{x1}\frac{\partial}{\partial x} + \tilde{u}_{r1}\frac{\partial}{\partial r}\right)\left(\frac{\partial \tilde{u}_{r1}}{\partial x} - \frac{\partial \tilde{u}_{x1}}{\partial r}\right) - \frac{2\tilde{u}_{\theta 1}}{r}\frac{\partial \tilde{u}_{\theta 1}}{\partial x}\right] -
$$

$$
- A^2\left[\frac{2u_{\theta 0}\sqrt{\Omega_1}}{r u_{x0}}\left(\tilde{u}_{x1}\frac{\partial \tilde{u}_{\theta 1}}{\partial x} + \frac{\tilde{u}_{r1}}{r}\frac{\partial r\tilde{u}_{\theta 1}}{\partial r}\right)\right] - A\Delta\Omega'\frac{2u_{\theta 0}\tilde{u}_{r1}}{r^2 u_{x0}}\frac{\partial(r u_{\theta 0})}{\partial r} +
$$

$$
+ \nu'\Omega_1\frac{2u_{\theta 0}}{r u_{x0}}\frac{\partial}{\partial r}\left(\frac{1}{r}\frac{\partial(r u_{\theta 0})}{\partial r}\right).
$$

Here the first term in the right-hand side of the equation is not linear, being proportional to A^2, and corresponds to the transport of the perturbation by the perturbation. The second term is linear in A and originates from the change of the linearized operator with swirl parameter. The last term is independent of A and represents the effect of viscosity on the base flow.

This equation may be formally written as $Lu_{r2} = \sigma(\tilde{u}_{x1}, \tilde{u}_{r1}, \tilde{u}_{\theta 1}, u_{\theta 0})$. It is easy to show that equation (3.7) is self-adjoint with respect to the scalar product

$$\langle u_r'|u_r\rangle = \iint u_r' u_r \, r \, dr \, dx.$$

Using the compatibility condition (Fredholm alternative) to find u_{r2} we need the forcing $\sigma(\tilde{u}_{x1}, \tilde{u}_{r1}, \tilde{u}_{\theta 1}, u_{\theta 0})$ to be orthogonal to the kernel of the adjoint that reads here $\langle \tilde{u}_{r1}|\sigma\rangle = 0$, giving:

$$A^2 M_1 - A\Delta\Omega' M_2 + \nu' M_3 = 0, \tag{3.11}$$

69

with

$$M_1 = \int_0^{x_0} \int_0^R \left[\left(-\frac{\tilde{u}_{r1}}{r} + \tilde{u}_{x1}\frac{\partial}{\partial x} + \tilde{u}_{r1}\frac{\partial}{\partial r} \right) \left(\frac{\partial \tilde{u}_{r1}}{\partial x} - \frac{\partial \tilde{u}_{x1}}{\partial r} \right) - \frac{2\tilde{u}_{\theta1}}{r}\frac{\partial \tilde{u}_{\theta1}}{\partial x} \right] \tilde{u}_{r1} r dr dx$$
$$+ \int_0^{x_0} \int_0^R \frac{2u_{\theta0}\sqrt{\Omega_1}}{ru_{x0}} \left(\tilde{u}_{x1}\frac{\partial \tilde{u}_{\theta1}}{\partial x} + \frac{\tilde{u}_{r1}}{r}\frac{\partial r\tilde{u}_{\theta1}}{\partial r} \right) \tilde{u}_{r1} r dr dx,$$

$$M_2 = -\int_0^{x_0} \int_0^R \frac{2u_{\theta0}\tilde{u}_{r1}}{r^2 u_{x0}}\frac{\partial(ru_{\theta0})}{\partial r}\tilde{u}_{r1} r dr dx,$$

$$M_3 = -\int_0^{x_0} \int_0^R \Omega_1 \frac{2u_{\theta0}}{ru_{x0}}\frac{\partial}{\partial r} \left(\frac{1}{r}\frac{\partial(ru_{\theta0})}{\partial r} \right) \tilde{u}_{r1} r dr dx.$$

Integration over x leads to

$$M_1 = \frac{x_0^2}{\pi^2 u_{x0}^2}N_1, \quad M_2 = \frac{x_0}{u_{x0}}N_2, \quad M_3 = \frac{4\Omega_1 x_0}{\pi u_{x0}}N_3$$

with

$$N_1 = -2\left(\pi - \frac{4}{3}\right)\Omega_1 \int_0^R \frac{\partial}{\partial r}\left(u_{\theta0}\frac{\partial(ru_{\theta0})}{\partial r} \right)\frac{\Phi^3}{r}dr + \frac{\pi^2 u_{x0}^2}{12x_0^2}\int_0^R \left[(3\pi - 8)\Phi + 3\pi\Phi_r r \right]\Phi^2 dr -$$
$$- u_{x0}^2 \left(\pi - \frac{4}{3}\right)\int_0^R \frac{(\Phi_r\Phi_{rr} - \Phi\Phi_{rrr})r^3 + (\Phi\Phi_{rr} + \Phi_r^2)r^2 + 3\Phi\Phi_r r - 4\Phi^2}{r^2}\Phi dr,$$

$$N_2 = -\int_0^R \frac{u_{\theta0}}{r}\frac{\partial(ru_{\theta0})}{\partial r}\Phi^2 dr, \tag{3.12}$$

$$N_3 = -\int_0^R u_{\theta0}\frac{\partial}{\partial r}\left(\frac{1}{r}\frac{\partial(ru_{\theta0})}{\partial r} \right)\Phi dr.$$

For the Grabowski profile, where the axial flow is uniform and equal to $u_{x0} = 1$, it can be shown that N_1 and N_3 are positive.

Equation (3.11) has a real solution for A if

$$|\Delta\Omega'| \geq 2\frac{\sqrt{M_1 M_3}}{|M_2|}\sqrt{\nu'} = 4\frac{\sqrt{N_1 N_3}}{|N_2|}\sqrt{\frac{\nu' x_0 \Omega_1}{\pi^3 u_{x0}}}. \tag{3.13}$$

If $|\Delta\Omega'| < 2\sqrt{M_1 M_3 \nu'}/|M_2|$, equation (3.11) has no real solutions; as mentioned by Wang and Rusak, [114] in this case no steady viscous solution exists near the critical point.

70

3.1 The Bifurcation Structure of Viscous Steady Axisymmetric Vortex Breakdown with Open Lateral Boundaries

Close to the critical state, with condition (3.13) satisfied,

$$A = \frac{\Delta\Omega' M_2 \pm \sqrt{(\Delta\Omega')^2 M_2^2 - 4\nu' M_1 M_3}}{2M_1} = \frac{\Delta\Omega' N_2 \pm \sqrt{(\Delta\Omega')^2 N_2^2 - 16\nu' x_0 \Omega_1 N_1 N_3/(\pi^3 u_{x0})}}{2x_0 N_1/(\pi^2 u_{x0})}.$$

$$(3.14)$$

Multiplying (3.13) by ϵ we get that $|\Delta\Omega| = 2\sqrt{M_1 M_3 \nu}/|M_2|$ meaning that no solution exists between $S_{c\nu 1}$ and $S_{c\nu 2}$

$$S_{c\nu 1}^2 = \Omega_1 - 4\frac{\sqrt{N_1 N_3}}{|N_2|}\sqrt{\frac{\nu x_0 \Omega_1}{\pi^3 u_{x0}}},$$

$$S_{c\nu 2}^2 = \Omega_1 + 4\frac{\sqrt{N_1 N_3}}{|N_2|}\sqrt{\frac{\nu x_0 \Omega_1}{\pi^3 u_{x0}}}$$

which defines a saddle fold bifurcation point of the steady axisymmetric Navier–Stokes solution. The value $S_{c\nu 1}^2$ corresponds to the first viscous correction to the inviscid critical swirl. [114]

Starting from (3.10), (3.9) and (3.14), multiplying by ϵ and neglecting all terms of higher order, the asymptotic expansion near the critical swirl Ω_1 reads

$$u_x(x,r) = u_{x0} + \frac{\Delta\Omega N_2 \pm \sqrt{(\Delta\Omega)^2 N_2^2 - 16\nu x_0 \Omega_1 N_1 N_3/(\pi^3 u_{x0})}}{2x_0 N_1/(\pi^2 u_{x0})}(\cos(\lambda x) - 1)\frac{1}{\lambda}\frac{1}{r}\frac{\partial(r\Phi(r))}{\partial r},$$

$$u_r(x,r) = \frac{\Delta\Omega N_2 \pm \sqrt{(\Delta\Omega)^2 N_2^2 - 16\nu x_0 \Omega_1 N_1 N_3/(\pi^3 u_{x0})}}{2x_0 N_1/(\pi^2 u_{x0})}\sin(\lambda x)\Phi(r),$$

$$u_\theta(x,r) = S u_{\theta 0}(r) +$$

$$+\frac{\Delta\Omega N_2 \pm \sqrt{(\Delta\Omega)^2 N_2^2 - 16\nu x_0 \Omega_1 N_1 N_3/(\pi^3 u_{x0})}}{2x_0 N_1/(\pi^2 u_{x0})}(\cos(\lambda x) - 1)\frac{S}{\lambda u_{x0}}\frac{\Phi(r)}{r}\frac{\partial(r u_{\theta 0})}{\partial r}.$$

$$(3.15)$$

Careful analytical investigation of the expression for the axial velocity (3.15) shows that the minimum axial velocity always occurs at the centerline of the domain at the outlet for the decelerated state. Thus, the minimum axial velocity in the whole domain u_{xmin} is equivalent to $u_x(x_0, 0)$.

We conclude, as in the pipe flow considered by Wang and Rusak, [114] that, for a small but finite viscosity, the modified transcritical bifurcation of the Euler solution consists of two Navier–Stokes branches about Ω_1 with a finite gap between these two branches equal to $8\frac{\sqrt{N_1 N_3}}{|N_2|}\sqrt{\frac{\nu x_0 \Omega_1}{\pi^3 u_{x0}}}$.

The bifurcation diagram in terms of the minimum axial velocity, u_{xmin}, along the centerline, evaluated by using (3.15), is a nonlinear function in $\Delta\Omega$. Steady columnar flow at

leading order exists for $S^2 < S^2_{c\nu 1}$ and $S^2 > S^2_{c\nu 2}$. The branches are not connected and the resulting gap near the critical swirl demonstrates that no near-columnar axisymmetric state exists for the corresponding range of the swirl parameter. Outside this region two near-columnar equilibrium states can exist for the same boundary conditions. For $S^2 < S^2_{c\nu 1}$ one branch describes a nearly columnar state, the other a decelerated axial flow which corresponds to the unstable steady-state branch described in section III. The deceleration is evident in the streamline plots of figure 3.3, since the streamlines diverge as the flow develops downstream in this case. For $S^2 > S^2_{c\nu 2}$ one branch consists of the accelerated state and then second relaxes toward the columnar state.

3.1.6 Grabowski profile

For the Grabowski profile (3.4) we compute the eigenfunction Φ to determine the bifurcation behavior based on our asymptotic results. A spectral method based on Chebyshev polynomials (see, e.g., Schmid and Henningson [96]) was used to solve equation (3.9) resulting in the eigenfunction $\Phi(r)$ displayed in figure 3.4 by the solid thick line. The equation (3.9) outside the characteristic radius $r = 1$ can be solved analytically, which gives the exact value $\Phi(R) = 0.02704144306$ once the equation has been integrated in the core. The numerical integration in this outer region produces $\Phi(R) = 0.027041443046$, which allows us to estimate the numerical error to be on the order of 10^{-11}. The constants $N_1 = 0.059819851197575$, $N_2 = -0.070295010313843$ and $N_3 = 0.763981542125681$ were computed using Clenshaw-Curtis quadrature to approximate the integrals (3.12) (see, e.g., Trefethen [105]).

To test the validity of these asymptotic results, we compare them to the results obtained from numerical simulations (section III). Figure 3.5 compares the same solution branch for Reynolds numbers $Re = 2000$ and $Re = 1500$ obtained from numerical simulations (dashed thick and thin lines, respectively) and the asymptotic solution (solid lines of corresponding thickness). The straight black lines represent bifurcation curves for the inviscid case, and the intersection of the two straight lines defines the inviscid critical swirl number S_1. Perturbations increase as the Reynolds number decreases, which qualitatively agrees with the numerical results. [107] A similar dependence of the solution on the Reynolds number has already been discussed for the pipe case. [114]

Despite a Reynolds number of only $Re = 2000$, we obtain a good agreement between numerical calculations and asymptotic analysis from Section V. We expect an even closer match between the analytic and numerical bifurcation curves for higher Reynolds numbers; this attempt, however, would require a significantly larger resolution (*i.e.*, denser computational grid, which in turn necessitates a smaller time step and an increased number of iterations to obtain the steady state solution), the CPU time to calculate stable and unstable branches would be computationally too expensive.

Since we have verified that the extended analysis agrees well with the numerical simula-
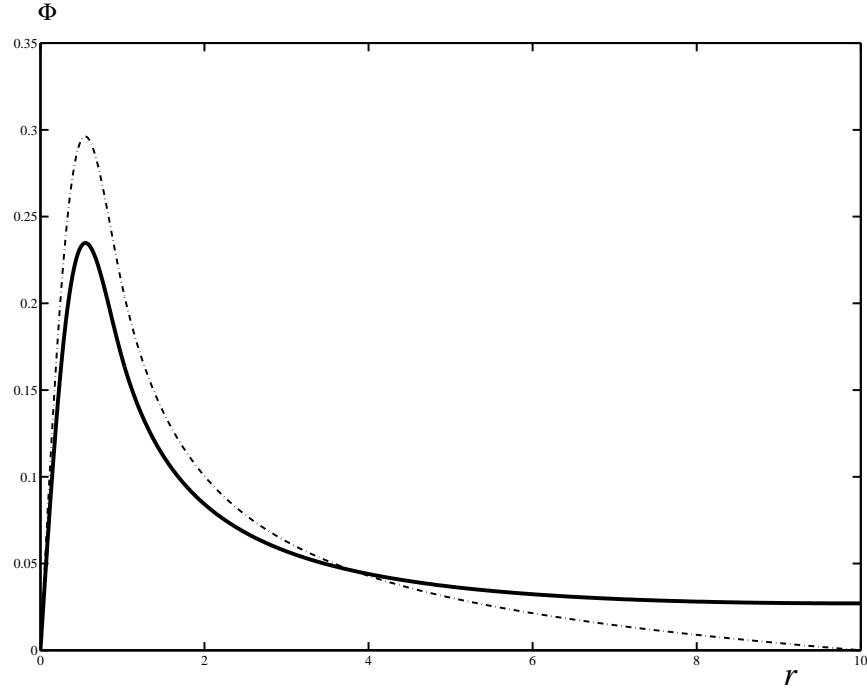
Figure 3.4: The normalized eigenfunctions for a Grabowski profile. The thick solid line corresponds to open flow; the dash-dotted line to a flow in a straight pipe.

tions for $Re = 2000$, we may now use this tool to explore the effects of differing conditions at lateral and outlet boundaries. First, we compare our problem with open lateral boundaries to the flow in a pipe in which the lateral boundary condition is changed from an open, traction-free condition to a closed, free slip condition:

$$u_{r1}(x, R) = 0,$$

while keeping the same outlet (Neumann) boundary conditions.

The eigenfunction $\Phi(r)$ corresponding to this case is shown in figure 3.4 by the dash-dotted line. One can observe a moderate difference between the two curves, but they have roughly the same shape. Even though the behavior of the curves near the lateral boundary at $r = 10$ is different (the solid curve remains non-zero allowing entrainment whereas the dash-dotted curve does not), the peaks of the curves, near the center of the domain, are about the same height and width. This indicates that the problem is only weakly sensitive to the type of imposed lateral boundary conditions.

The bifurcation curves corresponding to open and closed lateral boundaries (figure 3.6) also demonstrate that the solution depends very weakly on the lateral boundary conditions. Figure 3.6 also reports results obtained by Wang and Rusak[114] on a pipe flow
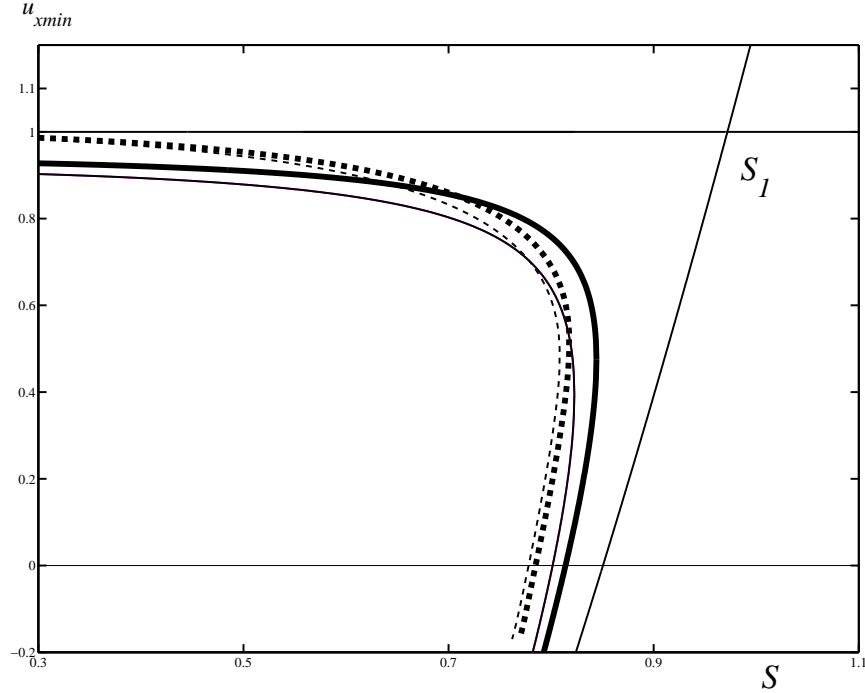
Figure 3.5: Bifurcation curves obtained from asymptotic analysis for $Re = 1500$ (thin solid line), $Re = 2000$ (thick solid line) and from numerical simulations for $Re = 1500$ (thin dashed line) and $Re = 2000$ (thick dashed line).

with a different outlet condition (Dirichlet). The difference is larger than when the lateral boundary condition alone is modified. This demonstrates a higher sensitivity to outlet boundary condition. We found that the critical inviscid swirl number in the present case is $\Omega_1 = 0.94463073$ which is smaller than for a pipe with a Dirichlet boundary condition at the outlet, where $\Omega_1 = 0.95064678$, as reported by Wang and Rusak. [114]

3.1.7 Discussion and Conclusions

In this paper we investigated the influence of a small but finite viscosity on the bifurcation diagram of axisymmetric swirling Euler flow with traction-free lateral and convective outlet boundary conditions. We study the flow stability by investigating the bifurcation structure of steady state solutions to the above problem. This has been accomplished both by means of numerical simulations and theoretical analysis.

To validate our numerical simulations, we first considered the bifurcation structure of a low Reynolds number case ($Re = 200$) as shown in figure 3.2. For this case, our computed steady state solutions agreed very well with those found in the literature. [79] Figure 3.2 shows that for small Reynolds numbers only one equilibrium solution exists, which repre-
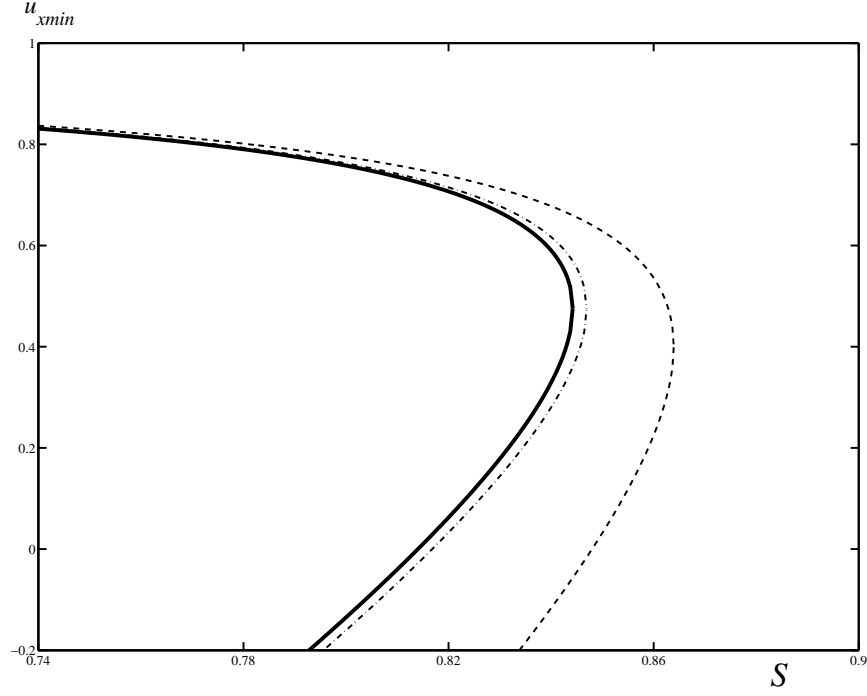
Figure 3.6: Bifurcation curves obtained from asymptotic analysis for $Re = 2000$. The solid black line corresponds to the Neumann outlet problem with open lateral boundaries, the dash-dotted line to flow in a pipe opened at the outlet and the dashed curve to a flow in a pipe with zero radial velocity at the outlet.[114]

sents the smooth monotonic change from the near-columnar state to vortex breakdown.

Numerical simulations and an asymptotic expansion about the critical swirl parameter for higher Reynolds numbers were also developed. The asymptotic analysis was carried out in a similar manner to Wang and Rusak[114] but for different boundary conditions, namely open lateral and outlet boundaries. As discussed in the introduction, such a set of boundary conditions allows us to expand the theory of the swirling flows involving vortex breakdown to flow configurations such as combustion chambers, delta wings and many others. It was shown that in a neighborhood of S_1 small but finite viscosity causes the steady Euler solution to give rise to two steady Navier–Stokes solutions whose branches show a gap. A small-disturbance analysis revealed a dependence on both viscosity as well as on a measure of the closeness to the critical swirl. It showed the existence of two critical viscous thresholds in parameter space, such that $S_{c\nu 1}^2 < S_1^2 < S_{c\nu 2}^2$, with the size of the gap $(S_{c\nu 1}^2 - S_{c\nu 2}^2)$ proportional to $\sqrt{\nu x_0 S_1^2}$. This means that no quasi-columnar states exist for $S_{c\nu 1}^2 < S_1^2 < S_{c\nu 2}^2$. Experimental and numerical investigations conducted in this parameter range should obtain only one equilibrium solution: the vortex breakdown state. Outside this parameter range, however, up to three equilibrium states (quasi-columnar, decelerated or accelerated and vortex-breakdown) exist for identical boundary conditions and suffi-

ciently large Reynolds numbers, as shown in figure 3.1. In this case, the decelerated state represents an unstable steady state and lies between the two other (columnar and vortex breakdown) states which are stable.

In spite of the fact that the inlet azimuthal velocity does not exactly satisfy the lateral boundary conditions, the present asymptotic analysis displayed good agreement with numerics, as shown in figure 3.5. Also, both the numerical and theoretical investigations found that the flow near the critical swirl is more sensitive to the outlet boundary conditions than to the lateral ones. Figure 3.6 shows that the asymptotic results changed more appreciably when the outlet boundary condition changed from Neumann to Dirichlet, in contrast to a change of the lateral boundaries from open to closed. From figure 3.3, we interpret the sensitivity of the solution to the outlet boundary condition to be caused by the nucleation of a recirculation bubble at the outlet boundary.

Asymptotic analysis also predicts the existence of an upper breakdown-free state for $S > S_{cv2}$, corresponding to the accelerated state.[114] We wish to point out, however, that the viscous corrections in expansion (3.10) are valid for $\epsilon \ll |S_2 - S_1|$, where S_2 is the second eigenvalue of problem (3.9). In our case ($Re = 2000$) these values are of the same order, *i.e.* $\epsilon \sim |S_2 - S_1| \sim 0.02$, indicating that $Re = 2000$ is a too small Reynolds number to apply the theory for $S > S_{cv2}$, meaning that the upper fold might not exist for such a moderate Reynolds number. As mentioned above, we expect a better match between the analytic and numerical solutions as the Reynolds number increases.

3.2 Convergence of the various branches in the bifurcation diagram

In this part of the chapter we discuss the numerical convergence of the various branches of the bifurcation curve presented in figure 3.3. We recall that the Reynolds number Re is set to 1000 and that S varies along the branches.

3.2.1 Saddle node

Here we carry out a numerical resolution check similar to the one discussed at the end of Chapter 2. Two points are chosen near the first saddle node bifurcation, point A lying on the stable branch and point B on the unstable branch. We compute these solutions with different resolutions:

- N_1: ($N_R = 127$, $N_x = 257$) ('coarse')

- N_2: ($N_R = 253$, $N_x = 513$) ('double')

- N_3: ($N_R = 379$, $N_x = 769$) ('triple')

- N_4: ($N_R = 505$, $N_x = 1025$) ('quadruple', the 'finest' resolution assumed close to the exact solution).

Point A: stable branch close to the first saddle node

The first point for the comparison lies on the near-columnar branch near to the turning point ($S = 0.7896234$), where the solution is expected to be very sensitive to any 'perturbation' induced by changes in the spatial resolution. Figure 3.7 (a) displays the magnitude of the velocity $|\vec{u}_{N_4}| = \sqrt{(u_x^2 + u_r^2 + u_\theta^2)}$ for the finest solution N_4 and its maximum is 1.3, i.e. of $O(1)$. Figure 3.7 (b),(c),(d) show the error field $|\delta\vec{u}_n(x,r)|$ for resolutions $n = N_1$, N_2 or N_3 compared to the solution computed with resolution N_4, where for any given location (x,r), $\delta\vec{u}_n(x,r) = \vec{u}_n(x,r) - \vec{u}_{N_4}(x,r)$. In this expression all quantities are evaluated numerically at locations (x,r) belonging to the coarsest grid N_1 point. All grid points of N_1 also belong to all the other grids without the need of interpolation, which could potentially cause extra errors.

In all cases the error field appears to be localized near the centerline at the outlet of the computational domain (right bottom corner). Quantitatively, the relative error (the ratio between the maximum of the error field and the maximum magnitude of velocity for the finest solution N_4) is 3.8%, 0.69% and 0.185% for the resolutions N_1, N_2 and N_3, respectively. In this case even the coarsest resolution N_1 can be considered as sufficient to capture the physical solution, whereas the solutions obtained using grids N_2 and N_3 show only negligible differences with the exact solution. We can thus conclude that the solution on the stable near-columnar branch is numerically robust, even close to the saddle.

Figure 3.7: Point A: Resolution test for $S = 0.7896234$, $Re = 1000$ (stable branch). Magnitude of the velocity of the finest solution using grid resolution N_4 (a). Field error for lower resolutions $|\delta \vec{u}_n(x, r)| = |\vec{u}_n(x, r) - \vec{u}_{N_4}(x, r)|$: $n = N_1$ (b), N_2 (c) and N_3 (d). $L^\infty-$ (blue) and L^2- (red) norms of the error field for various resolutions with step δx.

Figure 3.7(e) shows the error computed on the grid N_1, as a function of the resolution, using the $L^\infty-$ (blue line) and the L^2- (red line) norms. The L^∞-norm refers to the maximum of the error field $|\delta\vec{u}_n(x,r)|$ over all grid points: $||\delta\vec{u}||_\infty = \max\limits_{x_i,r_j} |\delta\vec{u}(x_i,r_j)|$. The L^2-norm is the Euclidian norm over the whole grid mesh: $||\delta\vec{u}||_2 = \sqrt{\dfrac{1}{N_R N_x}\sum\limits_{i=1}^{N_x}\sum\limits_{j=1}^{N_R}|\delta\vec{u}(x_i,r_j)|^2}$.

Not that it is *not* the energy norm of the error field since it does not take into account the r factor for the cylindrical integration, nor any weight factors due to the non uniformity in r of the grid. The slopes interpolated from figure 3.7(e) for the resolutions N_2 and N_3 is close to 3 and suggests at least the third order accuracy of the spatial numerical scheme.

Point B: unstable branch close to the first saddle node

The next point under investigation, point B, lies on the unstable branch ($S = 0.7857949$). Using the same analysis, we found that the maximum magnitude of the velocity for the exact solution is 1.3, see frame (a) of figure 3.8. The relative error is 2.47%, 0.36% and 0.07% for the resolutions N_1, N_2 and N_3, respectively, see plots in figure 3.8 (b),(c),(d), correspondingly. Hence, the coarsest grid N_1 is presently sufficient, and the solution obtained using grids N_2 and N_3 are almost identical to the finest solution. We conclude that the solution on the unstable branch near the bifurcation point is numerically robust as well. The slopes of the error norms $||\delta\vec{u}||_\infty$ and $||\delta\vec{u}||_2$ are close to 3 even though they seem slightly steeper for higher resolution (see figure 3.8 (e)), which suggests at least third order for the spatial scheme. Note that the expected fourth order for the method requires in principle asymptotically small grid spacing.

3.2.2 Solution with recirculation region

Figure 3.9 shows the bifurcation diagram for $Re = 1000$. It displays the dependence of the minimum of axial velocity in the whole domain u_{xmin} versus the swirl parameter S. Here green circles correspond to resolution N_1 (shown in black lines on the figure 3 in the previous part of the chapter), magenta circles correspond to resolution N_2, black circles correspond to resolution N_3 and red points correspond to resolution N_4.

As already discussed above, all solutions near to the saddle node are numerically robust with respect to the spatial resolution. However, the diagram 3.9 demonstrates that for point C at $S = 0.7361936$ there is a large discrepancy between the solutions calculated with the coarse resolution N_1 and others (N_2, N_3, N_4).

Figure 3.10 confirms this conclusion. The maximum magnitude of the velocity for the exact solution is of 1.25 (figure 3.10 (a)). For the resolutions N_1, N_2 and N_3, the maximum of the error field is 8.1%, 0.9% and 0.17%, respectively (figure 3.10 (b), (c), (d)). We observe from figure 3.10 that N_2 is sufficient, and that N_3 shows negligible differences with the finest solution. The slopes of the error fields norms $||\delta\vec{u}||_\infty$ and $||\delta\vec{u}||_2$ are close to 3 even though
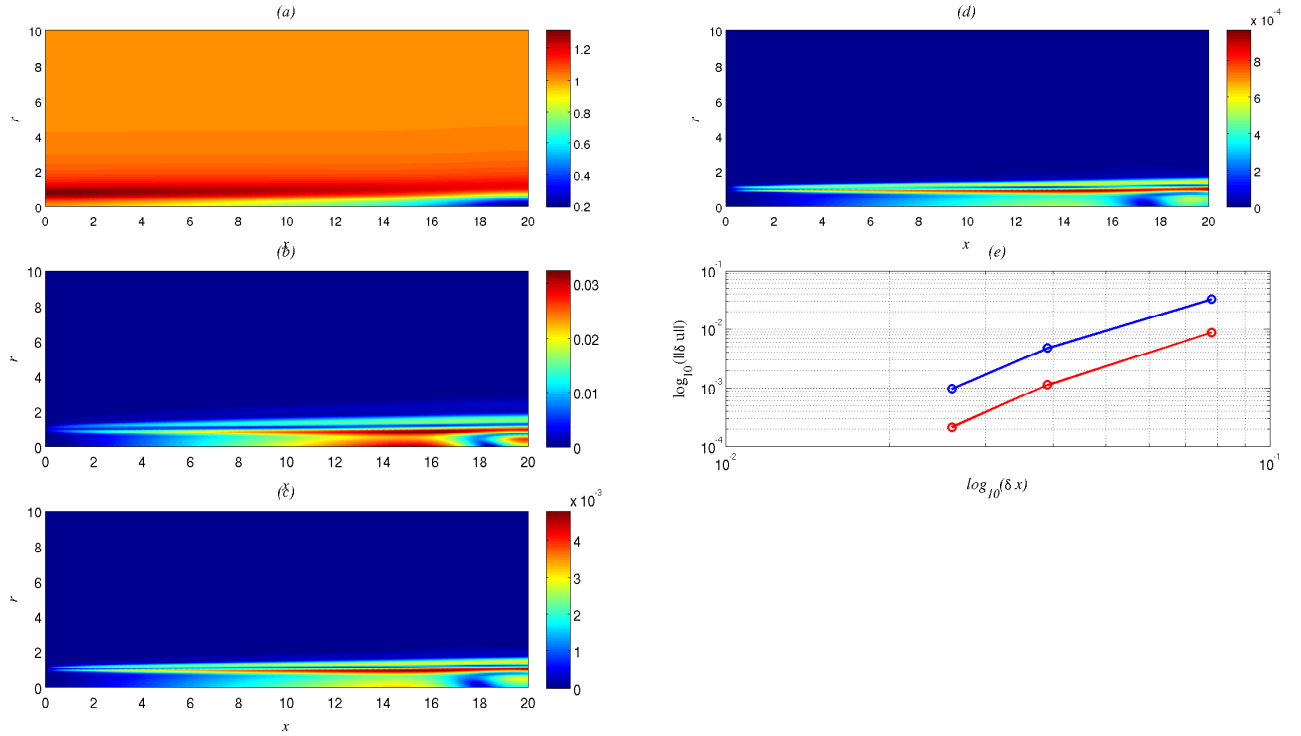
Figure 3.8: Point B: Resolution test for $S = 0.7857949$, $Re = 1000$ (unstable branch). Magnitude of the velocity for the exact solution using grid resolution N_4 (a). Pointwise magnitude of the error for lower resolutions: N_1 (b), N_2 (c) and N_3 (d). $L^\infty-$ (blue) and L^2- (red) norms of the error for various resolutions with step δx.
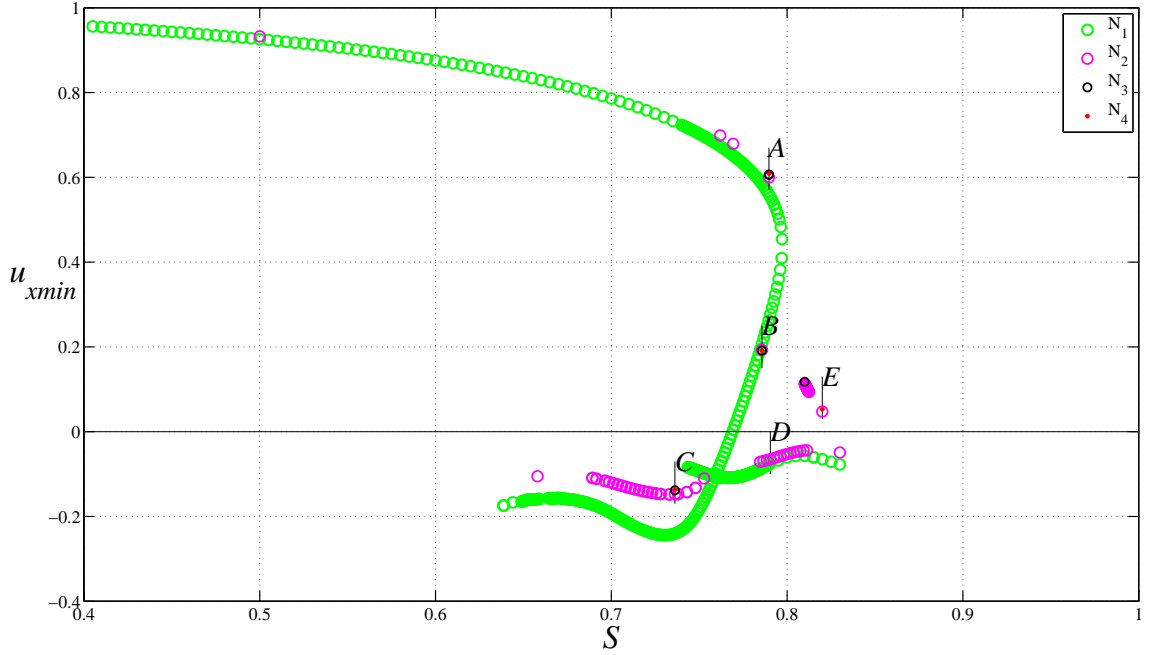
Figure 3.9: Bifurcation diagram for $Re = 1000$, minimum of axial velocity in the whole domain u_{xmin} versus the swirl parameter S. Here green circles correspond to resolution N_1, magenta circles correspond to resolution N_2, black circles to resolution N_3 and red points to resolution N_4.

they seem slightly steeper for the higher resolution, and suggests at least the third order accuracy of the spatial numerical scheme, see figure 3.10 (e). Note nevertheless that the maximum discrepancies appear in a small localized region near the centerline at the outlet of the computational domain (right bottom corner). However, the 8.1% is the maximum error in the velocity field between the coarser grid N_1 and the finer grid N_4 does not modify substantially the streamlines between grids N_1 (figure 3.11 (a)) and N_4 (figure 3.11 (b)).

A convergence test has been carried out for the point D on the stable solution branch with the recirculation region for $S = 0.7904633$ between the solutions obtained with grids N_1 and with N_2.

Frame (a) and (b) of figure 3.12 represent the streamline pattern of the solution obtained using grids N_1 and N_2, respectively. Here we assume that the solution computed on the finer grid N_2 is close to the exact solution; the magnitude of the velocity is shown in plot (c) figure 3.12, and the point-wise magnitude of the error for lower resolutions N_1 presented in plot (d). In the case of N_2 we only found that the recirculation bubble has moved slightly closer to the inlet than with N_1. The deceleration region has however not changed much. In order to confirm this fact we note that the maximum error is localized in the neighborhood of the first recirculation bubble and that the magnitude of the relative
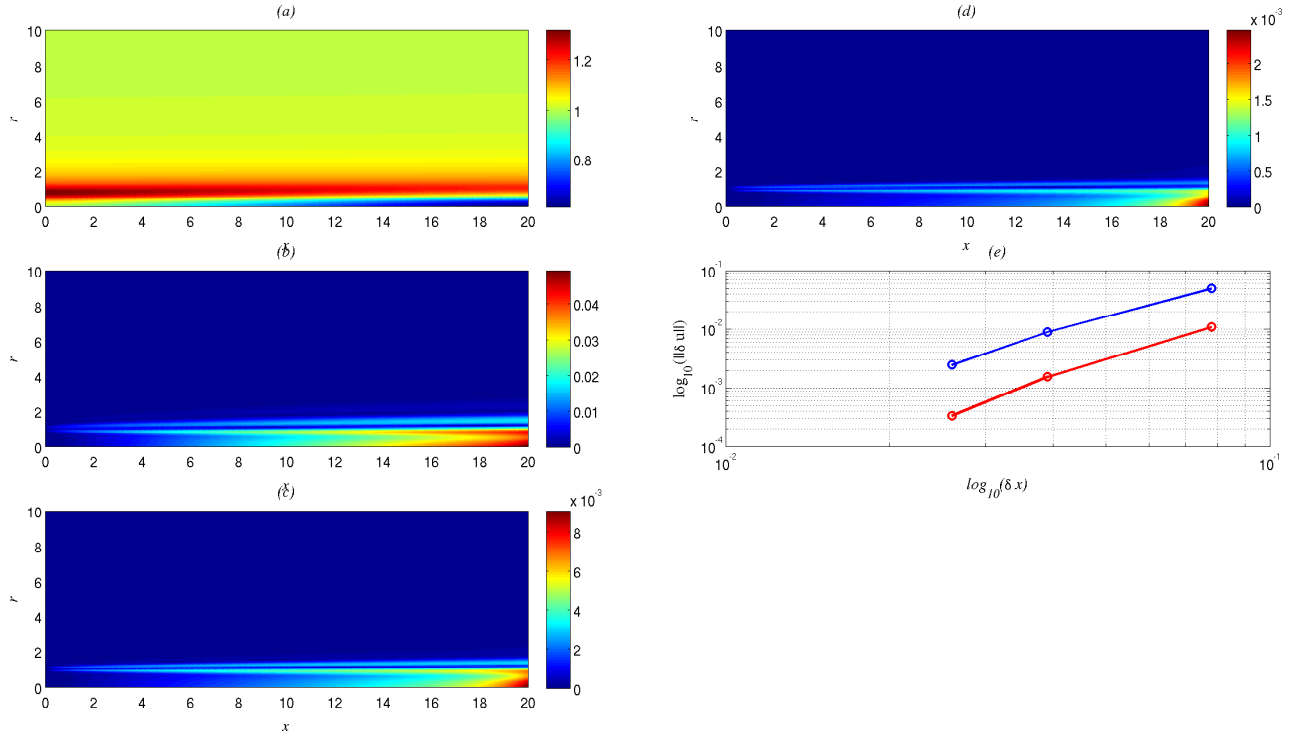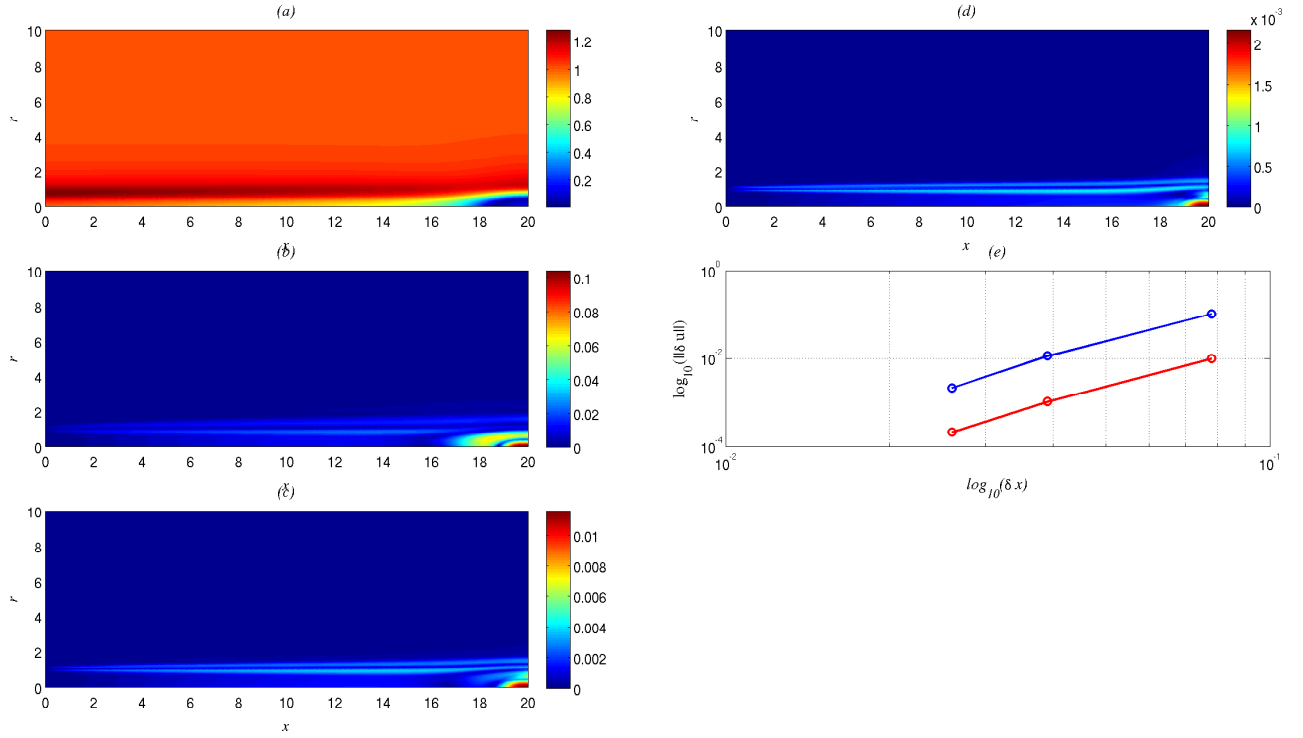
Figure 3.10: Point C: Resolution test for $S = 0.7361936$, $Re = 1000$ (unstable branch). Magnitude of the velocity for the exact solution using grid resolution N_4 (a). Point-wise magnitude of the error for lower resolutions: N_1 (b), N_2 (c) and N_3 (d). $L^\infty-$ (blue) and L^2- (red) norms of the error for various resolutions with step δx.
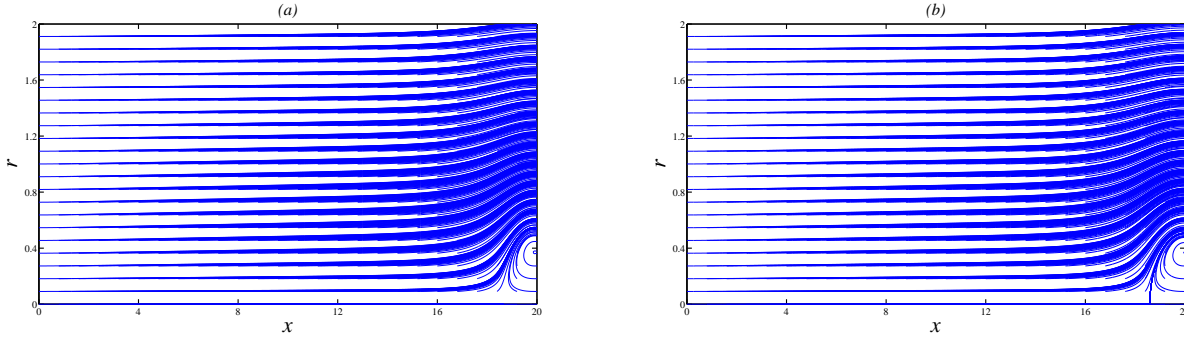
Figure 3.11: Point C: Streamline patterns for $S = 0.7361936$, $Re = 1000$ (unstable branch): plot (a) spatial resolution N_1; plot (b) spatial resolution N_4.

error is 8.5% for the resolution N_1, see plot (d) in figure 3.12. However we do not observe any significant difference in the streamline patterns between resolution N_1 and N_2. The coarsest grid N_1 is hence still sufficient to capture the spatial structure of the solution.

For $S = 0.82$, point E, the solution computed using the grid N_2 reveals considerable differences with the solution obtained using the grid N_1. In this case the topological structure is completely different: using N_1 we observe a recirculation bubble, whereas using N_2 we only find a decelerated region without any recirculation. We validate the structure of the solution obtained on the grid N_2 by recomputing it using resolution N_4. The results of this validation are shown in figure 3.13. The streamline patterns closely match each other, and the relative error is 2.3% for N_2, see plot (e) in figure 3.13. Hence, recomputing of this solution with a finer mesh N_4 demonstrates its numerical robustness. We thus conclude that the resolution N_2 is sufficient for $S = 0.82$.

It is important to note that the solution obtained with higher resolution (N_2, N_4) is completely different from the previous case (with resolution N_1). The decelerated region is located between $x = 6$ and $x = 9$ with the minimum of the velocity magnitude lying around $x = 7.5$, whereas near the saddle node bifurcation the deceleration occurs at the outlet of the computational domain. The new steady decelerated solution branch was obtained with grid N_2 by direct time integration. Hence it is a linearly stable steady solution. By increasing S up to at $S = 0.83$ this solution gradually changes from the decelerated state to a state with a recirculation bubble. We point out here that the solution at point E was never mentioned in the literature. This can be due to one of the following reasons: poor resolution used in previous investigations (e.g. this solution was not identified with the grid N_1) or complex interaction between lateral-outlet boundary conditions and the inlet Grabowski profile not investigated yet for this set of parameters ($Re = 1000$ and $S = 0.82$).

It is also important to mention here that for the same parameter $S = 0.81$ we ob-
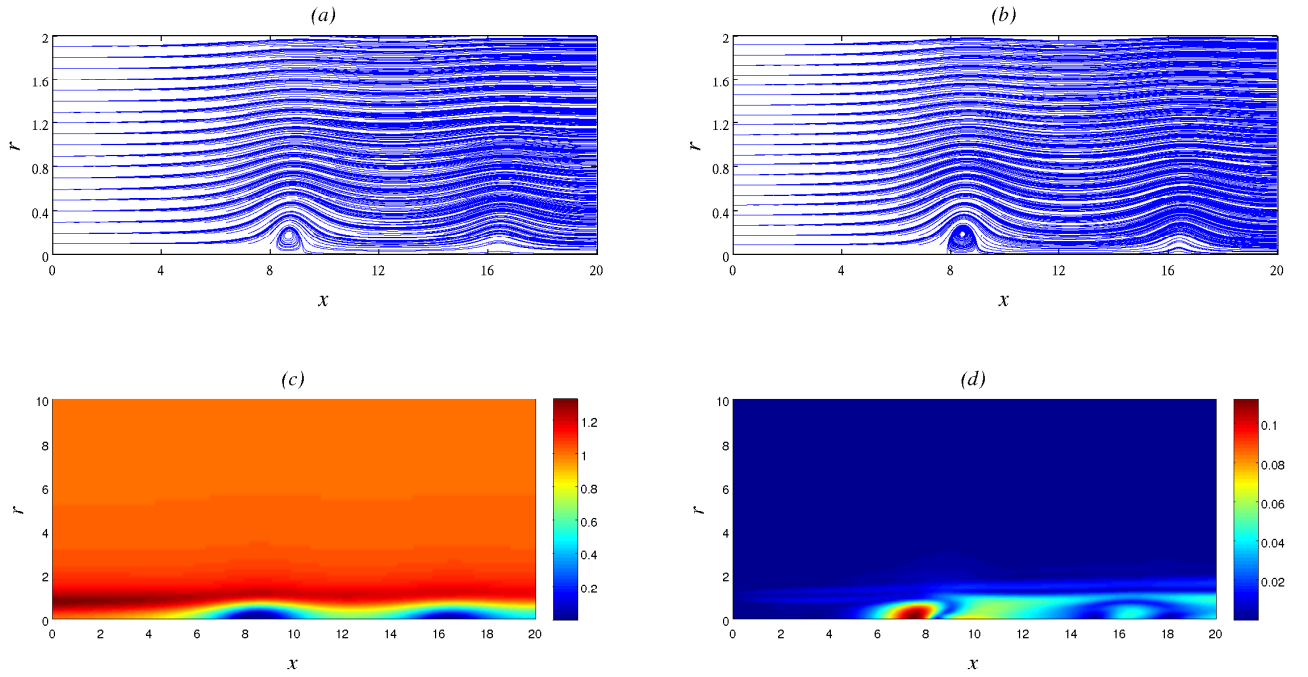
Figure 3.12: Point D: Resolution test for $S = 0.7904633$, $Re = 1000$ (stable branch). Streamline patterns: (a) spatial resolution N_1; (b) spatial resolution N_2. Magnitude of the velocity for N_2 solution (c). Error field between resolutions N_1 and N_2 (d).
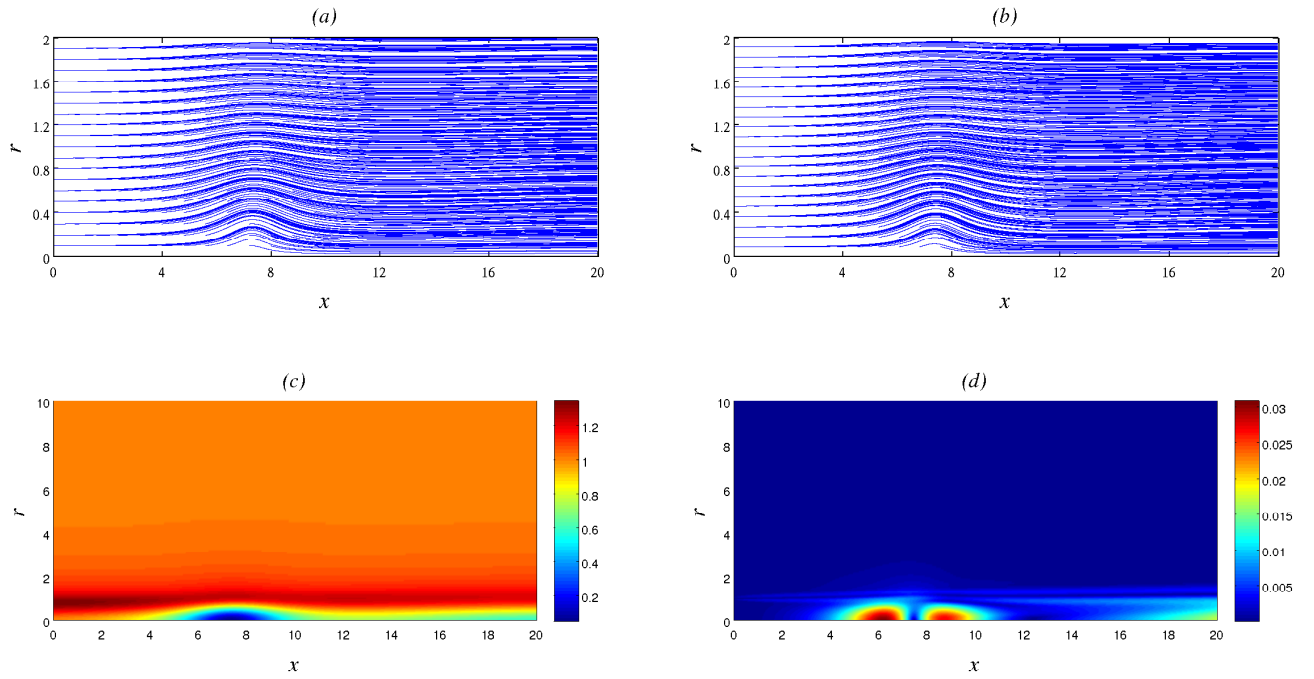
Figure 3.13: Point E: Resolution test for $S = 0.82$, $Re = 1000$ (stable branch). Streamline patterns: (a) spatial resolution N_2; (b) spatial resolution N_4. Magnitude of the velocity for the exact solution using grid resolution N_4 (c). Point-wise magnitude of the error for a lower resolution N_2 (d).

serve two different stable states: one with recirculation region (lower solution) and another without any recirculation (upper branch), see figure 3.9. This suggests the existence of a bifurcation close to this point. In any case this peculiar solution behavior calls for more careful investigation in the future.

4 Stability of Swirling Jets

This chapter contains new preliminary results on the effect of an imposed pressure gradient and on the global stability to axisymmetric and also non-axisymmetric disturbances. More precisely, the first section describes the influence of an external pressure gradient on the bifurcation diagram for axisymmetric swirling jets. In the second section the linear and nonlinear global stability of axisymmetric swirling jets are investigated with respect to axisymmetric perturbations. The global linear stability with respect to three-dimensional perturbations is also studied using an Arnoldi method for different parameter values. As in Chapter 2 and 3, validation tests confirm the necessity for high numerical resolution. The results are still incomplete since we have realized only recently the necessity for an increased numerical resolution (see sections 1 and 2).

4.1 The effect of an axial pressure gradient

4.1.1 General aspects

In several experimental studies, Sarpkaya[91, 95, 94] and Faler and Leibovich[29] have considered a weakly diverging pipe in order to investigate vortex breakdown. The convergence or divergence of the pipe induces an additional pressure gradient, which can respectively delay or promote breakdown. Exploiting this property, other more complicated pipe geometries are also used in technological fluid devices such as hydrocyclonic separators [48] and combustion chambers. [26]

The effect of a small viscosity was discussed in the Chapter 3 in the context of an incompressible axisymmetric flow without any external pressure gradient. Here and in Figure 4.1 we briefly recall the main results about the dependence on the swirl number S . It was shown that the columnar flow state becomes unstable in the inviscid limit above a particular swirl parameter S_1. An asymptotic expansion shows that for small perturbations around this inviscid state an exchange of stability gives rise to a double saddle node bifurcation: the inviscid solution branch breaks into two viscous branches with a gap between them, such that above a critical swirl number $S_{c\nu 1}$ no quasi-columnar flow exists. This theory predicts that above a critical swirl number $S_{c\nu 2}$, both an unstable branch (quasi-columnar flow) and a stable branch (accelerated state) may exist at high swirl number. These states have not been observed yet, because of a gap between $S_{c\nu 1}$ and $S_{c\nu 2}$ where only one stable solution exists, corresponding to a state with a recirculation region, see figure 4.1.

In the case of the inviscid flow in a pipe Rusak et al. [84] used an asymptotic analysis based on a small pipe divergence parameter σ. They established that the solution in a diverging pipe breaks near the critical swirl S_1 into two solution branches with a finite gap between them. In this gap, $S_{c\sigma 1} < S < S_{c\sigma 2}$, no near-columnar flow exists and the flow displays large temporal variations. Outside this region, for $S < S_{c\sigma 1}$ and for $S > S_{c\sigma 2}$, two steady solutions coexist for the same boundary conditions: one corresponds to the quasi-columnar flow, the other to a swirling flow with a solitary standing wave. The effect of $\sigma > 0$ on the bifurcation diagram bears a strong analogy with the introduction of a small viscosity ν investigated here in Chapter 3, see figure 3.1.

Switching the sign of σ directly leads to the bifurcation diagram in the case of a contracting pipe. Rusak and Meder,[86] established that the flow in a contracting pipe accelerates near the centerline so that there is no fold along the corresponding solution branch, see the bifurcation diagram figure 4.1. The convergence of the pipe induces a favorable pressure gradient in the mean flow direction. These results suggest that the addition of a small favorable axial pressure gradient can delay or even prevent vortex breakdown. In analogy with the previous paragraph, a favorable pressure gradients acts on the bifurcation diagram as a diminished viscosity.

88
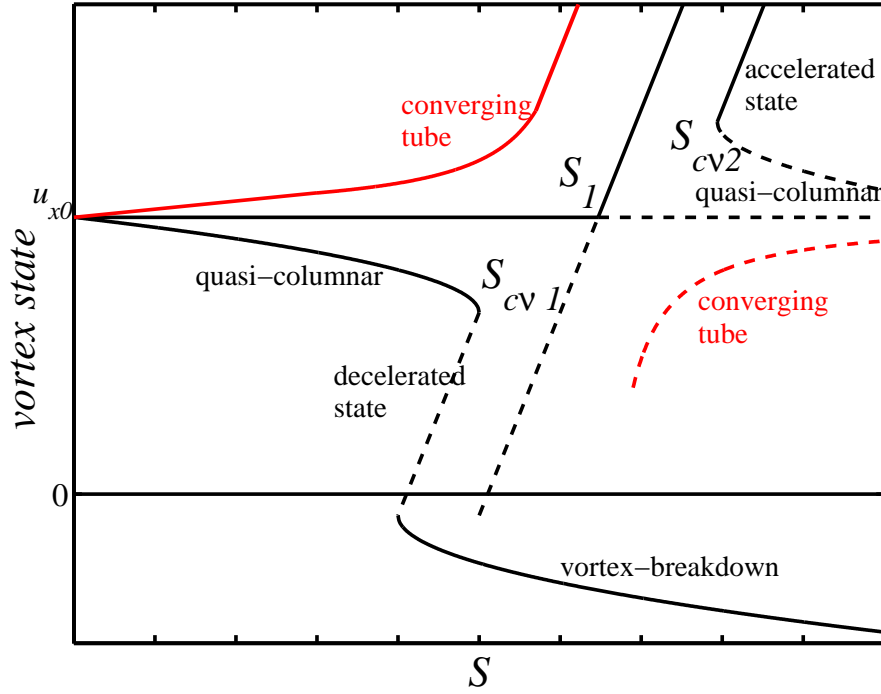
Figure 4.1: The summary of the previous theoretical work: qualitative bifurcation diagram for axisymmetric vortex breakdown for both inviscid and viscous flows (black lines) and converging tubes for inviscid flow (red lines). Solid lines correspond to stable solutions, dashed lines to unstable solutions.

4.1.2 Flow configuration and theoretical prediction

We use the same flow configuration as in the previous chapters. However, instead of modifying the geometry, we directly impose an external pressure gradient in the axial direction. The axisymmetric Navier–Stokes and continuity equations take the form:

$$\frac{\partial u_x}{\partial t} + u_x \frac{\partial u_x}{\partial x} + u_r \frac{\partial u_x}{\partial r} + \frac{\partial p}{\partial x} + \beta - \frac{1}{Re}\left(\frac{\partial^2 u_x}{\partial x^2} + \frac{\partial^2 u_x}{\partial r^2} + \frac{1}{r}\frac{\partial u_x}{\partial r}\right) = 0,$$

$$\frac{\partial u_r}{\partial t} + u_x \frac{\partial u_r}{\partial x} + u_r \frac{\partial u_r}{\partial r} - \frac{u_\theta^2}{r} + \frac{\partial p}{\partial r} - \frac{1}{Re}\left(\frac{\partial^2 u_r}{\partial x^2} + \frac{\partial^2 u_r}{\partial r^2} + \frac{1}{r}\frac{\partial u_r}{\partial r} - \frac{u_r}{r^2}\right) = 0, \quad (4.1)$$

$$\frac{\partial u_\theta}{\partial t} + u_x \frac{\partial u_\theta}{\partial x} + u_r \frac{\partial u_\theta}{\partial r} + \frac{u_r u_\theta}{r} - \frac{1}{Re}\left(\frac{\partial^2 u_\theta}{\partial x^2} + \frac{\partial^2 u_\theta}{\partial r^2} + \frac{1}{r}\frac{\partial u_\theta}{\partial r} - \frac{u_\theta}{r^2}\right) = 0,$$

$$\frac{\partial u_x}{\partial x} + \frac{1}{r}\frac{\partial}{\partial r}\left(r u_r\right) = 0,$$

where β represents the body force due to an external axial pressure gradient.

In the presence of a small viscosity and a small external pressure gradients we consider the perturbation approach about the critical inviscid solution for S_1 defined in section 3.1.4.

Wang and Rusak have shown that for small viscosity[114] and small tube divergence [84] a regular expansion in the neighborhood of the critical state is nonuniform. This motivates the introduction of another small parameter $\Delta\Omega'$ measuring the closeness to the critical inviscid state with zero external pressure gradient. We set $\Omega = S^2$, $\Omega_1 = S_1^2$. Assuming a balance at leading order when perturbing the transcritical bifurcation, we now set $\Omega = \Omega_1 + \epsilon\Delta\Omega'$, $\beta = \epsilon^2\beta'$ and $\nu = \epsilon^2\nu'$ with $\Delta\Omega' = O(1)$, $\beta' = O(1)$, $\nu' = O(1)$. We then expand the steady solution as follows:

$$
\begin{aligned}
u_x(x,r,t) &= u_{x0} + \epsilon u_{x1}(x,r) + \epsilon^2 u_{x2}(x,r) + \dots, \\
u_r(x,r) &= \epsilon u_{r1}(x,r) + \epsilon^2 u_{r2}(x,r) + \dots, \\
u_\theta(x,r) &= S u_{\theta0}(r) + \epsilon u_{\theta1}(x,r) + \epsilon^2 u_{\theta2}(x,r) + \dots, \\
p(x,r) &= p_0(r) + \epsilon p_1(x,r) + \epsilon^2 p_2(x,r) + \dots,
\end{aligned}
\tag{4.2}
$$

where $\epsilon \ll 1$. As in Chapter 3 the perturbation variables u_{x1}, u_{r1}, $u_{\theta1}$ must satisfy the following boundary conditions:

$$
u_{x1}(0,r) = 0, \quad u_{r1}(0,r) = 0, \quad u_{\theta1}(0,r) = 0,
$$

$$
\frac{\partial u_{r1}}{\partial x}(x_0,r) = 0,
$$

$$
u_{r1}(x,0) = 0, \quad \frac{\partial u_{r1}}{\partial r}(x_0,R) = 0.
$$

These same boundary conditions will also be imposed to the higher-order terms u_{x2}, u_{r2}, $u_{\theta2}$.

Substituting of(4.2) into (4.1) and collecting terms at different order of ϵ, yields the following equations:

$$
\begin{aligned}
L(\mathbf{q}_1) &= 0, \\
L(\mathbf{q}_2) &= -\mathbf{H}(\mathbf{q}_1) - \mathbf{P}(\mathbf{q}_1, u_{\theta0}) - \beta'\mathbf{K} + \nu'\mathbf{N}(u_{\theta0}),
\end{aligned}
\tag{4.3}
$$

where $\mathbf{q}_1 = (u_{x1}, u_{r1}, u_{\theta1}, p_1)^T$ and $\mathbf{q}_2 = (u_{x2}, u_{r2}, u_{\theta2}, p_2)^T$. Here L is the operator:

$$
L\mathbf{q} = \mathbf{B}\frac{\partial\mathbf{q}}{\partial x} + \mathbf{C}\frac{\partial\mathbf{q}}{\partial r} + \mathbf{D}\mathbf{q},
\tag{4.4}
$$

and the matrices are given by

$$
\mathbf{B} = \begin{pmatrix} u_{x0} & 0 & 0 & 1 \\ 0 & u_{x0} & 0 & 0 \\ 0 & 0 & u_{x0} & 0 \\ 1 & 0 & 0 & 0 \end{pmatrix}, \quad
\mathbf{C} = \begin{pmatrix} 0 & 0 & 0 & 0 \\ 0 & 0 & 0 & 1 \\ 0 & 0 & 0 & 0 \\ 0 & 1 & 0 & 0 \end{pmatrix}, \quad
\mathbf{D} = \begin{pmatrix} 0 & 0 & 0 & 0 \\ 0 & 0 & -2\dfrac{Su_{\theta0}}{r} & 0 \\ 0 & \dfrac{S}{r}\dfrac{\partial(ru_{\theta0})}{\partial r} & 0 & 0 \\ 0 & \dfrac{1}{r} & 0 & 0 \end{pmatrix};
$$

90

$$\mathbf{H} = \begin{pmatrix} u_{x1}\dfrac{\partial u_{x1}}{\partial x} + u_{r1}\dfrac{\partial u_{x1}}{\partial r} \\ u_{x1}\dfrac{\partial u_{r1}}{\partial x} + u_{r1}\dfrac{\partial u_{r1}}{\partial r} - \dfrac{u_{\theta1}^2}{r} \\ u_{x1}\dfrac{\partial u_{\theta1}}{\partial x} + \dfrac{u_{r1}}{r}\dfrac{\partial(ru_{\theta1})}{\partial r} \\ 0 \end{pmatrix}, \quad \mathbf{P} = \begin{pmatrix} 0 \\ -2\dfrac{\Delta S u_{\theta0}}{r}u_{\theta1} \\ \dfrac{\Delta S}{r}\dfrac{\partial(ru_{\theta0})}{\partial r}u_{r1} \\ 0 \end{pmatrix},$$

$$\mathbf{K} = \begin{pmatrix} 1 \\ 0 \\ 0 \\ 0 \end{pmatrix} \quad \mathbf{N} = \begin{pmatrix} 0 \\ 0 \\ S_1\dfrac{\partial}{\partial r}\left(\dfrac{1}{r}\dfrac{\partial(ru_{\theta0})}{\partial r}\right) \\ 0 \end{pmatrix}.$$

At leading order $O(\epsilon)$ we recover the linear system (3.5) with $S^2 = \Omega_1$, which can be formally written as $L\mathbf{q}_1 = 0$, with L defined by (4.4). As described in section 3.1.4 the solution of this system is

$$\mathbf{q}_1(x, r) = A\tilde{\mathbf{q}}_1(x, r),$$

with A being an arbitrary amplitude to be determined by compatibility arguments at higher order.

At second order the linearized operator L applied to $\mathbf{q}_2$ is forced by terms from the lower-order solution

$$L\mathbf{q}_2 = -A^2\mathbf{H}(\tilde{\mathbf{q}}_1) - A\mathbf{P}(\tilde{\mathbf{q}}_1, u_{\theta0}) - \beta'\mathbf{K} + \nu'\mathbf{N}(u_{\theta0}). \tag{4.5}$$

The above equation may be formally written as $L\mathbf{q}_2 = \mathbf{F}(\tilde{\mathbf{q}}_1, u_{\theta0})$. Using the compatibility condition (Fredholm alternative) to find $\mathbf{q}_2$ we need the forcing $\mathbf{F}(\tilde{\mathbf{q}}_1, u_{\theta0})$ to be orthogonal to the kernel of the adjoint $L^\dagger\mathbf{q}_1^\dagger = 0$. This condition reads $\langle\tilde{\mathbf{q}}_1^\dagger|\mathbf{F}\rangle = 0$ and results in amplitude equation

$$A^2 M_1 - A\Delta\Omega' M_2 + \nu' M_3 - \beta' M_4 = 0, \tag{4.6}$$

with coefficients

$$M_1 = -\langle\tilde{\mathbf{q}}_1^\dagger|\mathbf{H}(\tilde{\mathbf{q}}_1)\rangle, \quad M_2 = \langle\tilde{\mathbf{q}}_1^\dagger|\mathbf{P}(\tilde{\mathbf{q}}_1, u_{\theta0})\rangle, \quad M_3 = \langle\tilde{\mathbf{q}}_1^\dagger|\mathbf{K}\rangle, \quad M_4 = \langle\tilde{\mathbf{q}}_1^\dagger|\mathbf{N}(u_{\theta0})\rangle$$

where the inner product for the considered domain is given by

$$\langle\mathbf{q}'|\mathbf{q}\rangle = \int_0^{x_0}\int_0^R (\mathbf{q}')^T\mathbf{q}\,r\,dr\,dx.$$

The coefficients M_i, $i = 1, .., 4$ in (4.6) can not be computed analytically since the adjoint system does not allow separation of variables. In the case considered in Chapter 3 (in the presence of a small viscosity only), the system can be reduced to one equation for the radial velocity, and coefficients M_1, M_2 and M_3 can be found explicitly, see section 3.1.5.

If the global mode normalization is the same as in section 3.1.5 only the coefficient M_4 remains to be determined and form the work of Wang and Rusak[84] it can be concluded that $M_4 < 0$. In the present case, this coefficients has not been determined since this would require solving numerically the adjoint equations. Only qualitative feature implied by normal form (4.6) would be discussed.

Equation (4.6) is quadratic in A and admits real solutions under the condition:

$$M_2 \left| \Delta\Omega' \right| \geq 2\sqrt{M_1 \left(\nu' M_3 - \beta' M_4 \right)}. \tag{4.7}$$

If (4.7) is not satisfied, equation (4.6) has no real solutions, in which case no steady viscous solution exists near the critical point.

Close to the critical state, provided the condition (4.7) is satisfied, we obtain the solutions:

$$A = \frac{\Delta\Omega' M_2 \pm \sqrt{(\Delta\Omega')^2 M_2^2 - 4M_1 \left(\nu' M_3 - \beta' M_4 \right)}}{2M_1},$$

Multiplying (4.7) by ϵ we obtain $|\Delta\Omega| = 2\sqrt{M_1 \left(\nu' M_3 - \beta' M_4 \right)}/M_2$, which means that no solution can exist between $S_{c\nu\beta 1}$ and $S_{c\nu\beta 2}$, where:

$$S_{c\nu\beta 1}^2 = \Omega_1 - 2\frac{\sqrt{M_1 \left(\nu M_3 - \beta M_4 \right)}}{M_2},$$

$$S_{c\nu\beta 2}^2 = \Omega_1 + 2\frac{\sqrt{M_1 \left(\nu M_3 - \beta M_4 \right)}}{M_2}.$$

This implies saddle-node bifurcations of the steady axisymmetric Navier–Stokes solutions. The value $S_{c\nu\beta 1}^2$ corresponds to the first correction to the inviscid critical swirl number due to viscosity and external pressure gradient.

Neglecting all terms of higher order in ϵ, the asymptotic expansion near the critical swirl Ω_1 reads

$$u_x(x, r) = u_{x0} + \frac{\Delta\Omega M_2 \pm \sqrt{(\Delta\Omega)^2 M_2^2 - 4M_1 \left(\nu M_3 - \beta M_4 \right)}}{2M_1}(\cos(\lambda x) - 1)\frac{1}{\lambda}\frac{1}{r}\frac{\partial(r\Phi(r))}{\partial r},$$

$$u_r(x, r) = \frac{\Delta\Omega M_2 \pm \sqrt{(\Delta\Omega)^2 M_2^2 - 4M_1 \left(\nu M_3 - \beta M_4 \right)}}{2M_1}\sin(\lambda x)\Phi(r),$$

$$u_\theta(x, r) = Su_{\theta 0}(r) +$$
$$\frac{\Delta\Omega M_2 \pm \sqrt{(\Delta\Omega)^2 M_2^2 - 4M_1 \left(\nu M_3 - \beta M_4 \right)}}{2M_1}(\cos(\lambda x) - 1)\frac{S}{\lambda u_{x0}}\frac{\Phi(r)}{r}\frac{\partial(ru_{\theta 0})}{\partial r},$$

where $\lambda = \frac{\pi}{2x_0}$ and $\Psi(r)$ is the solution of the problem (3.7).

In order to understand the solution behavior near the critical point S_1 at the presence of viscosity and external pressure gradient, we took arbitrary coefficients M_i in (4.6). Figure 4.2 demonstrates a schematic characteristic solution surface in the parameter space (β, S).
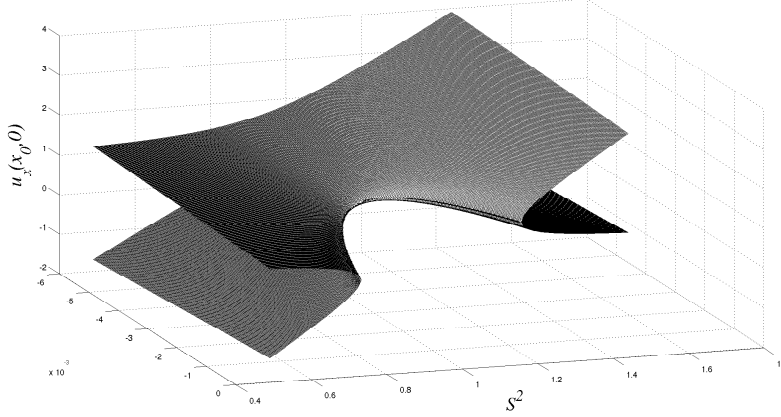
Figure 4.2: Schematic bifurcation surface as a function of the swirl number S and the imposed pressure gradient β for finite viscosity.

The bifurcation diagram in figure 4.2 shows the dependence of the axial velocity $u_x(x_0, 0)$ (evaluated at the centerline at the inlet) as a function of the governing parameters S and β. According to this solution surface there exists a critical value of the pressure gradient $\beta_c = \nu \frac{M_3}{M_4}$, at which the two viscous branches reconnect, and below which ($\beta < \beta_c$) there is no fold in the bifurcation diagram. Note that the value β_c must be negative.

For $\beta > \beta_c$ the modified transcritical bifurcation of the Euler solution consists of two Navier–Stokes branches with a finite gap between them, corresponding to two critical swirl numbers $S_{cv\beta1}$ and $S_{cv\beta2}$. The steady columnar flow exists for $S < S_{cv\beta1}$ and for $S > S_{cv\beta2}$, exactly as in the viscous case. The branches are not connected and the resulting gap near the critical swirl indicates that no near-columnar axisymmetric state exists for the corresponding range of the swirl parameter. Outside this range two near-columnar equilibrium states can exist for the same boundary conditions. For $S < S_{cv\beta1}$ one branch corresponds to a near-columnar state, the other to a decelerated axial flow which corresponds to the unstable steady-state branch. For $S > S_{cv\beta2}$ one branch consists of the accelerated state while the second relaxes towards the columnar state, see figure 4.1.

For the case $\beta < \beta_c$ a steady solution exists near the critical point. In this case the diagram results in two branches of perturbed states around S_1 along which $u_x(x_0, 0)$ increases smoothly with S: no fold in the bifurcation curve is observed. The bifurcation surface in figure 4.2 clearly shows the folded branch behavior for $\beta > \beta_c$, and unfolded behavior for

$\beta < \beta_c$.

4.1.3 Numerical procedure

We use the same computational technique, presented in the Chapter 2, for the continuation of steady solutions with respect to the parameters S (for fixed Re and β) or β (for fixed S and Re). In the current investigation we fix the Reynolds number Re to 1000.

Here we are interested in finding the second vortex breakdown-free branch (on the right top corner of the figure 4.1) at high swirl numbers $S > S_{c\nu 2}$ at $\beta = 0$. This solution branch represents two different states: one is stable and accelerated, another is unstable and possesses quasi-columnar flow structure. As already mentioned this solution branch is not reachable, due to a finite gap between solutions, the size of which is equal to $S_{c\nu 2} - S_{c\nu 1}$. The topology of the bifurcation surface in figure 4.2 suggests the following homotopy procedure to bridge the gap between both viscous solutions with $\beta = 0$: from a stable breakdown-free state with $S < S_{c\nu 1}$, we first perform a continuation with respect the β. After a sufficient axial pressure gradient is achieved ($\beta < \beta_c$), we then perform continuation along the S, with fixed β, until $S > S_{c\nu 1}$. Finally, we continue the solution along β until we cross $\beta = 0$.

Figure 4.3 frame (a) shows the feasibility of the above method for $Re = 1000$ using three different numerical grids N_1 ($N_R = 127$, $N_x = 257$), N_2 ($N_R = 253$, $N_x = 513$) and N_3 ($N_R = 379$, $N_x = 769$). We start from the solution at $\beta = 0$, $S = 0.77$ with the grid resolution N_1. Using the continuation in β with fixed S we reach the solution at $\beta = -0.01525$. We then fix β and follow the solution in S until $S = 1.2$ keeping the same spatial grid N_1. The validation of the resolution at this point showed that N_1 has become too coarse to represent well the flow structure. However, the validation of the grid N_2 ($N_R = 253$, $N_x = 513$) showed good agreement with the higher resolution N_3, see figure 4.3. For $S = 1.2$ we perform continuation in β, now using both resolutions N_1 and N_2.

Frame (b) in figure 4.3 shows the dependence of u_{xmin} (the minimum of the axial velocity) on β at $S = 1.2$. We point out that using the grid N_2, this part of the solution branch bifurcates back at $\beta = -0.01112$ and thus does not cross $\beta = 0$. The vortex breakdown-free state hence does not exist for this value of Re neither with resolution N_1 nor with N_2. We need to validate the existence of the unstable branch around $\beta = -0.01112$ for the resolution N_2 and also N_3. However, since the physics of the solution seem robust to an increase in the resolution, we expect those unstable states to persist. This would confirm the robustness of the solution with respect to the numerical resolution.

Frame (b) of figure 4.3 shows the existence of a saddle node bifurcation of the solution via continuation in β (before β reaches zero). This means that the second vortex breakdown-free branch does not exist for $Re = 1000$. The bifurcation of the solution can be explained by the fact that the value $Re = 1000$ is too small to justify the asymptotic approach for $S > S_{c\nu 2}$. It is also worth noting that the computation domain is quite long
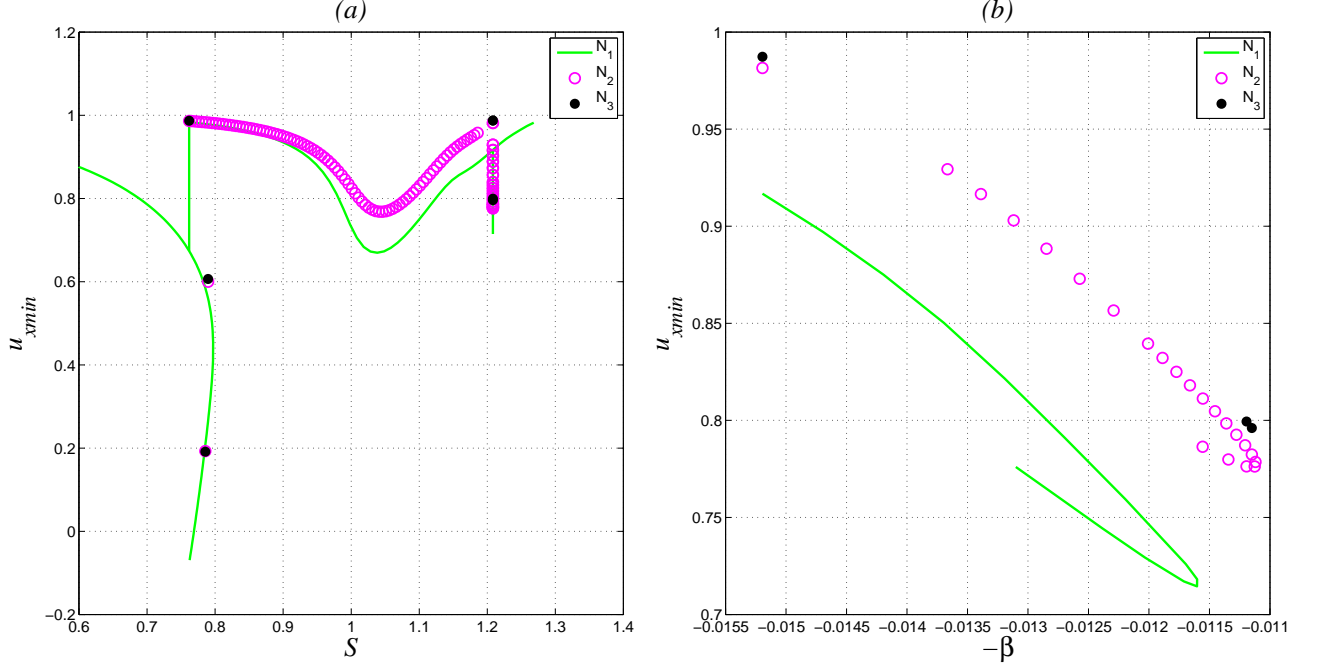
Figure 4.3: Bifurcation diagram for $Re = 1000$: on the left the minimum axial velocity u_{xmin} is plotted as a function of the swirl number S; on the right u_{xmin} is plotted as a function of the β for $S = 1.2$. According to the theoretical prediction the solutions across the gap are linked to each other through homotopy in β. Green line corresponds to grid N_1 ($N_R = 127$, $N_x = 257$), magenta circles correspond to grid N_2 ($N_R = 253$, $N_x = 513$) and black dots correspond to grid N_3 ($N_R = 379$, $N_x = 769$).

in the axial direction ($x_0 = 20$), meaning that even in the inviscid limit the eigenvalues are very densely clustered (in practice, $|S_2 - S_1| \sim 0.02$). In this situation the asymptotic expansion proposed by Rusak et al. [84] and Vyazmina et al.[108] is not valid. However, we expect to find the second vortex breakdown-free branch solutions as the Reynolds number increases. Due to the fact even for such a moderate $Re = 1000$ we need to use the grid N_2, we expect that increasing Re will require an increase in spatial resolution, which might render the computations very expensive.

The bifurcation of the solution at $\beta < 0$ was also proved by preliminary computations for $Re = 2000$ at the grid N_1. This investigation suggests very important physical characteristic of the viscous solution - the second vortex breakdown-free branch predicted by asymptotic analysis does not exist at finite (moderate) Reynolds numbers.

4.2 Hopf bifurcation

Previous theoretical studies (Benjamin,[7] Leibovich,[57] Keller,[52] Rusak and collaborators[87, 82, 111, 112, 89, 113, 88, 114, 81]) as well as numerical experiments (Beran[11], Lopez [64] and Snyder and Spall[99]) have presented a comprehensive investigation of the dynamics and stability of an incompressible axisymmetric vortex flow. Based on these investigations, Rusak and collaborators gave a clear picture of the physical mechanisms underlying axisymmetric vortex breakdown. They reported that the columnar state is absolutely stable for $S < S_0$, linearly stable for $S_0 < S < S_1$ and unstable for $S > S_1$, see Ref. [113]. The solitary wave branch connecting the states corresponding to the swirl numbers S_0 and S_1 is unstable. The breakdown branch originating from the state with swirl S_0 is globally stable for any swirl $S > S_0$ according to Wang and Rusak[113]. However, in the case of an open flow, we found that it is computationally too expensive to continue the vortex breakdown branch back towards S_0. The very slow convergence observed along this branch suggests the need for investigating the stability properties of the viscous flow (with open lateral and outflow boundaries) near the critical point S_0. Unlike previous studies inside a pipe, where the lower vortex breakdown branch is globally stable, we found that a Hopf bifurcation occurs near $S = S_0$, causing difficulties to follow numerically the steady solution branch. All the simulations in the present case are carried out for a Reynolds number of $Re = 1000$.

As in previous studies we use the minimum of the axial velocity in the entire domain, u_{xmin}, as a quantitative measure of the flow and vary the swirl parameter S. For each choice of this parameter steady-state solutions and their stability are computed using an arc-length continuation coupled with the RPM technique.

At this point it is important to give more details about the choice of the numerical resolution. We have shown in Chapter II that the grid N_1 ($N_R = 127$, $N_x = 257$) is sufficient to capture the near-columnar and solitary wave states with enough accuracy. Hence those branches shown in figure 4.4 were calculated using the resolution N_1. However, in the case at hand, the presence of a recirculation region imposes the use of an N_2 ($N_R = 253$, $N_x = 513$) grid, shown in the previous chapter to display negligible discrepancies with the exact (N_4 ($N_R = 505$, $N_x = 1025$)) solution.

Figure 4.4 shows the steady-state solution branches versus the swirl parameter S. The saddle-node bifurcation of the solution at critical swirl $S_{c\nu 1}$ is evident, as predicted by theory. [114, 108] In experiments or in simple time integrations by DNS (without stabilization), the decelerated solution in the fold (connecting points $S_{c\nu 1}$ and S_0) cannot be observed since it is unstable. The instability of the solutions in the fold actually leads to a hysteresis phenomenon: as the swirl is increased, the solution remains in the near-columnar state until S becomes larger than $S_{c\nu 1}$, at which point the solution suddenly jumps to the lower vortex breakdown branch. Conversely, it is expected that the swirl number must be lowered below S_0 for the flow to transition from the vortex breakdown state back to the near-columnar state. For vortex breakdown inside a pipe, computations [64] have shown that this reverse transition does indeed occur at $S = S_0$.
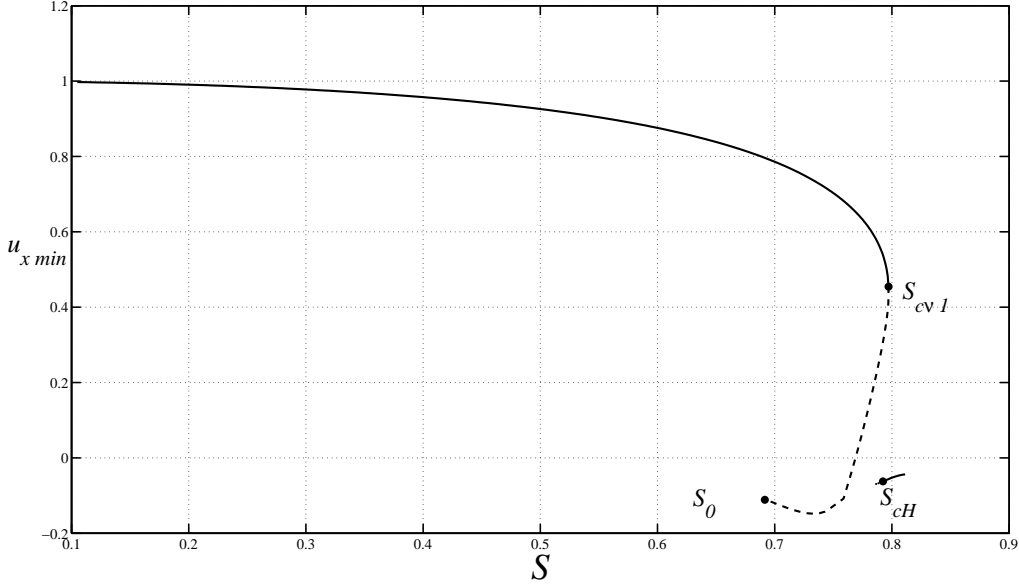
Figure 4.4: Bifurcation diagram describing the formation of vortex breakdown as the swirl is increased. The minimum axial velocity $u_{x\,min}$ is plotted as a function of the swirl number S. Each point along the bifurcation curve corresponds to a steady-state solution of the Navier-Stokes equations. The solid line corresponds to stable solutions, the dashed line to the unstable solitary wave solution, the dashed-dotted line to the limit circle behavior.

Using RPM we found that for $S < S_{cH}$ (see figure 4.4) the steady solution has two complex conjugate eigenvalues associated with a positive growth rate. This indicates that the steady solution is unstable and possibly evolves into a limit cycle. In order to determine whether such a cycle can be reached numerically, we have considered the steady solution obtained and its least stable eigenvector (both obtained using RPM) and perturbed it by (also obtained from the RPM procedure) with an amplitude 10^{-4}. Starting from this perturbed state, we have used DNS for $S > S_{cH}$ and $S < S_{cH}$, figure 4.5 frames (a) and (b), respectively. As illustrated by figure 4.5 (a), for $S > S_{cH}$ the perturbation decays back exponentially towards the original steady state. However, for $S < S_{cH}$, see figure 4.5 (b), the perturbations energy undergo an exponential growth followed by saturation, indicating that a stable limit cycle has been reached. The comparison between RPM and DNS shows that a Hopf bifurcation occurs at $S = S_{cH}$ and that it is supercritical since the eigenvalues cross the unit circle for decreasing values of S.

The same behavior was found for the coarse resolution N_1 as well. Figure 4.6 shows the growth rate associated to perturbations to the steady state. The growth rate was calculated via nonlinear DNS from the maxima of the perturbation velocity around the steady state in the linear regime, when the observed oscillations are strictly monochromatic and their envelope displays exponential growth. The green line corresponds to the resolution
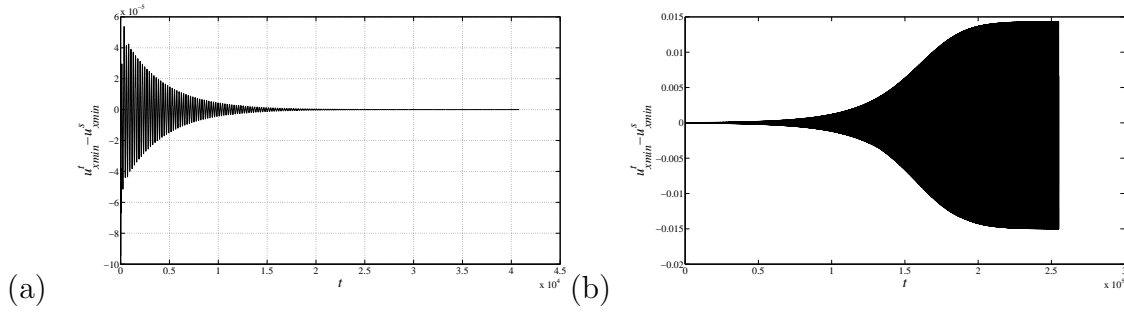
Figure 4.5: The difference between the fixed point solution and the limit cycle for swirl number (a): $S = 0.79239875578$; (b): $S = 0.7904633$. Numerical simulations were carried out for the spatial resolution N_2.

N_1 whereas the magenta line corresponds to the resolution N_2. As expected, the location of the critical S_{cH} point (associated with a vanishing growth rate) shows a weak dependence on the numerical resolution: in the case of the coarse resolution N_1 $S_{cH} = 0.784$, and for N_2 $S_{cH} = 0.791$. This yields an error estimate for S_{cH} of less than 1%, demonstrating the robustness of the physical mechanism with respect to numerical resolution. The slope extrapolated from the growth rates varies from 0.222771 for N_1 to 0.2102428, giving an error of about 6%. The same error magnitude was found in Chapter 3 between the steady state solutions computed using grids N_1 and N_2 in the same parameter range for S.

Another important physical feature of the flow is the period T of the oscillations around the unstable steady state (in the absence of period doubling). Figure 4.7 shows the dependence of T on the swirl parameter S. (T was calculated using DNS in the linear regime starting from the neighborhood of the steady state, as for the corresponding growth rate). Near the critical swirl S_{cH}, the period T increases linearly with an increase in S. The error in the slope computed with resolutions N_1 and N_2 is about 13.5%.

It is important to mention that the physical period of oscillations is rather large, meaning that the most unstable eigenmodes correspond to slow oscillations. This causes numerical difficulties for the determination of the associated subspace of the Jacobian, and this issue manifests itself by a very slow convergence of the RPM algorithm. This comes from the fact that monitoring the Picard iteration requires long time-integration. Since the velocity of the flow changes on a slow time-scale scaling with $T \approx 200$, many costly Picard iterations are needed for an estimation of the corresponding eigenspace. Experience has shown that integration for two thirds of a period T is needed to obtain a basis for the projection onto the unstable subspace. As the resolution is increased, the time step must be reduced accordingly, which adds up to the total cost of the computation.

The comparison between the growth rates and the oscillation frequencies determined by RPM and DNS shows that eigenvalues found by RPM are detected with large precision.
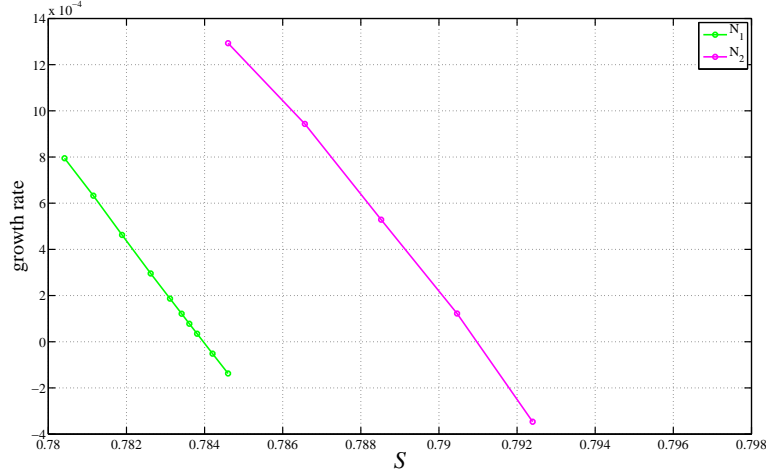
Figure 4.6: Growth rate versus swirl S, the green line corresponds to N_1 resolution, magenta line corresponds to N_2 resolution.

However this precision is good enough to claim that the solution found by RPM corresponds to the steady solution identified using DNS. Figure (a) 4.5 is the strong evidence of this fact, since it displays that the DNS solution converges towards the one obtained by RPM.

Figure 4.8 (blue color) shows the dependence of the periodic solution amplitude on the swirl number (for these computations N_1 grid was used), while frames a, b, c and d correspond to different characteristic states represented on the bifurcation diagram (on the right). We define the amplitude of the oscillations as the maximum difference between the periodic solution obtained by DNS and the steady state solution, $A = u_x^{DNS}(x_0, 0) - u_x^s(x_0, 0)$. Frame (a) in figure 4.8 represents the amplitude of the limit cycle obtained for S close to S_{cH}. Frame (b) shows the solution after it has passed one period doubling, with the appearance of another local maximum (see the second horizontal line). Frames (c) and (d) correspond to the periodic flow after two and three period doublings, respectively. In frame (c) each horizontal black line is associated with a corresponding set of local maxima. In the case of the three period-doubling the structure of the oscillations is already thin, meaning that local maxima of the amplitude are quite close to each other. For this reason, some of the lines on frame (d), corresponding to different local maxima, visually merge together. A further decrease of swirl leads to chaotic behavior associated with a Coullet–Feigenbaum cascade, partly represented in figure 4.8.

In the present case for both resolutions N_1 and N_2, the structure of the hysteresis loop is far more complex, with the disappearance of the breakdown state via a series of bifurcations leading to a complex behavior, and eventually leaving the columnar state as the only attractor as S is decreased. This leads to a jump of the periodic solution towards the columnar state for $S > S_0$ and means that hysteresis occurs at larger swirl number than predicted by theory. In another words, the state at $S = S_0$ cannot be reached by direct
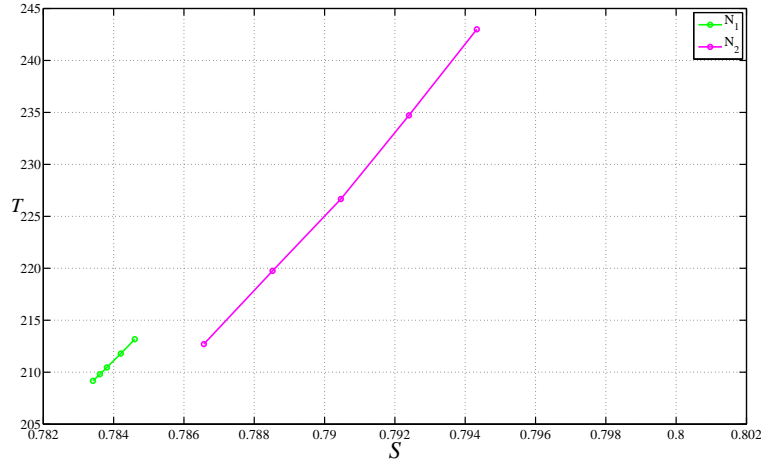
Figure 4.7: Period T of oscillations around the steady state versus swirl S, the green line corresponds to N_1 resolution, magenta line corresponds to N_2 resolution.
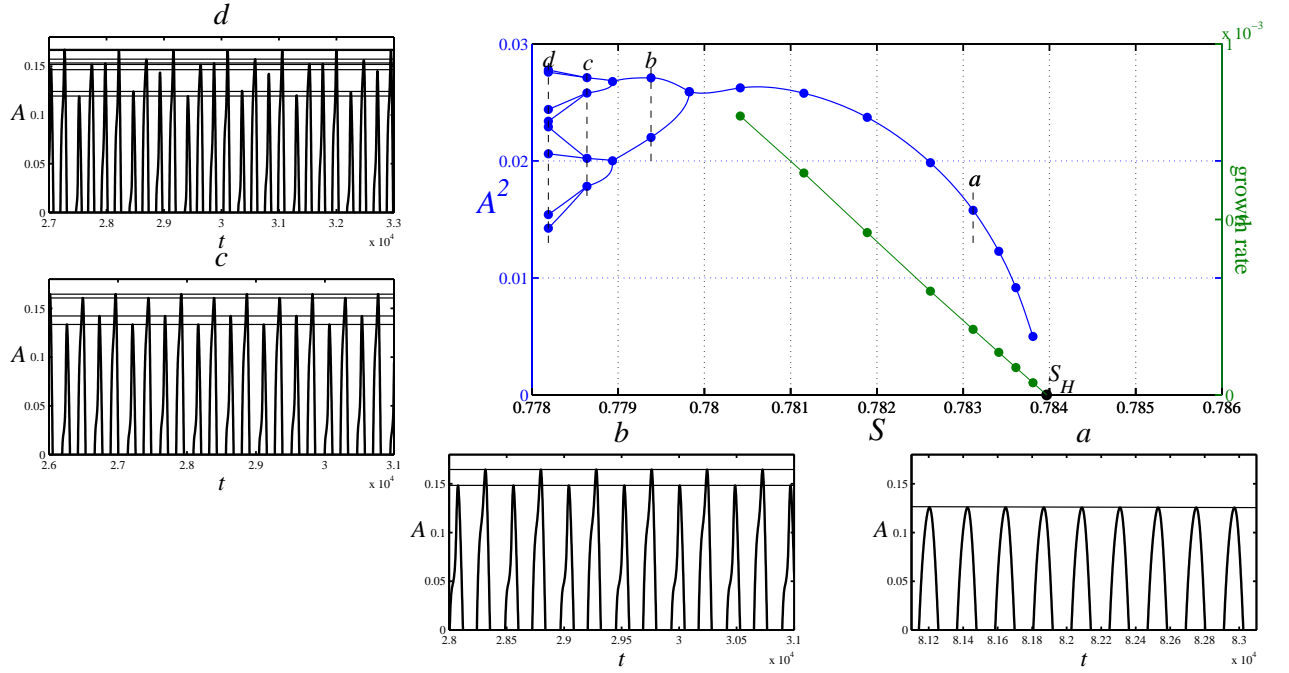
Figure 4.8: Amplitude bifurcation in the neighborhood of the S_{cH} on the right, and corresponding amplitudes on the bottom and on the left; (a): $S = 0.7831154096$; (b) $S = 0.7793802829$; (c) $S = 0.7786377016$; (d) $S = 0.7781908822$.

100

time-stepping or experimental investigation, due to the unstable nature of the solution near this point.

4.3   Spiral vortex breakdown

The goal of the present section is to determine numerically the three-dimensional global stability of the flow linearized around the axisymmetric steady state with recirculation bubble found in Chapter 2.

4.3.1   Previous studies

As mentioned in the introduction, spiral vortex breakdown has been observed experimentally by Sarpkaya,[91] Faler & Leibovich,[29] and Escudier & Zehnder.[28] Lambourne & Bryer[54] reported the coexistence of both an axisymmetric recirculation bubble and spiral vortex breakdown for the same set of parameters. Measurements of Brücker & Althaus[16] further revealed a periodic switch between the bubble and the spiral form.

Using direct numerical simulation at a moderate Reynolds number, Ruith & Meiburg[80] observed an axisymmetric bubble, then helical and double-helical breakdown modes as the swirl is progressively increased. Transition to helical breakdown modes was suggested to be caused by a sufficiently large pocket of absolute instability in the wake of the bubble, giving rise to a self-excited global mode. Gallaire & Chomaz[32] identified the selection mechanism responsible for the appearance of a double-helical structure in the pre-breakdown stage of so-called screened swirling jets, when the circulation vanishes away from the jet. Temporal and absolute/convective instability properties were extracted from numerical simulations of the linear impulse response for different swirl parameters. It was shown that a large set of negative helical modes, winding around the base flow, are destabilized as the swirl is increased, and their characteristics for large azimuthal wave numbers agreed with the asymptotic analysis of Leibovich & Stewartson.[61]

Gallaire et al.[33] demonstrated by means of numerical simulation that the non-axisymmetric vortex breakdown results from a global instability of the axisymmetric vortex breakdown state. It is triggered by the appearance of a locally absolutely unstable region in the wake of the recirculation bubble. The resulting nonlinear global mode is primarily driven by a front located where the flow goes from convectively to absolutely unstable. They drew an analogy between vortex breakdown and the flow behind a bluff body, the wake of which becomes absolutely unstable.

4.3.2   Governing equations

As before we consider that the flow is governed by the incompressible Navier-Stokes equations with constant density.

The steady base flow is assumed to have the following axisymmetric form

$$\mathbf{U} = \left(U_x(x,r), U_r(x,r), U_\theta(x,r) \right).$$

In the present work, the steady base flow is obtained as a solution of the axisymmetric Navier-Stokes equations using the boundary conditions and the numerical techniques exposed in the first Chapter of this dissertation.

The linearized Navier-Stokes equations governing small perturbations in velocity, $\mathbf{u}$, and pressure, p, to the steady base flow $\mathbf{U}$ are given by:

$$\frac{\partial \mathbf{u}}{\partial t} + \mathbf{u} \cdot \nabla \mathbf{U} + \mathbf{U} \cdot \nabla \mathbf{u} = -\nabla p + \frac{1}{Re} \nabla^2 \mathbf{u}, \tag{4.8}$$
$$\nabla \cdot \mathbf{u} = 0.$$

Since the base flow $\mathbf{U}(x, r)$ is independent of time t and azimuthal angle θ, it is natural to expand the perturbations as:

$$\mathbf{u} = \mathbf{u}(x, r)e^{im\theta - i\omega t}, \tag{4.9}$$
$$p = p(x, t)e^{im\theta - i\omega t},$$

where $m \in \mathbb{Z}$ is the azimuthal wavenumber and $\omega \in \mathbb{C}$ is the complex frequency. Substituting (4.9) into (4.8) yields

$$\mathbf{A}_m \mathbf{q} = i\omega \mathbf{B} \mathbf{q}, \tag{4.10}$$

where $q = (u_x, u_r, u_\theta, p)^T$ and the operators $\mathbf{A}_m$ and $\mathbf{B}$ are given by

$$\mathbf{A}_m = \begin{pmatrix} C_m(\bullet, \mathbf{U}) - \dfrac{1}{Re}\nabla_m^2 & \nabla_m \\ \nabla_m^T & 0 \end{pmatrix}, \quad \mathbf{B} = \begin{pmatrix} 1 & 0 \\ 0 & 0 \end{pmatrix}.$$

For the azimuthal wavenumber m, the gradient operator and the velocity gradient tensor respectively read

$$\nabla_m = \begin{pmatrix} \partial_x \\ \partial_r \\ \dfrac{im}{r} \end{pmatrix}, \quad \nabla_m \mathbf{u} = \begin{pmatrix} \partial_x u_x & \partial_r u_x & \dfrac{im}{r} u_x \\ \partial_x u_r & \partial_r u_r & \dfrac{im}{r} u_r - \dfrac{1}{r} u_\theta \\ \partial_x u_\theta & \partial_r u_\theta & \dfrac{im}{r} u_\theta - \dfrac{1}{r} u_r \end{pmatrix},$$

and $C_m(\mathbf{u}, \mathbf{U}) = \mathbf{U} \cdot \nabla_m \mathbf{u} + \mathbf{u} \cdot \nabla_0 \mathbf{U}$ is the complex advection operator.

Solving numerically the eigenvalue problem (4.10) yields the complex eigenfrequency ω. The eigenfunctions depend on both space variables x and r, which makes the computations significantly challenging.

Rather than formulating (4.10) into a large matrix equation, we solve the eigenvalue problem using direct time-stepping of the linearized Navier-Stokes equations. For the velocity perturbations we impose Dirichlet boundary conditions on the inlet and lateral boundary. At the outlet we impose the convective boundary condition similar to the axisymmetric case.

The process of integrating the linearized equations forward in time from $t = 0$ to $t = t_1$ defines a new linear operator

$$\mathbf{C} \equiv \exp\left(-\mathbf{B}^{-1}\mathbf{A}_m t_1\right).$$

The eigenvalue problem

$$\mathbf{C}\mathbf{q} = \lambda\mathbf{q}, \quad \lambda \in \mathbb{C}, \quad \mathbf{q} \in \mathbb{C}^n, \quad \mathbf{C}^{n \times n} \tag{4.11}$$

for this new operator is solved using the Arnoldi method. Hence, the (complex) frequency ω is given by

$$\omega = \frac{i \log(\lambda)}{t_1}.$$

$\sigma = \mathrm{Re}(-i\omega)$ corresponds to the growth rate and $\nu = \mathrm{Im}(-i\omega)$ to the frequency. A negative growth rate $\sigma < 0$ is associated with perturbations decaying asymptotically. If all eigenvalues are strictly negative, the steady axisymmetric state $\mathbf{U}$ is linearly stable to three-dimensional perturbations. If at least one eigenvalue in the spectrum is associated with a positive growth rate $\sigma > 0$, the corresponding perturbation grows exponentially with time and the base flow is linearly unstable.

For the computations of the global stability spectrum the 'znaupd()' routine in ARPACK software library was used, see Lehoucq et al.[56]. We use 513 grid points in the axial direction and 253 in the radial direction, the timestep was chosen to be $\delta t = 0.005$. For the eigenvalue solver we use an Arnoldi basis of size 50 and seek 25.

4.3.3 Arnoldi method used by ARPACK

The Arnoldi technique to solve the eigenvalue problem (4.11) is based on an iterative algorithm where at the kth step the system takes the following form:

$$\mathbf{C}\mathbf{V} = \mathbf{V}\mathbf{H} + \mathbf{f}\mathbf{e}_k^T, \quad \mathbf{V} \in \mathbb{C}^{n \times k}, \quad \mathbf{H} \in \mathbb{C}^{k \times k}, \quad \mathbf{f} \in \mathbb{C}^{n \times 1},$$

In this expression, $\mathbf{V} = [\mathbf{v}_1, \mathbf{v}_2, \ldots, \mathbf{v}_k]$ represents a k-dimensional orthonormal basis, $\mathbf{H}$ denotes an upper Hessenberg matrix of size $k \times k$, $\mathbf{f} = h_{k+1}\mathbf{v}_{k+1}$ is the residual vector orthogonal to the basis $\mathbf{V}$ and $\mathbf{e}_k$ is a unit vector along the k-th direction. For small values of h_{k+1}, the eigenvalues θ_j, $j = 1, .., k$ of $\mathbf{H}$, the so-called Ritz values, approximate well some of the eigenvalues λ_j, $j = 1, .., k$ of $\mathbf{C}$, and the associate eigenvectors $\mathbf{q}_j$, $j = 1, .., k$ of $\mathbf{C}$ are $\mathbf{q}_j = \mathbf{V}\mathbf{y}_j$, the so-called Ritz vectors. The accuracy of the approximation is measured by

$$||\mathbf{C}\mathbf{q}_j - \mathbf{q}_j\theta_j|| = ||\mathbf{C}\mathbf{V}\mathbf{y}_j - \mathbf{V}\mathbf{y}_j\theta_j|| = ||(\mathbf{C}\mathbf{V} - \mathbf{V}\theta_j)\mathbf{y}_j|| = ||\mathbf{f}\mathbf{e}_k^T\mathbf{y}_j|| = \beta|\mathbf{e}_k^T\mathbf{y}_j|$$

with $\beta = ||\mathbf{f}||$. The central idea behind the Arnoldi factorization is to construct eigenpairs of the large matrix $\mathbf{C}$ from the eigenpairs of a smaller matrix $\mathbf{H}$. We assume that $k \ll n$ so that the eigenpairs of $\mathbf{H}$ can be computed using familiar direct techniques. The goal

is to drive $|\mathbf{e}_k^T \mathbf{y}_j| \to 0$, so that the Ritz pair $(\mathbf{q}, \theta)$ converges towards an eigenpair of $\mathbf{C}$. The term $\beta |\mathbf{e}_k^T \mathbf{y}_j|$ is called the Ritz estimate of the pair $(\mathbf{q}, \theta)$, and is a measure of the convergence of the scheme.

The orthonormal basis $\mathbf{V}$ is constructed by an orthogonalization of the Krylov space spanned by $\mathbf{C}$-iterates of an initial vector $\mathbf{v}_1$:

$$K_k(\mathbf{C}, \mathbf{v}_1) = \{\mathbf{v}_1, \mathbf{C}\mathbf{v}_1, \mathbf{C}^2\mathbf{v}_1, \ldots, \mathbf{C}^{k-1}\mathbf{v}_1\}.$$

The Arnoldi factorization is entirely dependent on the choice of the vector $\mathbf{v}_1$. In general we wish the starting vector $\mathbf{v}_1$ used to begin the Arnoldi factorization to be 'rich' in the subspace spanned by the desired eigenvectors, and with negligible components in the directions of the other eigenvectors. The idea is to adaptively refine $\mathbf{v}_1$ as a linear combination of the approximate eigenvectors, and to restart the Arnoldi factorization with this new vector instead. A convenient and stable way to perform this update is given by the implicitly restarted Arnoldi method based on the implicitly shifted QR factorization.

The idea of the restarted method is to extend a k-step Arnoldi factorization

$$\mathbf{C}\mathbf{V}_k = \mathbf{V}_k\mathbf{H}_k + \mathbf{f}_k\mathbf{e}_k^T$$

to a $(k+p)$-step Arnoldi factorization

$$\mathbf{C}\mathbf{V}_{k+p} = \mathbf{V}_{k+p}\mathbf{H}_{k+p} + \mathbf{f}_{k+p}\mathbf{e}_{k+p}^T$$

Then p implicit shifts are applied to the factorization, resulting in the new factorization

$$\mathbf{C}\mathbf{V}_+ = \mathbf{V}_+\mathbf{H}_+ + \mathbf{f}_{k+p}\mathbf{e}_{k+p}^T\mathbf{Q},$$

where $\mathbf{V}_+ = \mathbf{V}_{k+p}\mathbf{Q}$, $\mathbf{H}_+ = \mathbf{Q}^H\mathbf{H}_{k+p}\mathbf{Q}$ and $\mathbf{Q} = \mathbf{Q}_1\mathbf{Q}_2\ldots\mathbf{Q}_p$, where each $\mathbf{Q}_i$ is associated with the factorization $(\mathbf{H} - \sigma_i\mathbf{I}) = \mathbf{Q}_i\mathbf{R}_i$. Because of the Hessenberg structure of the matrices, it turns out that the first $k-1$ entries of $\mathbf{e}_{k+p}\mathbf{Q}$ are zero, so that the new k-step Arnoldi factorization can be obtained by equating the first columns on each side:

$$\mathbf{C}\mathbf{V}_k^+ = \mathbf{V}_k^+\mathbf{H}_k^+ + \mathbf{f}_k^+\mathbf{e}_k^T.$$

We can iterate the process of extending this new k-step factorization to a $(k+p)$-step factorization, applying shifts and condensing. Every iteration implicitly applies a pth degree polynomial in $\mathbf{C}$ to the initial vector $\mathbf{v}_1$. The roots of the polynomial are the p shifts that were applied to the factorization. Therefore, if we choose as a shift σ_i eigenvalues that are 'unwanted', we can effectively filter the starting vector so that it is 'rich' in the direction of the 'wanted' eigenvectors. For example, if we are interested in computing the eigenvalue with the largest magnitude, the eigenvalues of $\mathbf{H}_{k+p}$ are sorted with respect to magnitude and the p eigenvalues of smallest amplitude are used as shift.

For the results shown in the next section, we used the convergence criterion for the Arnoldi algorithm $\beta = 10^{-5}$, which is usually reached using a Krylov space of dimension
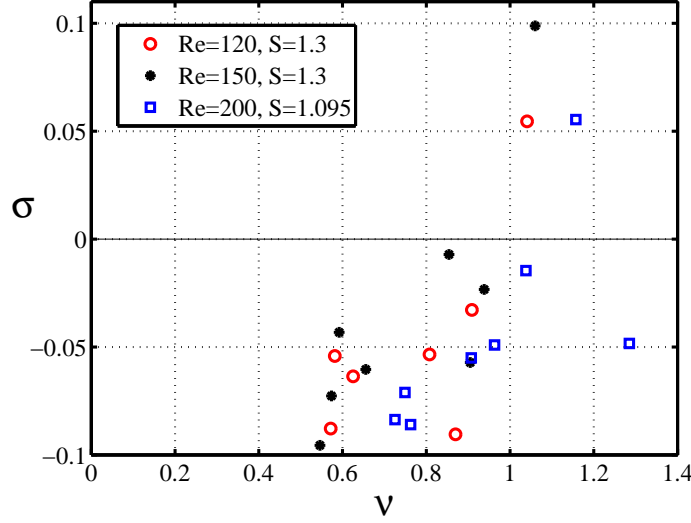
Figure 4.9: Zoom of the global Arnoldi spectrum for three different cases: ($Re = 120$, $S = 1.2$), ($Re = 150, S = 1.3$) and ($Re = 200$, $S = 1.095$).

50. In the case where only one eigenvalue is unstable, the growth rates were cross-validated by using the linearized Navier-Stokes time-stepper with the initial condition corresponding to the base flow plus the unstable eigenvector (with amplitude 10^{-8}). Extrapolation of the growth rate of the perturbation energy has confirmed quantitatively the growth rate given by the unstable eigenvalue as computed by the Arnoldi routine (within a relative error of less than 1%).

4.3.4   Results

The eigenspectrum was computed for $Re = 200$ with varying swirl S from 0.8 to 1.3, and for $S = 1.3$ from $Re = 85$ to 200. In all these cases, the flow is linearly stable to axisymmetric disturbances. The non-axisymmetric eigenspectrum was computed using the Arnoldi algorithm for perturbations with an azimuthal wavenumber $m = -1$, i.e. helical perturbations. Preliminary computations of global modes with $m = -2$ indicate that the growth is still dominated by $m = -1$ modes (at least for the range of parameters tested here). The number of unstable eigenmodes ($m = 1$) was either 0 or 1, see for instance figure 4.9. Typically, the base flow (which depends on both Re and S) is unstable for higher values of Re and/or S.

Figure 4.10 represents the effect of the swirl parameter S on the growth rate σ for the azimuthal mode $m = -1$ at $Re = 200$. The blue line corresponds to the computations carried out in the current investigation, while the red line corresponds to the reference case presented by Ruith et al.[79] In the case of Ruith et al.[79] for the lowest swirl parameter considered, $S = 0.8944$, no growing helical disturbances are found and the imposed three-dimensional disturbances decay exponentially to zero. Hence the breakdown remains
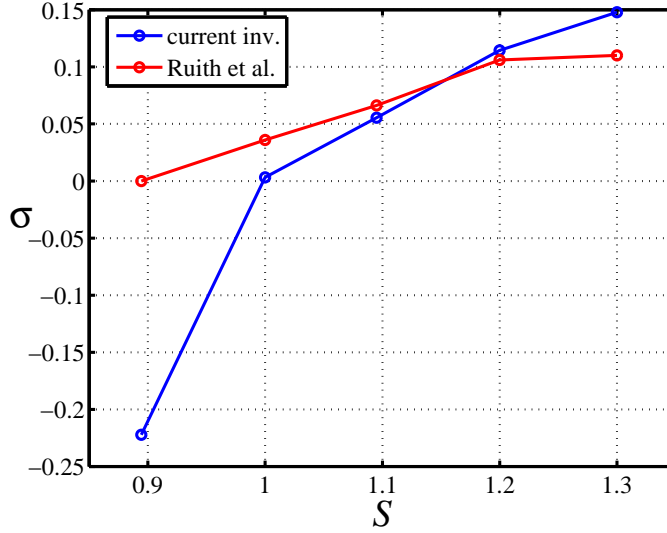
Figure 4.10: Growth rates σ versus swirl parameter S for Re=200. Comparison with Ruith et al.[79]

axisymmetric, a result confirmed in the current investigation by the absence of unstable eigenvalues. Starting from $S = 1.0$ our computations always indicate a small exponential growth, and in the range $1.1 < S < 1.2$ values of σ match closely the growth rates obtained by Ruith. For $S = 1.3$ we observe a larger discrepancy in σ, possible explained by the coarser grid used by Ruith, and by the fact that robust computing of the eigenvectors demands higher resolution. In this case, $S = 1.3$ and $Re = 200$, the base flow was not correctly resolved by Ruith (see chapter 1 for higher values of Re), and the effect of the numerical viscosity manifests itself by a lowered growth rate of the disturbances. It is worth nothing that in the study of Ruith et al.[79], the growth rate was found from nonlinear direct numerical simulations of breakdown, initiated by the axisymmetric base state with an initial perturbation of amplitude $O(10^{-10})$. Hence for $S = 0.8944$ Ruith et al.[79] did not compute the exact growth rate of the perturbations, they only indicated that the base flow is stable and remains axisymmetric. This justifies the large discrepancy obtained in the figure for $S = 0.8944$.

Figure 4.11 shows the effect of the Reynolds number Re on the growth rate σ for $S = 1.3$, still for modes with $m = -1$. For low Reynolds numbers $Re < 90$, the base flow is linearly stable. For $Re > 90$, the flow becomes linearly unstable to helical modes. Increasing Re up to $Re = 160$ shows reasonable agreement in σ between our computations and results of Ruith et al.[79] For the last point $Re = 200$, we note that the growth rate of Ruith again is lower than ours, which as in the previous paragraph can be attributed to their coarse resolution.

We show the spatial location of the perturbation energy associated to the unstable global mode with $m = 1$ in the unstable regime when there is a good match between our
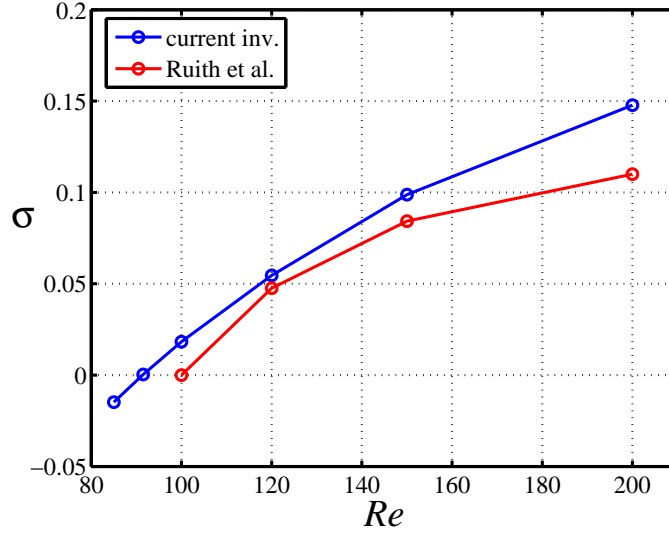
Figure 4.11: Growth rates σ versus Reynolds numbers Re for swirl parameter $S = 1.3$. Comparison with Ruith et al.[79]

results and those of Ruith et al.[79], here for $Re = 200$ and $S > 1.1$. Figure 4.12 shows the energy of the unstable mode for $S = 1.095$ and $Re = 200$. The associated perturbation energy is located predominantly at $4 < x < 16$, i.e. slightly downstream of the recirculation bubble of the base flow. By examining carefully the base flow we observe that the stream-lines reapproach to the centerline just downstream of the bubble but then separates again slightly downstream, inducing a decelerated region (wake) behind the bubble. The maximum perturbation energy lies between $x = 8$ and $x = 10$, where a last increase in the axial velocity is observed (the change from wake to jet). We thus conclude that the sightly decelerated region behind the recirculation bubble (the wake) is the most unstable to three-dimensional perturbations.

For higher swirl ($S = 1.3$), this wake region turns into a second recirculation bubble, even for the lowest values of Re, see figure 4.13. The maximum energy of the unstable global mode is located just downstream of this second recirculation bubble (e.g. from $x = 6$ to $x = 10$ for $Re = 120$), exactly where the recirculation region closes and the flow returns to the parallel columnar structure. For larger Re, i.e. $Re = 150$ the second recirculation bubble is much stronger and larger in both the axial and the radial direction. The localization of the energy of the global mode changed only slightly. However, the maximum of the energy corresponds now to the region of trailing edge of the second recirculation bubble.

Figure 4.14 shows the velocity field associated with the unstable global mode. Since all components are mostly downstream of the second recirculation bubble, this also confirms that the flow is the most unstable to three-dimensional disturbances in the region precisely where the flow exhibits a topological change from the decelerated state (or a state with recirculation) to the parallel columnar structure. The isosurface of the axial velocity com-

108
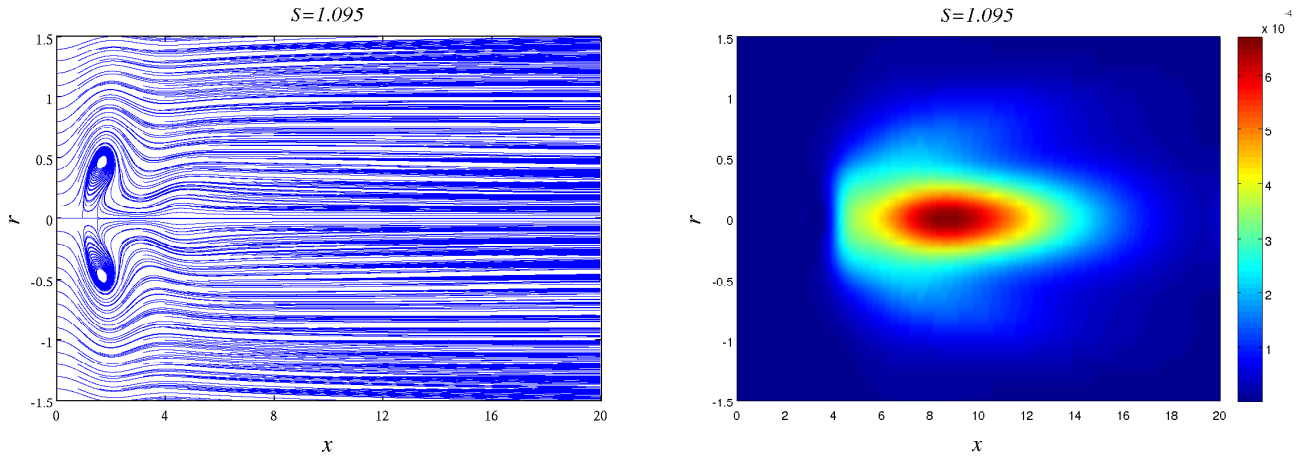
Figure 4.12: Streamlines of the base flow (on the left) and the energy of the unstable global mode (on the right) for $S = 1.095$ and $Re = 200$.
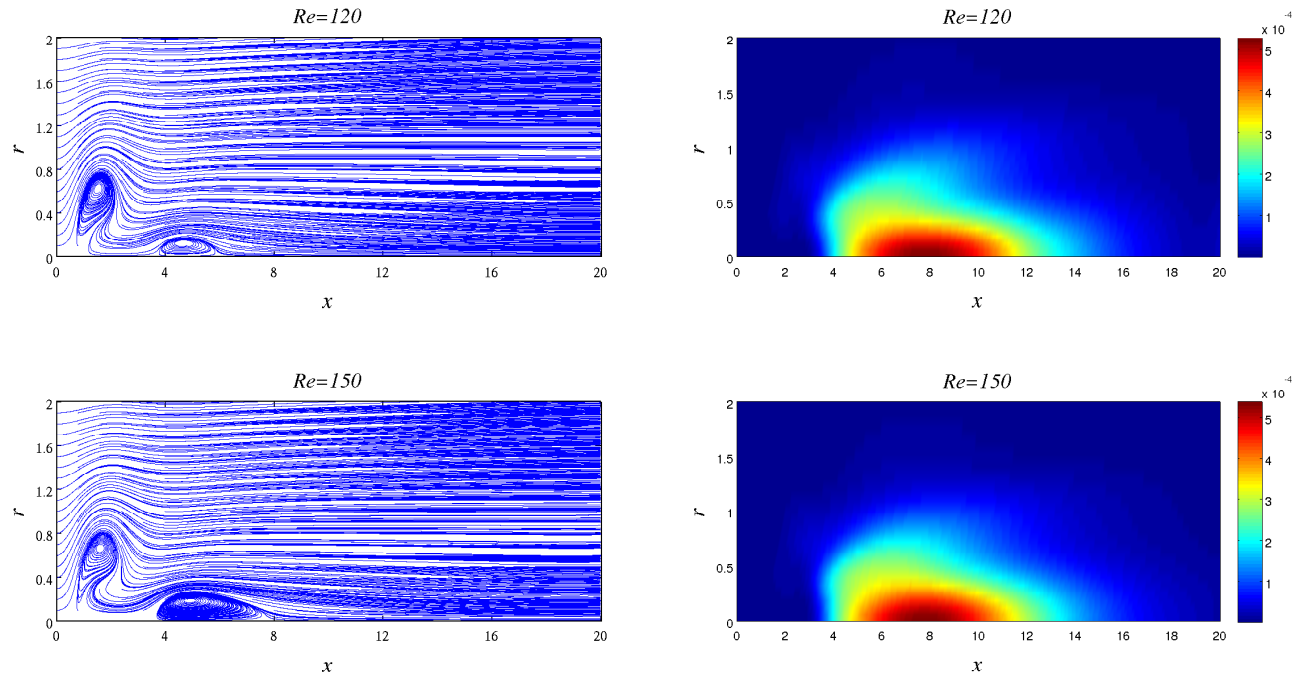
Figure 4.13: Streamlines of the base flow (on the left) and the energy of the unstable global modes (on the right) for different Reynolds numbers Re at $S = 1.3$.
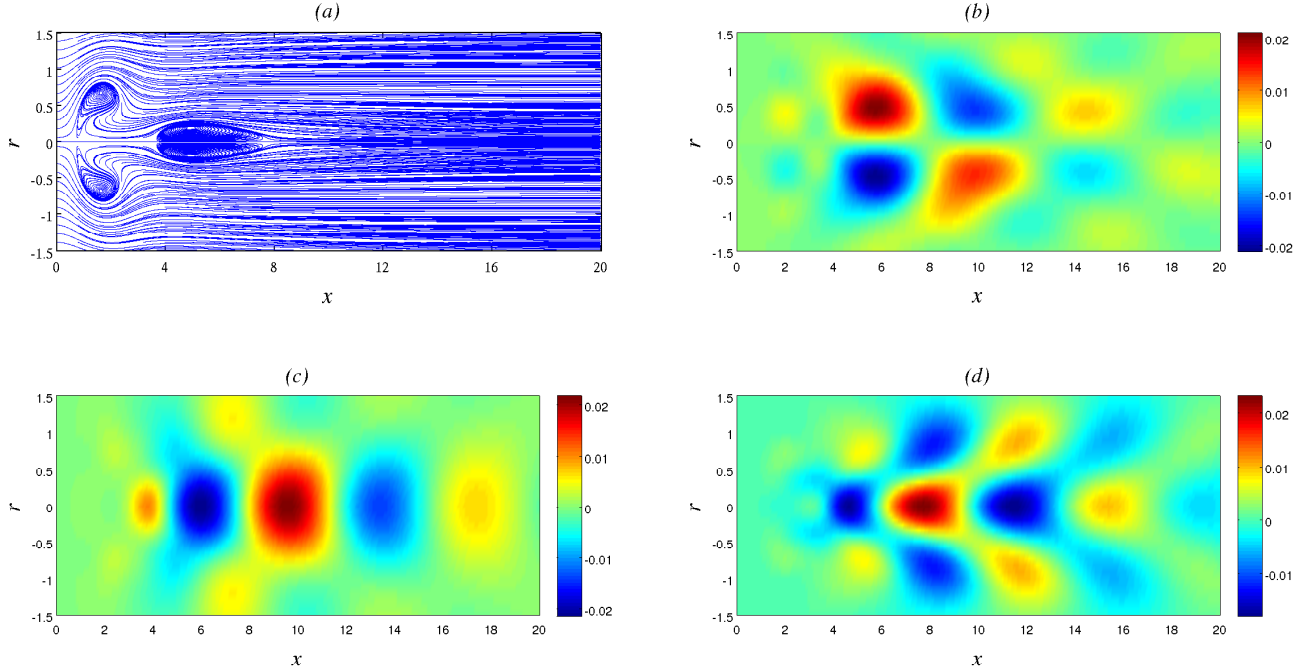
Figure 4.14: Streamlines of the base flow (a) at $Re = 150$ and $S = 1.3$ and unstable global mode: (b) $Re(u_x(x,r))$; (c) $Re(u_r(x,r))$ and (d) $Re(u_\theta(x,r))$.

ponent (see figure 4.15) demonstrates the spiral form of the unstable global mode, which suggests that this unstable global mode is associated with the spiral vortex breakdown.

At the end of this section we would like to extend the analogy of Gallaire et al.[33] between the global instability of the wake past a bluff body and vortex breakdown. Our computations of the unstable global modes strongly suggest that the instability of the axisymmetric vortex breakdown state to three-dimensional perturbations occurs where the flow undergoes a spatial change from decelerated (wake) and recirculation (bubble) behavior to the parallel columnar state. This conclusion needs to be confirmed by a sensitivity analysis, for example, used by Meliga et al.[69], using knowledge of direct and adjoint global modes. The overlap of direct and adjoint global modes detects the region of the flow, which is the most sensible to perturbations.
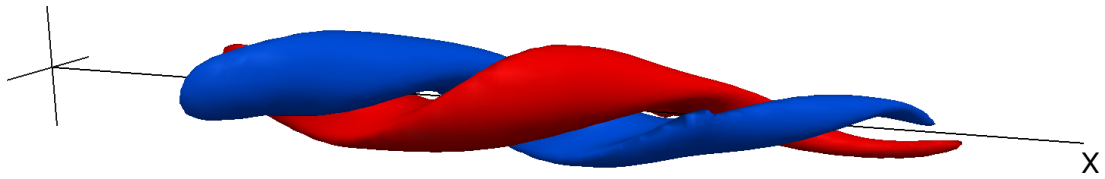
Figure 4.15: Typical isosurface of the axial velocity of the unstable global mode at $Re = 150$ and $S = 1.3$.

5 Conclusions and outlook

5.1 Conclusion

In this dissertation we have investigated numerically the stability properties of a swirling jet, by assuming open lateral and outlet boundaries. In order to accomplish this task, a numerical code written by J. Nichols[72] in the three-demential configuration, initially written for reactive flows, was adapted to the current case. The numerical arc-length continuation algorithm used the recursive projection method (RPM) was implemented in the code in order to identify steady solutions, whether stable or unstable. Their stability to axisymmetric disturbances was investigated by computing the eigenvalues of the associated Jacobian matrix. Continuation of steady solutions versus the swirl parameter S revealed the existence of bifurcations for high Reynolds numbers.

Validation of the spatial numerical resolution revealed that flow states at high S and Re can be numerically well-resolved only using a sufficiently refined grid. We showed that the 'reference case' by Ruith et al.[79] is under-resolved, which explains the discrepancies obtained between the current investigation and the reference case for the solutions at $Re = 500$.

The influence of a small but finite viscosity on the bifurcation diagram of an axisymmetric swirling Euler flow was addressed by means of numerical simulations and theoretical analysis. It was shown that in a neighborhood of critical swirling number S_1 small but finite viscosity causes the steady Euler solution to give rise to two steady Navier-Stokes solutions with a finite gap between the two branches. A small-disturbance analysis revealed a dependence on both viscosity as well as on the departure from the critical swirl S_1. It showed the existence of two critical viscous thresholds in parameter space $S_{c\nu1}$ and $S_{c\nu2}$, such that $S_{c\nu1} < S_1 < S_{c\nu2}$, with the size of the gap proportional to $\sqrt{\nu x_0 S_1}$, where x_0 is the axial size of considered domain. No quasi-columnar state exists for $S_{c\nu1} < S < S_{c\nu2}$. Outside this parameter range, however, up to three equilibrium states (quasi-columnar, decelerated or accelerated, and vortex breakdown) exist for identical boundary conditions and sufficiently large Re. In such a case, the decelerated state represents an unstable steady state and lies between the columnar and the state with recirculation, both of which are stable. The suggested asymptotic analysis displays good agreement with numerical results. Since we verified that the theoretical analysis agrees well with the numerical simulations, we used this asymptotic analysis as a tool to explore the effects of different lateral and outlet boundaries conditions on the bifurcation structure of the solution. The theoretical investigations showed that the flow near the critical swirl is more sensitive to the outlet boundary conditions than to the lateral ones.

According to theoretical predictions, in the application of an external negative pressure gradient β can delay or even prevent vortex breakdown by connecting together two branches of solutions. For pressure gradients below a critical threshold $\beta_c(\nu)$ the gap between viscous solution branches completely disappears. This bifurcation structure is verified by numerical simulations at $Re = 1000$, where the steady solutions of the Navier-Stokes equations were computed using the continuation technique. For larger pressure gradients, numerical computations show that only a single equilibrium solution exists, corresponding to a flow state without vortex breakdown. However, at higher $S > S_{c\nu 2}$ continuation with respect to β reveals a fold of the solution branch before $\beta = 0$ is reached, implying that the second solution branch does not exist for $\beta = 0$ at the moderate values $Re = 1000$ and $S > S_{c\nu 2}$.

The bifurcation structure of a viscous incompressible axisymmetric rotating flow with a recirculation bubble was studied near the critical swirl S_{cH} at $Re = 1000$, using nonlinear simulations and the RPM algorithm. It was previously believed that the vortex break-down branch is stable for any swirl larger than the critical value $S = S_0$. Our numerical simulations show, however, that as the swirl is decreased towards S_0 in the vortex break-down regime, the solution becomes unstable through a supercritical Hopf bifurcation, and evolves towards a periodic solution. A further decrease in swirl leads to period doubling and eventually to strong chaotic behavior via a Coullet-Feigenbaum cascade. This suggests that hysteresis occurs at larger swirl number than predicted by theory of Keller.

Finally, the physical origin of spiral vortex breakdown was investigated by computing the direct three-dimensional global modes with specified azimuthal wave-number $m = 1$ of the Navier-Stokes equations linearized around an axisymmetric vortex breakdown state with a recirculation bubble. The results reveal discrepancies at high S and Re with the reference case[79], observed as well for the axisymmetric base flow. As showed in Chapter 1, the resolution used in the literature is too low for high S and Re, allowing only for a qualitative correspondence. The largest eigenvalues of the global spectrum, obtained by the Implicitly Restarted Arnoldi method, is the key tool for understanding the global stability of the flow. The energy associated to the most unstable global mode is localized just downstream of the recirculation bubble, where the flow returns to the parallel columnar structure. This suggests that the instability of the axisymmetric vortex breakdown state to three-dimensional perturbations occurs where the flow undergoes a topological change from decelerated (wake) and recirculation (bubble) behavior to the parallel columnar state.

5.2 Outlook

The studies presented in this dissertation give rise following scientific perspectives:

- perform computations at higher Reynolds numbers ($Re \approx 100000$) with high spatial resolution using the procedure proposed in the first section of Chapter 4 in order to find the second vortex breakdown-free state at $S > S_{c\nu 2}$

- develop an asymptotic analysis using two competitive small parameters such as viscosity ν and axial pressure gradient β in order to investigate the solution structure and its stability properties, determining the adjoint mode numerically

- further investigation of the Hopf bifurcation and the related period doublings in the axisymmetric case, identified here for the first time (for example, using other types of boundary conditions)

- the Hopf bifurcation found at $Re = 1000$ and $S_{cH} = 0.791$ suggests to develop a continuation tool with respect to two parameters S and Re and to investigate the dependence of the critical swirl S_{cH} on the Re. Codimension two bifurcations such as a Bogdanov-Takens scenario can be expected here. In the neighborhood of this point complex dynamics of the system occurs with the appearance and collision of nontrivial solution branches (stable and unstable).

- compute the three-dimensional global modes of the *adjoint* Navier-Stokes equations linearized around the axisymmetric vortex breakdown state. The overlap between direct and corresponding adjoint mode allow to determinate whether the wake of the recirculation region or the recirculation region itself causes the spiral vortex breakdown.

6 Appendix: The pseudo-arclength continuation algorithm based on the Recursive Projection Method (RPM)

In this part of the thesis we present a numerical example in which the pseudo-arclength RPM continuation algorithm (page 47) is used to compute the stable and unstable steady-state solution branches. This example is inspired by the original paper by Schroff and Keller [97]

6.1 Bratu-Gelfand equation

We consider the Brat-Gelfand equation, which is a one-dimensional stationary problem appearing in the field of combustion (see [49] for a review of the problem):

$$f(u, \lambda) = \frac{\partial^2 u}{\partial x^2} + \lambda e^u, \quad u(0) = u(1) = 0. \tag{6.1}$$

The operator is discretized on a spatial grid of $N = 40$ points, and we introduce the associated (time-dependent) system of ordinary differential equations:

$$\frac{\partial u}{\partial t} = f(u, \lambda). \tag{6.2}$$

The temporal integration scheme generates a sequence $(u^n)_{n=0,1,2,\dots}$ which writes symbolically:

$$u^{n+1} = F(u^n), \tag{6.3}$$

whose fixed points represent solutions of the steady problem (6.1). The sequence (6.3) is integrated using the second-third order Runge-Kutta Matlab integrator over the time interval $[0 : 0.1]$. The step size for the time integration is controlled by the Matlab function $ode23$, using an error tolerance 10^{-5}.

We use the following set of parameters: the arclength step for the continuation is $\Delta s = 0.15$; the size of the disk K_δ is $\delta = 0.5$; and the relative tolerance indication the convergence of the code towards the steady state is $tol = 10^{-4}$. The Jacobian in (2.26) and the derivative F_λ in (2.36) are computed using first-order finite differences with $\epsilon_i = 10^{-3}$.
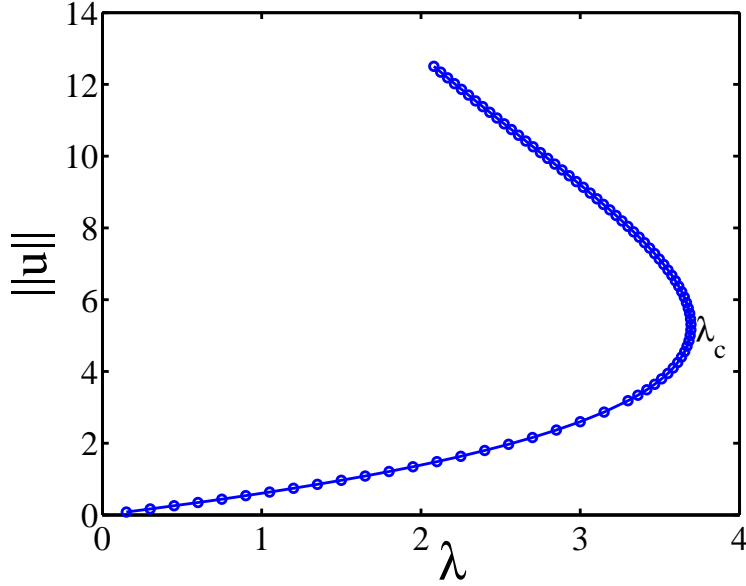
Figure 6.1: Bifurcation diagram for Bratu-Gelfand equation w.r.t. the parameter λ: $||u||$ versus λ.

The bifurcation diagram computed by RPM algorithm is shown in Fig.6.1. This diagram compares very well to the one presented by Shroff and Keller (Fig. 1, [97]).

As already discussed in the Chapter 2, the ultimate convergence rate of the fixed point iteration $u^{n+1} = F(u^n)$ in (2.21) depends on the spectral radius $\rho(J)$, identified as the eigenvalue with largest modulus of the Jacobian matrix $J(u_s) \equiv \dfrac{\partial F(u_s)}{\partial u}$, where u_s is the fixed point $u_s = F(u_s)$. The spectral radius $\rho(J)$ is closely related to the parameter λ, see figure 6.2. Since the RPM technique deals only with the largest eigenvalues of J lying outside K_δ, we detect $\rho(J) > 0.5$ only at $\lambda_* = 3.29$.

We can clearly see from figures 6.1 and 6.2 that for each λ-value, there are two different solutions, one stable and the other unstable. The fixed point iteration can only compute the solutions on the lower (stable) part of the branch. Furthermore the convergence rate approaches zero as λ approaches $\lambda_c = 3.68$, the turning point where $\rho(J)$ becomes unity. Beyond the turning point, the upper branch solution becomes unstable, which corresponds to the spectral radius $\rho(J) > 1$.

Figure 6.3 shows the dependence of the solution on λ. As λ approaches back zero along the unstable branch, the solution becomes less and less smooth, which slows down the convergence of the method.
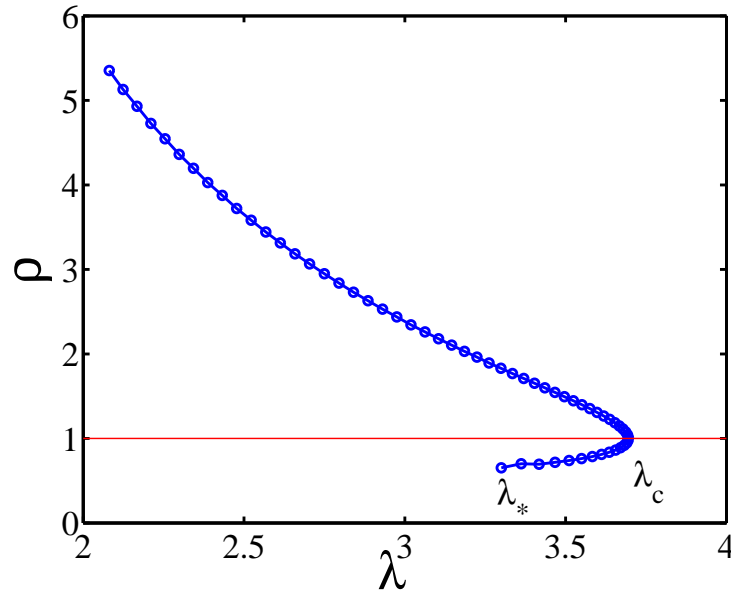
Figure 6.2: The spectral radius ρ as a function of the parameter λ.

6.2 Matlab script

This section is dedicated to a brief explanation of the matlab script written for this numerical investigation.

6.2.1 Time step subroutine

As mentioned earlier, the RPM technique uses the timestepper as a "black box". However, the timestepping routine can be used itself for the straightforward fixed point iteration scheme (Picard scheme) in presence of a stable steady state. Until RPM detects the first eigenvalue leaving K_δ for $\lambda < \lambda_*$ the solutions are obtained by means of Picard iterations only.

The following subroutine represents the spatial discretization of the operator $f(u, \lambda)$:

```
1: function [f]=myf_small(t,U)
2: global lambda
3: global N
4: global delta_x
5: F=zeros(N,1);
6: F(2:N-1)=(U(3:N)-2*U(2:N-1)+U(1:N-2))/(delta_x^2)+lambda*exp(U(2:N-1));
```

Lines 2 to 4 describe the variables used in this computation, where N is the number of grid points, delta_x$= 1/N$ and parameter λ. During the course of the integration N and delta_x stay constant, as defined in the main routine, however, λ changes as we proceed

119
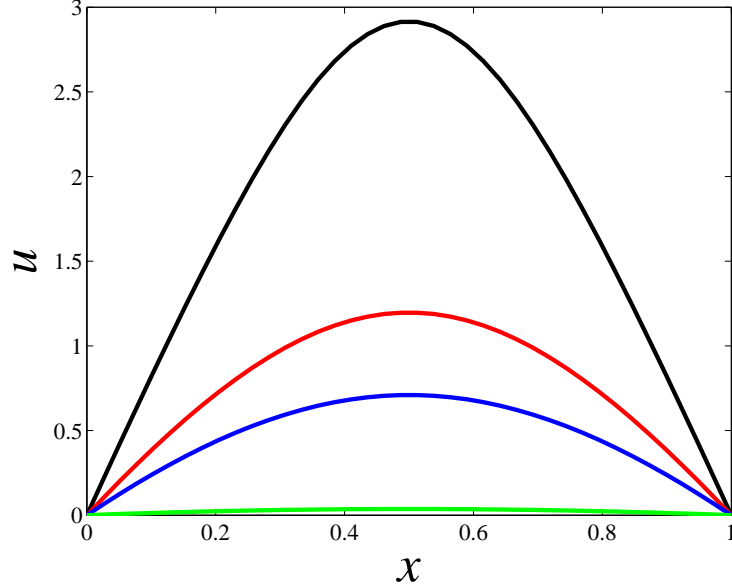
Figure 6.3: Solution curve for various parameters λ: green line $\lambda = 0.3$, stable solution;
blue line $\lambda = \lambda_* = 3.29$; red line $\lambda = \lambda_c = 3.68$ marginally unstable solution; black line
$\lambda = 2.081$ unstable solution.

with the continuation of the solution. Since the value of u is imposed at both boundaries
we directly set this value to zero over the whole time of integration, see line 5. Line 6
represents the discretization of the right hand side part of the equation (6.1).

This is the timestepping routine, which integrates the discretized operator in time over
$[0 : \delta t]$ (with $\delta t = 0.1$, see line 3:

1: function [F]=myF(U_in, delta_t)
2: options = odeset('RelTol',1e-5,'AbsTol',1e-5);
3: [t,u]=ode23(@myf_small,[0,delta_t],U_in,options);
4: F=[u(size(t,1),:)];

Here U_in is the input value for u; in line 3 "ode23" is second-third order Runge-Kutta
matlab integrator. We need to know only the solution after the integration has been com-
pleted, thus we save only the velocity field $u(\delta t)$ at the final time, which corresponds to
the result of the integration over the delta_t, see line 4.

6.2.2   Jacobian matrix-vector product and F_λ subroutines

Since the RPM does not require the explicitly formed Jacobian matrix, we only need to
know the effect of the Jacobian on the basis vectors Z_i, so we approximate the matrix-vector
product JZ using finite differences:

1: function [J]=myJ(U,Z)
2: global N;

3: delta_t=0.1;
4: J(1:size(Z,1),N-2)=0;
5: U2(1:N)=0;
6: [F1]=myF(U, delta_t);
7: my_eps=10^(-3);
8: for i=1:size(Z,1)
9: U2=U+my_eps*Z(i,1:N);
10: [F2]=myF(U2, delta_t);
11: J(i,1:N-2) = (F2(2:N-1)-F1(2:N-1))/my_eps;
12: end

Here we perturb the velocity field in the direction of the basis vectors, line 9, with $\epsilon = 10^{-3}$ and compute the approximation of the Jacobian matrix-vector product in line 11. Since u is imposed at the boundaries, we calculate JZ only inside the computational domain excluding boundaries.

In the case of the 1-dimensional Bratu equation (6.1) the function F_λ can be found explicitly, however, in the general case this is rarely possible. In such a case we use a similar finite difference approximation using $\epsilon = 10^{-3}$ (line 7):

1: function [dF_dl]=dF_dlambda(U)
2: global lambda;
3: global N;
4: delta_t=0.1;
5: dF_dl(1:N-2)=0;
6: [F1]=myF(U, delta_t);
7: lambda=lambda+ 1.D-3;
8: [F2]=myF(U, delta_t);
9: dF_dl(1:N-2)=(F2(2:N-1)-F1(2:N-1))/1.D-3;
10: lambda=lambda_old;

Here as in the previous subroutine, the size of F_λ is $N - 2$ since $u(0) = u(1) = 0$.

6.2.3 Basis increase subroutine

This subroutine increases the size nZ of the projection basis Z:

1: function[Z,nZ]=increasing_basis(Z,nZ,dq)
2: global N;
3: clear a;
4: [Q,R] = qr(dq',0);
5: a(1:(size(R,2)))=abs(diag(R,0));
6: cnt=0;
7: for i=1:(size(R,2)-1);
8: if (a(i)/a(i+1)>1000);
9: cnt=i;
10: end

11: end
12: nZ=size(Z,1);
13: if cnt>0
14: Z((nZ+1):(nZ+cnt),1:N)=(Q(1:N,1:cnt))';
15: end
16: [Q1,R1] = qr(Z',0);
17: Z=Q1';
18: nZ=size(Z,1);

We ortogonalize Δq using the matlab function "qr", writing the orthogonal vectors in a matrix Q, line 4. The upper-diagonal matrix R contains the coefficient of this decomposition. Using the Krylov acceptance ratio $k_a = 1000$ we calculate *cnt*, the number of columns of Q to be added the basis Z, lines 5-11, then we add the columns of Q to Z, line 13-15, and re-orthogonalize the new basis Z, lines 16-17. The output of this subroutine is the updated orthogonal basis Z with the size nZ.

6.2.4   Basis decrease subroutine

In this subroutine we check which eigenvalue of the small matrix H lies outside the disk K_δ:

 1: function [Z,nZ]=decrease_basis(Z,nZ,H)
 2: format long e;
 3: [v,e] = eig(H);
 4: a=diag(e,0);
 5: cnt=0;
 6: for i=1:(size(H,2));
 7: if (abs(a(i))>0.5);
 8: cnt=cnt+1;
 9: v2(:,cnt)=v(:,i);
10: end
11: end
12: if cnt>0
13: Zv=Z'*v2;
14: [Q1,R1] = qr(Zv,0);
15: clear Z
16: Z=Q1';
17: end
18: nZ=size(Z,1)

As input we give the matrix H, the eigenvalues and eigenvectors computed using the matlab function "eig" in line 3. We are interested only in the eigenvalues lying outside K_δ, i.e. with a modulus larger than $\delta = 0.5$, lines 7-11, then we estimate the new basis Z associated with the eigenvalues outside K_δ, lines 12-17. As output of the routine we obtain the new basis Z and its size nZ.

6.2.5 RPM subroutine

This subroutine presents the pseudo-arclengh continuation routine based on the algorithm presented page 51 of this dissertation:

```
 1: function [U,lambda,nZ,Z]=my_rpm_simple(U0,lambda0, U, lambda, ds, n_max, tol,
    delta_t, nZ, Z,theta)
 2: global lambda
 3: global delta_x
 4: global N
 5: [F]=myF(U, delta_t);
 6: [dF_dl]=dF_dlambda(U);
 7: iter=0;
 8: resid=norm(F-U,2);
 9: q=0;
10: if (nZ>0)
11: [J]=myJ(U,Z);
12: H=Z(1:nZ,2:N-1)*J';
13: [Z,nZ]=decrease_basis(Z,nZ,H);
14: clear zi0 zi1 J H zidot xi2;
15: if (nZ>0)
16: zi0=Z*U0';
17: zi1=Z*U';
18: [J]=myJ(U,Z);
19: H=Z(1:nZ,2:N-1)*J';
20: H=eye(size(H))-H;
21: zidot=2*theta*(zi1-zi0)/(lambda-lambda0);
22: zidot=2*theta*(zi1-zi0)/(lambda-lambda0);
23: xi2=Z(1:nZ,2:N-1)*dF_dl';
24: M(1:nZ,1:nZ)=H;
25: M(1:nZ,nZ+1)=-xi2;
26: M(nZ+1,1:nZ)=zidot';
27: M(nZ+1,nZ+1)=2*(1-theta)*(lambda-lambda0)/ds;
28: M=inv(M);
29: end
30: end
31: while (resid>tol)
32: if (iter/4*4==iter)
33: old_q =q;
34: end
35: if (nZ==0)
36: q=F;
37: U=F;
38: [F]=myF(U, delta_t);
39: resid=norm(F-U,2);
```

```
40: else
41: zi1=Z*U';
42: xi=Z*F';
43: xi2=Z(1:nZ,2:N-1)*dF_dl';
44: q=F-(Z'*xi)';
45: q(1,1)=0;
46: q(1,N)=0;
47: zi2=zi1-zi0;
48: clear zz2;
49: zz2(1:nZ,1)=zi1-xi;
50: resid_N=theta*dot(zi2,zi2)/ds+(1-theta)*(lambda-lambda0)'2/ds -ds;
51: zz2(nZ+1,1)=resid_N;
52: zz3(1:nZ,1)=zi1;
53: zz3(nZ+1,1)=lambda;
54: zz3(1:nZ+1,1)=zz3(1:nZ+1,1)-M*zz2;
55: temp(1,1:N)=(Z'*xi2)';
56: q(2:N-1)=q(2:N-1)-(zz3(nZ+1,1)-lambda)*(dF_dl(1:N-2)-temp(2:N-1));
57: lambda=zz3(nZ+1,1);
58: p=(Z'*zz3(1:nZ,1))';
59: p(1,1)=0;
60: p(1,N)=0;
61: U=p+q;
62: U(1,1)=0; U(1,N)=0;
63: [F]=myF(U, delta_t);
64: resid=norm(F-U,2)
65: [dF_dl]=dF_dlambda(U);
66: iter=iter+1;
67: if (iter>(n_max-9))
68: dq(n_max-iter+1,1:N)=q-old_q;
69: end
70: if (iter==n_max)
71: iter=0;
72: [Z, nZ]=increasing_basis(Z,nZ,dq);
73: [J]=myJ(U,Z);
74: H=Z(1:nZ,2:N-1)*J';
75: [Z,nZ]=decrease_basis(Z,nZ,H);
76: if (nZ>0)
77: clear zi0 zi1 J H zidot xi2;
78: zi0=Z*U0';
79: zi1=Z*U';
80: [J]=myJ(U,Z);
81: H=Z(1:nZ,2:N-1)*J';
82: H=eye(size(H))-H;
83: zidot=2*theta*(zi1-zi0)/(lambda-lambda0);
```

84: xi2=Z(1:nZ,2:N-1)*dF_dl';
85: M(1:nZ,1:nZ)=H;
86: M(1:nZ,nZ+1)=-xi2;
87: M(nZ+1,1:nZ)=zidot';
88: M(nZ+1,1:nZ)=zidot';
89: M(nZ+1,nZ+1)=2*(1-theta)*(lambda-lambda0)/ds;
90: M=inv(M);
91: end
92: end
93: end

As input of the subroutine (line 1) we use the following set of parameters: the converged solution U_0 corresponding to $\lambda = \lambda_0$; the predicted values for U and λ; the continuation parameter ds; the tolerance criterion for convergence tol; the maximum number of iterations n_max after which we increase the size of the projection basis Z, and the weight parameter θ used for continuation:

$$N = \theta \dot{p}^T \Delta p + (1 - \theta) \dot{\lambda} \Delta p - \Delta s.$$

This subroutine is already presented and explained in detail in section 2.3.3, Chapter 2. Thus here we give only brief explanations of the algorithm. We form the matrix M (2.26) and update the basis of projection Z in lines 11-28 and 76-90. Lines 31-90 represent the main part of the subroutine updating the solution U and λ, using the convergence criterion $resid < tol$. If the size of basis is $nZ = 0$ we use only power iterations, lines 35-39, otherwise we use the projection onto the unstable subspace where we perform Newton iterations, lines 41-43, 47-54 and 57-58. In the stable subspace q we use power iterations (line 44), then perform the correction requested by the change in λ line 56.

In line 61 and 62, correspondingly, we reconstruct the solution from p and q and enforce the boundaries conditions $u(0) = u(1) = 0$. We then recompute the residual, line 64.

We build the Δq matrix (line 67-69) in order to update the basis Z and speed up the convergence of the code (using the last 5 computed vectors q only proved sufficient). In this case, if the procedure does not converge in less than n_{max} iterations we update the basis and recompute the matrix M, lines 70-92. As output we obtain the new converged solution U and the parameter λ with a projection basis Z of size nZ.

6.2.6   Main routine

Finally we present the governing routine:

1: clear all
2: format long e;
3: global lambda
4: L=1;

```
 5: N=40;
 6: delta_x=L/N;
 7: delta_t=0.1;
 8: ds=0.15;
 9: tol=10^(-4);
10: n_max=13;
11: U0=[0 0 0 0 0 0 0 0 0 0 0 0 0 0 0 0 0 0 0 0 0 0 0 0 0 0 0 0 0 1 0 0 0 0 0 0 0 0 0 0 0]';
12: lambda0=0;
13: lambda=lambda0+ds;
14: U=U0;
15: nZ=0;
16: Z=0;
17: theta=0.1;
18: for i=1:100
19: [U,lambda,nZ,Z]=my_rpm_simple(U0,lambda0, U, lambda, ds, n_max, tol, delta_t, nZ,
    Z,theta)
20: u_out(i)=norm(U,2);
21: lambda_out(i)=lambda;
22: lambda_new=2*lambda-lambda0;
23: U_new=2*U-U0;
24: lambda0=lambda;
25: U0=U;
26: lambda=lambda_new;
27: U=U_new;
28: end
```

First of all, we define the main parameters such as the length of the domain L, the
number of grid points N, the length between grid points Δx, size of a time step Δt, the
arc-length continuation parameter ds, the convergence criterion tol and the maximum num-
ber of iterations n_max, lines 4-10. We also define some initial condition for the solution u
in line 11 and an initial value for λ in line 12. We also impose the basis of the projection
on the first iteration to be zero (lines 15-16), meaning that the solution is stable, and the
weight parameter $\theta = 0.1$ defined in line 17. At the fist iteration we approximate the sought
solution by the initial solution and the sought value of λ by $\lambda = \lambda_0 + ds$, lines 11 and 13,
respectively.

Calling the pseudo-arclength continuation subroutine in line 19 we perform the contin-
uation w.r.t. the parameter λ. Every time we need an approximation of a new predicted
solution and a new predicted parameter lambda in (2.31) we use lines 22-27. We output
only the L_2-norm of the computed solution with the corresponding parameter λ, lines 20-21.

Bibliography

[1] E.A. Akervik, L. Brandt, D.S. Henningson, J.P.J. Hoepffner, O. Marxen, and P. Schlatter. Steady solutions of the navier-stokes equations by selective frequency damping. *Phys. Fluids*, 18:068102, 2006.

[2] W. Althaus, C. Brüker, and M. Weimer. *Fluid Vortices*, chapter Breakdown of slender vortices, pages 373–426. Kluwer, 1995.

[3] W. Althaus and E. Krause. Flow visualisation of flows with concentrated vorticity. Technical report, EC Contract SC1-0212, 1990.

[4] R.L. Ash and M.R. Khorrami. *Fluid Vortices*, chapter Vortex stability, page 317. Kluwer, 1995.

[5] G.K. Batchelor. *An Introduction to Fluid Dynamics*. Cambridge University Press, 1967.

[6] J. Beer and N. Chigier. *Combustion Aerodynamics*. Applied Science Publishers, 1972.

[7] T.B. Benjamin. Theory of the vortex breakdown phenomenon. *J. Fluid Mech.*, 14:593, 1962.

[8] T.B. Benjamin. Significance of the vortex breakdown phenomenon. *Trans ASME, J Basic Engng*, 87:518–24, 1965.

[9] T.B. Benjamin. Some developments in the theory of vortex breakdown. *J. Fluid Mech.*, 21 (1):65–84, 1967.

[10] P.S. Beran. *An investigation of the bursting of trailing vortices using numerical simulation*. PhD thesis, California Institute of Technology, 1989.

[11] P.S. Beran. The time-asymptotic behavior of vortex breakdown in tubes. *Comput. Fluids*, 23:913, 1994.

[12] P.S. Beran and F.E.S. Culick. The role of non-uniqueness in the development of vortex breakdown in tubes. *J. Fluid Mech.*, 242:491–527, 1992.

[13] P. Billant, J.-M. Chomaz, and P. Huerre. An experimental study of vortex breakdown in swirling jets. *J. Fluid Mech.*, 376:183–219, 1998.

[14] B. Boersma, G. Brethouwer, and F. Nieuwstadt. A numerical investigation on the effect of the inflow conditions on the self-similar region of a round jet. *Phys. Fluids*, 10:899, 1998.

[15] E.A. Brandes. Mesocyclone evolution and tornadogenesis: Some observations. *Mon. Wea. Rev.*, 106:995–1011, 1978.

[16] C. Brüecker and W. Althaus. Study of vortex breakdown by particle tracking velocimetry(ptv). part 3: Time dependent structure and development of breakdown modes. *Exp. Fluids*, 18:174, 1995.

[17] J.D. Buntine and P.G. Saffman. Inviscid swirling flows and vortex breakdown. *Proc. R. Soc. London*, 449:139, 1995.

[18] A. J. Chorin. A numerical method for solving incompressible viscous flow problems. *J. Comput. Phys.*, 2:12–26, 1976.

[19] G.S. Constantinescu and S.K. Lele. A highly accurate technique for treatment of flow equations at polar axis in cylindrical coordinates using series expansions. *J. Comput. Phys.*, 183:165–186, 2002.

[20] A.W. Cook and J.J. Riley. Direct numerical simulations of a turbulent reactive plume on a parallel computer. *J. Comput. Phys.*, 129(2):263–283, 1996.

[21] J.W. Cooley, P.A. Lewis, and P.D. Welch. The fast fourier transform algorithm: Programming considerations in the calculations of sine, cosine and laplace transforms. *J. Sound Vib.*, 12:315–337, 1970.

[22] D.L. Darmofal. Comparison of experimental and numerical results for axisymetric vortex breakdown in pipes. *Comput. Fluids*, 25:353, 1996.

[23] R. P. Davies-Jones. *Thunderstorms: A Social, Scientific and Technological Documentary*, chapter Tornado dynamics, page Vol.2 297. Univercity of Oklahoma, Nolan, 1983.

[24] J. M. Delery. Aspects of vortex breakdown. *Prog. Aerosp. Sci.*, 30:1, 1993.

[25] O. Derzho and R. Grimshaw. Solitary waves with recirculation zones in axisymmetric rotating flows. *J. Fluid Mech.*, 462:217–250, 2002.

[26] M.P. Escudier. Vortex breakdown: observations and explanations. *Prog. Aerosp. Sci.*, 25:189–229, 1988.

[27] M.P. Escudier and J.J. Keller. Vortex breakdown: a two-stage transition. *AGARD CP: aerodynamics of vortical type flows in 3D*, 342:25, 1983.

[28] M.P. Escudier and N. Zehnder. Vortex-flow regimes. *J. Fluid Mech.*, 115:105–121, 1982.

[29] J.H. Faler and S. Leibovich. Disrupted states of vortex flow and vortex breakdown. *Phys. Fluids*, 20:1385, 1977.

[30] J.H. Faler and S. Leibovich. An experimental map of the internal structure of vortex breakdown. *J. Fluid Mech.*, 86:313–335, 1978.

[31] S. Farokhi, R. Taghavi, and E.J. Rice. Effect of initial swirl distribution on the evolution of a turbulent jet. *AIAA J.*, 27:700–706, 1988.

[32] F. Gallaire and J.-M. Chomaz. Mode selection in swirling jet experiments: a linear stability analysis. *J. Fluid Mech.*, 494:223–253, 2003.

[33] F. Gallaire, M.R. Ruith, E. Meiburg, J.-M. Chomaz, and P. Huerre. Spiral vortex breakdown as a global mode. *J. Fluid Mech.*, 549:71–80, 2006.

[34] T.B. Gatski and R.E. Spall. Numerical studies of vortex breakdown : from helices to bubbles. *Fourth. Int. Symposium on Comp. Fluid Dynamics*, 1:418–423, 1991.

[35] S. Görtz and J. Möller. Evaluation of the recursive projection method for efficient unsteady turbulent cfd simulations. In *Proc. ICASE*, 2004.

[36] S. Görtz and J. Möller. Recursive projection method for efficient unsteady cfd simulations. In *Proc. ECCOMAS*, 2004.

[37] W. Grabowski and S. Berger. Solutions of the navier-stokes equations for vortex breakdown. *J. Fluid Mech.*, 75:525, 1976.

[38] A. K. Gupta, D.J. Lilley, and N. Syred. *Swirl Flows*. Abacus, Kent, England, 1984.

[39] L.N. Gutman. Theoretical models of waterspout. *Bull. Acad. Sci. USSR Geophys. Ser.*, 1:87, 1957.

[40] M. Hafez, G. Kuruvila, and M. D. Salas. Numerical study of vortex breakdown simulation. In *AIAA-paper 86-0558*, 1986.

[41] M.G. Hall. Vortex breakdown. *Annu Rev. Fluid Mech.*, 4:195–217, 1972.

[42] M.G. Hall. An introduchtion to vortex breakdown and vortex core bursting. In *No.24336*, 1985.

[43] A. Hanifi, P.J. Schmid, and D.S. Henningson. Transient growth in compressible boundary layer flow. *Phys. Fluids*, 8:826–837, 1996.

[44] J.K. Harvey. Some observations of vortex breakdown phenomenon. *J. Fluid Mech.*, 14:585–592, 1962.

[45] M.A. Herrada and R. Fernandez-Feria. On the development of three-dimensional vortex breakdown in cylindrical regions. *Phys. Fluids*, 18:084105, 2006.

[46] M.K. Herrada and V. Shtern. Control of vortex breakdown by temperature gradient. *Phys.Fluids.*, 15:3468, 2003.

[47] D. Hummel and P.S. Srinivasan. Vortex breakdown effects on the low-speed aerodynamic characteristics of slender delta wings in symmetrical flow. *J. R. Aeronaut. Soc.*, 71:319, 1967.

[48] T. Husveg, O. Rambeau, T. Drengstig, and T. Bilstad. Performance of a deoiling hydrocycone during variable flow rates. *Minerals Engineering*, 20:368–379, 2007.

[49] J. Jacobsen and K. Schmitt. The liouville-bratu-gelfand problem for radial operators. *J. Different Equat.*, 184:283–298, 2002.

[50] V. Janovsky and O. Liberda. Continuation of invariant subspaces via the recursive projection method. *Applications of Mathematics*, 48(4):241–255, 2003.

[51] H.B. Keller. *Numerical solution of bifurcation and nonlinear eigenvalue problems, in application in bifurcation theory*, pages 359–384. Academic Press, New York, 1987.

[52] J.J. Keller, W. Egli, and J. Exley. Force- and loss-free transitions between two states. *J. Appl. Math. Phys.*, 36 (6):854–889, 1985.

[53] N.C. Lambourne. The breakdown of certain types of vortex. In *Aeronautical Research Council -Current paper 915*, 1967.

[54] N.C. Lambourne and D.W. Bryer. The bursting of leading-edge vortices: some observations and discussion of the phenomenon. In *Aeronautical Research Council R & M, 3282*, 1967.

[55] B. Leclaire and D. Sipp. A sensitivity study of vortex breakdown onset to upstream boundary conditions. *J.Fluid Mech.*, 645:81–119, 2010.

[56] R.B. Lehoucq, D.C. Sorensen, and C. Yang. *ARPACK Usrs' Guide: Solution of Large-scale Eigenvalue Problems with Implicitly Restarted Arnoldi Methods.* SIAM, 1998.

[57] S. Leibovich. Weakly nonlinear waves in rotating fluids. *J. Fluid Mech.*, 42:803, 1970.

[58] S. Leibovich. The structure of vortex breakdown. *Ann. Rev. Fluid Mech.*, 10:221–246, 1978.

[59] S. Leibovich. Vortex stability and breakdown: survey and extension. *AIAA J*, 22(9):1192–1206, 1983.

[60] S. Leibovich. Vortex stability and breakdown: survey and extension. *AIAA J.*, 22:1192–1206, 1984.

[61] S. Leibovich and K. Stewartson. A sufficient condition for the instability of columnar vortices. *J. Fluid Mech.*, 126:335–356, 1983.

[62] S.K. Lele. Compact finite difference schemes with spectral-like resolution. *J. Comput. Phys.*, 103:16–42, 1992.

[63] H. Liang and T. Maxworthy. An experimental investigation of swirling jets. *J. Fluid Mech.*, 525:115–159, 2005.

[64] J.M. Lopez. On the bifurcation structure of axisymmetric vortex breakdown in a constricted pipe. *Phys. Fluids*, 6:3683, 1994.

[65] M.V. Lowson. Some experiments with vortex breakdown. *J.R. Aeronaut.Soc.*, 68:343, 1964.

[66] O. Lucca-Negro and T. O'Doherty. Vortex breakdown: a review. *Prog. Energy Combust. Sci*, 431-481:2001, 27.

[67] H.J. Lugt. Vortex breakdown in atmospheric columnar vortices. *Bull. Amer. Meteor. Soc.*, 70:1526–1537, 1989.

[68] A. Mager. Dissipation and breakdown of a wing-tip vortex. *J. Fluid Mech.*, 1972:609, 55.

[69] P. Meliga, J.-M. Chomaz, and D. Sipp. Unsteadiness in the wake of disks and spheres: instability, receptivity and control using direct and adjoint global stability analyses. *J. Fluids Struct.*, 25:601–616, 2009.

[70] J. Möller. The recursive projection method applied to steady-state cfd calculations. Technical report, Royal Institute of Technology (KTH), Dept. of Numerical Analysis and Computer Science, TRITA-NA-0445, 2004.

[71] J.W. Nichols. *Simulations and stability analysis of jet diffusion flame.* PhD thesis, U Washington, 2005.

[72] J.W. Nichols, P.J. Schmid, and J.J. Riley. Self-sustained oscillations in variable-density round jets. *J. Fluid Mech.*, 582:341, 2007.

[73] F. Novak and T. Sarpkaya. Turbulent vortex breakdown at high reynolds numbers. In *AIAA paper No.1999-0135*, 1999.

[74] J. Panda and D.K. McLaughlin. Experiments on the instabilites of a swirling jet. *Phys. Fluids*, 6:263–276, 1994.

[75] R.L. Pauley and J.T. Snow. On the kinematics and dynamics of the 18 july 1986 minneapolis tornado. *Mon. Wea. Rev.*, 116:2731–2736, 1988.

[76] D.H. Peckham and S.A. Atkison. Preliminary results of low speed wind tunnel tests on a gothic wing of aspect ratio 1.0. *Aero. Res. Counc.*, CP-508:16–17, 1957.

[77] C.M. Reber. The south platte valley tornadoes of june 7, 1953. *Bull.Amer.Met. Soc.*, 35:191–197, 1954.

[78] M.R. Ruith, P. Chen, and E. Meiburg. Development of boundary conditions for direct numerical simulations of three-dimensional vortex breakdown in semi-infinite domains. *Comput. Fluids*, 33:1225–1250, 2004.

[79] M.R. Ruith, P. Chen, E. Meiburg, and T. Maxworthy. Three-dimensional vortex breakdown in swirling jets and wakes: direct numerical simulations. *J. Fluid Mech.*, 486:331–378, 2003.

[80] M.R. Ruith and E. Meiburg. Direct numerical simulations of spatially developing, three-dimensional swirling jets. *J. of Turbulence*, 3:065, 2002.

[81] Z. Rusak. The interaction of near-critical swirling flows in a pipe with inlet azimuthal vorticity perturbations. *Phys. Fluids*, 10 (7):1672–1684, 1998.

[82] Z. Rusak. Review of recent studies on the axisymmetric vortex breakdown phenomenon. *AIAA Paper*, 2000:2529, 2000.

[83] Z. Rusak and K.P. Judd. The stability of noncolumnar swirling flows in diverging streamtubes. *Phys. Fluids*, 13 (10):2835–2844, 2001.

[84] Z. Rusak, K.P. Judd, and S. Wang. The effect of small pipe divergence on near critical swirling flows. *Phys. Fluids*, 9 (8):2273–2285, 1997.

[85] Z. Rusak, A. K. Kapila, and J.J. Choi. Effect of combustion on near-critical swirling flow. *Combustion Theory and Modelling*, 6 (4):625–645, 2002.

[86] Z. Rusak and C.C. Meder. Near-critical swirling flow in a slightly contracting pipe. *AIAA J.*, 42 (11):2284, 2004.

[87] Z. Rusak and S. Wang. Review of theoretical approaches to the vortex breakdown phenomenon. *AIAA Pap.*, 96:2126, 1996.

[88] Z. Rusak, S. Wang, and C.H. Whiting. The evolution of a perturbed vortex in a pipe to axisymetric vortex breakdown. *J. Fluid Mech.*, 366:211, 1998.

[89] Z. Rusak and Whiting-C. H. Wang, S. Numerical computations of axisymmetric vortex breakdown in a pipe. *AIAA Pap*, 96:0801, 1996.

[90] Z. Rusak, C.H. Whiting, and S. Wang. Axisymmetric breakdown of a q-vortex in a pipe. *AIAA J.*, 36:659, 1998.

[91] T. Sarpkaya. On stationary and travelling vortex breakdown. *J. Fluid Mech.*, 45:545–559, 1971.

[92] T. Sarpkaya. Vortex breakdown in swirling conical flows. *AIAA J.*, 9:1792–1799, 1971.

[93] T. Sarpkaya. Effect of the adverse pressure gradient on vortex breakdown. *AIAA J.*, 12:602–607, 1974.

[94] T. Sarpkaya. Turbulent vortex breakdown. *Phys. Fluids*, 7:2301, 1995.

[95] T. Sarpkaya. Vortex breakdown and turbulence. In *AIAA Paper No. 95-0433*, volume 95, page 0433, 1995.

[96] P.J. Schmid and D.S. Henningson. *Stability and Transition in Shear Flows*. Springer-Verlag, New York,NY, 2001.

[97] G.M. Shroff and H.B. Keller. Stabilisation of unstable procedures: the recursive projection method. *SIAM J. Num. Anal.*, 30:1099–1120, 1993.

[98] S. Sivasegaram and J.H. Whitelaw. The influence of swirl on oscillations in ducted premixed flames. *Comb. Flame*, 85:195–205, 1991.

[99] D.O. Snyder and R.E. Spall. Numerical simulation of bubble-type vortex breakdown within a tube-and-vane apparatus. *Phys. Fluids*, 12:603, 2000.

[100] R. Spall and D. Snyder. Numerical simulations of vortex breakdown: review and recent developments. *Recent REs Devel Heat, Mass Moment Transfer*, 2:41–70, 1999.

[101] H.B. Squire. *Analysis of the vortex breakdown phenomenon*, chapter Miszallaneen der angewandten Mechanik, pages 306–312. Akademie, Berlin, 1960.

[102] H.B. Squire. Analysis of the vortex breakdown phenomenon, part 1. Technical report, No. 102, Imperial College of Science and Technology Aeronautics, 1960.

[103] J.T. Stuart. A critical review of vortex breakdown theory. In *Vortex control and breakdown behaviour, Second International Colloquium on Vortical Flows, BBC*, 1987.

[104] S. Táasan. Multigrid method for a vortex breakdown simulation. Technical report, NASA Contractor Rep. 178106, 1986.

[105] L. N. Trefethen. *Spectral Methods in Matlab*. SIAM, Philadelphia, PA, 2000.

[106] S. Uchida, Y. Nakamura, and M. Oshawa. Experiments on the axisymmetric vortex breakdown in a swirling air flow. *Trans. Jpn. Soc. Aero. Sci.*, 27:206–216, 1985.

[107] E. Vyazmina, J.W. Nichols, J.-M. Chomaz, and P. J. Schmid. Bifurcation structure of viscous vortex breakdown. In *Proc. of the 5th AIAA Theoretical Fluid Mechanics Conference, Seattle, AIAA-2008-3797*, 2008.

[108] E. Vyazmina, J.W. Nichols, J.-M. Chomaz, and P. J. Schmid. The bifurcation structure of viscous steady axisymmetric vortex breakdown with open lateral boundaries. *Phys. Fluids*, 21:074107, 2009.

[109] R.M. Wakimoto and C. Liu. The garden city, kansas, storm during vortex 95. part ii: The wall cloud and tornado. *Mon. Wea. Rev.*, 126:393–408, 1998.

[110] R.L. Walko. *Tornado spin-up beneath a convective cell: Requires basic stucture of the near-field boundary layer wind*, chapter The Tornado: its stucture, dynamics, prdiction, and hazards., pages 89–95. American Geophysical Union, 1993.

[111] S. Wang and Z. Rusak. On the stability of an axisymmetric rotating flow. *Phys. Fluids*, 8:1007, 1996.

[112] S. Wang and Z. Rusak. On the stability of non-columnar swirling flow. *Phys. Fluids*, 8:1017, 1996.

[113] S. Wang and Z. Rusak. The dynamics of a swirling flow in a pipe and transition to axisymmetric vortex breakdown. *J. Fluid Mech.*, 340:177–223, 1997.

[114] S. Wang and Z. Rusak. The effect of slight viscosity on a near-critical swirling flow in a pipe. *Phys. Fluids*, 9 (7):1914–1927, 1997.

[115] E. Wedermeyer. Vortex breakdown. In *High angle of attack aerodynamics*. AGARD-VKI Lecture Series 121:, 1982.